Dissertation zur Erlangung des Doktorgrades der Fakultät für Mathematik und Physik der Albert-Ludwigs-Universität Freiburg im Breisgau

Search for supersymmetric particles in final states with jets and missing transverse momentum with the ATLAS detector

von Michael Rammensee

Eingereicht am 17.04.2013

Betreut von Prof. Dr. Gregor Herten

Dekan:	Prof. Dr. Michael Ruzicka
Prodekan:	Prof. Dr. Andreas Buchleitner
Referent:	Prof. Dr. Gregor Herten
Koreferent:	Prof. Dr. Karl Jakobs
Prüfer (Experiment):	Prof. Dr. Markus Schuhmacher
Prüfer (Theorie):	JProf. Dr. Harald Ita
Datum der mündlichen Prfung:	11.06.2013

Erklärung

Hiermit erkläre ich die vorliegende Arbeit selbständig und nur mit den angegebenen Quellen und Hilfsmitteln verfasst zu haben. Einige Ergebnisse dieser Arbeit wurden in den untenstehenden Publikationen bereits veröffentlicht.

Freiburg, den 17.04.2013

Michael Rammensee

Publications with own contributions

[1] ATLAS Collaboration, *Search for squarks and gluinos using final states with jets and missing transverse momentum with the ATLAS detector in* $\sqrt{s} = 7$ *TeV proton–proton collisions*, Phys. Lett. **B701** (2011) 186, arXiv:1102.5290 [hep-ex].

[2] ATLAS Collaboration, *Search for squarks and gluinos using final states with jets and missing transverse momentum with the ATLAS detector in* $\sqrt{s} = 7$ *TeV proton-proton collisions*, ATLAS-CONF-2011-086 , https://cdsweb.cern.ch/record/1356194.

[3] M. Rammensee, *Search for Supersymmetry in final states with jets and missing transverse momentum with the ATLAS detector*, Tech. Rep. ATL-PHYS-PROC-2013-045, CERN, Geneva, Feb, 2013.

[4] ATLAS Collaboration, *Search for squarks and gluinos using final states with jets and missing transverse momentum with the ATLAS detector in* $\sqrt{s} = 7$ *TeV proton-proton collisions*, Phys. Lett. **B710** (2011) 67–85, arXiv:1109.6572 [hep-ex].

[5] ATLAS Collaboration, *Search for squarks and gluinos using final states with jets and missing transverse momentum with the ATLAS detector in* $\sqrt{s} = 7$ *TeV proton-proton collisions*, Phys. Rev. **D87** (2013) 012008, arXiv:1208.0949 [hep-ex].

[6] ATLAS Collaboration, *Search for squarks and gluinos with the ATLAS detector using final states with jets and missing transverse momentum and 5.8* fb^{-1} *of* $\sqrt{s} = 8$ *TeV proton-proton collision data*, Tech. Rep. ATLAS-CONF-2012-109, CERN, Geneva, Aug, 2012.

[7] M.Rammensee, *Search for squarks and gluinos using final states with jets and missing transverse momentum with the ATLAS detector*, 6th Annual Workshop of the Helmholtz Alliance: Physics at the Terascale, Hamburg, 2012.

[8] ATLAS Collaboration, *Prospects for Supersymmetry and Univeral Extra Dimensions discovery based on inclusive searches at a 10 TeV centre-of-mass energy with the ATLAS detector*, Tech. Rep. ATL-PHYS-PUB-2009-084, CERN, Geneva, Jul, 2009.

[9] *Internal :* ATLAS Collaboration, *Setting exclusion limits in ATLAS supersymmetry searches with a likelihood ratio based method*, Tech. Rep. ATL-COM-PHYS-2011-004, CERN, Geneva, 2011.

[10] M.Rammensee, *Statistische Methoden in Suchen nach R-Parität erhaltender Supersymmetrie mit dem ATLAS-Detektor*, Frühjahrstagung der DPG, Karlsruhe, 2011.

[11] A. Strübig, S. Caron, and M. Rammensee, *Constraints on the pMSSM from searches for squarks and gluinos by ATLAS*, JHEP **1205** (2012) 150, arXiv:1202.6244 [hep-ph].

[12] ATLAS Collaboration, *Search for supersymmetry with jets and missing transverse momentum: Additional model interpretations*, Tech. Rep. ATLAS-CONF-2011-155, CERN, Geneva, Nov, 2011.

[13] ATLAS Collaboration, *Combined exclusion reach of searches for squarks and gluinos using final states with jets, missing transverse momentum, and zero or one lepton, with the ATLAS detector in* $\sqrt{s} = 7$ *TeV proton-proton collisions*, Tech. Rep. ATLAS-CONF-2011-064, CERN, Geneva, Apr, 2011.

[14] ATLAS Collaboration, *SUSY Searches at ATLAS in Multilepton Final States with Jets and Missing Transverse Energy*, Tech. Rep. ATLAS-CONF-2011-039, CERN, Geneva, Mar, 2011.

[15] M.Rammensee, *Untersuchung multi-leptonischer Endzustände mit fehlender transversaler Energie am ATLAS Detector und deren statistische Interpretation*, Frühjahrstagung der DPG, Bonn, 2010.

Table of contents

Chapter 1

Introduction

In the past few decades experimental observations and theoretical considerations converged into a set of equations and parameters called the Standard Model of particle physics (SM). The SM is a very successful theory of elementary particles and their interactions down to length scales of approximately 10^{-17} cm or equivalently up to energies of approximately 1 TeV. The Large Hadron Collider (LHC) [16] probes the SM in the TeV range. In 2010 and 2011 it collided protons with a center of mass energy of 7 TeV and in 2012 of 8 TeV and is designed to reach up to 14 TeV. The collisions are recorded by several experiments, one of them being ATLAS [17], which is a multipurpose detector with a forward-backward symmetric cylindrical geometry and nearly 4π coverage. The recently discovered particle [18, 19] bearing a mass of approximately 125 GeV seems to be compatible with a standard model Higgs boson and thus would close the last undiscovered gap of the SM.

If physics beyond the SM manifests at the TeV scale, the LHC may be sensitive to it. In theories including Supersymmetry (SUSY) new particles may be produced copiously at the LHC. In most phenomenological SUSY models the production of supersymmetric particles at the LHC is dominated by squark-squark, squark-anti-squark, squark-gluino and gluino-gluino pair production. Squarks are the super-partners to quarks and gluinos the super-partners to the gluons. These particles decay subsequently into the Lightest Supersymmetric Particle (LSP). Assuming the LSP is stable, it escapes the detector unseen, thus leading to final states with jets and missing transverse momentum ($E_{\mathrm{T}}^{\mathrm{miss}}$).

This thesis covers a set of subsequent analyses by ATLAS in final states with jets and missing transverse momentum and a veto on leptons which were triggered by the successful data acquisition of the LHC and ATLAS. The single analyses correspond to integrated luminosities of $35\,\mathrm{pb}^{-1}$ [1], $165\,\mathrm{pb}^{-1}$ [2, 3], $1.04\,\mathrm{fb}^{-1}$ [4] and $4.7\,\mathrm{fb}^{-1}$ [5] at 7 TeV center of mass energy and $5.8\,\mathrm{fb}^{-1}$ [6, 7] at 8 TeV center of mass energy.

Given the cost and the effort put into the LHC experiments it is absolutely mandatory to infer the most information possible from the data. In this thesis special emphasis is given on the mathematical modelling of the measurement within the likelihood framework and on hypothesis testing. The search methods for signatures of supersymmetric particles at this stage of the experiment are optimized for very broad bumps in $E_{\mathrm{T}}^{\mathrm{miss}}$ based distributions. As the $E_{\mathrm{T}}^{\mathrm{miss}}$ based distributions are prone to a lot of systematic uncertainties, the most robust choice to analyze the data is to define signal regions where counting experiments

are carried out.

The thesis is structured as follows. The standard model of particle physics is described in Chap. 2 and the supersymmetric extension to it in Chap. 3. The experimental setup including the LHC and ATLAS are described in Chap. 4. The signatures of SM and supersymmetric processes in proton-proton collisions are discussed in Chap. 5. The analysis of the complete data set taken at 7 TeV center of mass energy corresponding to a integrated luminosity of $4.7\,\text{fb}^{-1}$ is described in detail in Chap. 6. Within this section the background estimation technique, hypothesis testing and the impact of the searches on supersymmetric model parameters are discussed. A summary and outlook is given in Chap. 7.

Tests towards improved analysis models are described in Appendix A. The sensitivity of these searches to other beyond SM scenarios is exemplified in Appendix B, where an additional interpretation in the context of a minimal universal extra dimensions model is shown. A combination of the analysis described in the main text requiring a lepton veto and one with a requirement of exactly one lepton is shown in Appendix C. A search in a dedicated multi-lepton final state is presented in Appendix D.

Chapter 2

The Standard Model of particle physics (SM)

The particle content of the SM is outlined briefly in Sec. 2.1. A review of the SM is given in Ref. [20]. The theoretical formulation is briefly summarized in Sec. 2.2 and Sec. 2.3, a review is given, e.g., in Refs. [21, 22]. The chapter closes with a review of the current status of the SM in Sec. 2.4.

2.1 Particle content of the SM

Weak, electromagnetic and the strong interaction are responsible for the forces between particles by mediating bosonic particles. The SM is a gauge theory with gauge group $SU(3)_C \otimes SU(2)_L \otimes U(1)_Y$. Fundamental particles are fermions and bosons. The first generation of the fermionic particle content of the SM is summarized in Fig. 2.1. These are the left chiral quarks (u_L, d_L) and their anti-particles $(\bar{u}_R, \bar{d}_R)$, the left chiral neutrinos and electrons $(\nu_{e,L}, e_L)$ and their anti-particles $(\bar{\nu}_{e,R}, \bar{e}_R)$ and the right chiral quarks and electron (u_R, d_R, e_R) and their anti-particles $(\bar{u}_L, \bar{d}_L, \bar{e}_L)$. L, R stands for left, respectively right chiral fermions. Leptons are fermions which interact only electroweakly. Listed are the third component $I_{3,W}$ of the weak isospin $\mathbf{I}_W$ connected to SU(2), the weak hyper-charge Y_W connected to U(1) and the electric charge Q. They are connected via:

$$Q = I_{3,W} + Y_W/2 \tag{2.1}$$

In SU(3) each quark flavour belongs to the fundamental color representation (3), the anti-quarks to (3∗) and the gluons to (8). The strong charges associated to these representation are usually denoted blue(b), red(r) and green(g) for the quarks and anti-blue $\left(\bar{b}\right)$, anti-red $(\bar{r})$ and anti-green $\left(\bar{b}\right)$ for the anti-squarks. The eight independent gluon states can be represented by a set of superpositions $(r\bar{b} + b\bar{r})/\sqrt{2}$, $-i(r\bar{b} - b\bar{r})/\sqrt{2}$, $(r\bar{g} + g\bar{r})/\sqrt{2}$, $-i(r\bar{g} - g\bar{r})/\sqrt{2}$, $(b\bar{g} + g\bar{b})/\sqrt{2}$, $-i(b\bar{g} - g\bar{b})/\sqrt{2}$, $(r\bar{r} - b\bar{b})/\sqrt{2}$ and $-i(r\bar{r} + g\bar{g} - 2b\bar{b})/\sqrt{6}$.

Fermions come in three families with exactly the same quantum numbers as the first generation. The electron e, the muon μ and the tau τ and their corresponding neutrinos (ν_e, ν_μ, ν_τ) are ordered in three families. Right chiral neutrinos or left chiral anti-neutrinos may exist as neutrinos do have a mass

Name	$I_{3,W}$	Y_W	Q	color charge
u_L	$1/2$	$1/3$	$2/3$	r,g,b
d_L	$-1/2$	$1/3$	$-1/3$	r,g,b
$\nu_{e,L}$	$1/2$	-1	0	0
e_L	$-1/2$	-1	-1	0
u_R	0	$4/3$	$2/3$	r,g,b
d_R	0	$-2/3$	$-1/3$	r,g,b
e_R	0	-2	-1	0
$\bar{u}_R$	-1/2	-1/3	$-2/3$	$\bar{r},\bar{g},\bar{b}$
$\bar{d}_R$	$1/2$	-1/3	$1/3$	$\bar{r},\bar{g},\bar{b}$
$\bar{\nu}_{e,R}$	-1/2	1	0	0
$\bar{e}_R$	$1/2$	1	1	0
$\bar{u}_L$	0	$-4/3$	$-2/3$	$\bar{r},\bar{g},\bar{b}$
$\bar{d}_L$	0	$2/3$	$1/3$	$\bar{r},\bar{g},\bar{b}$
$\bar{e}_L$	0	2	1	0

Table 2.1: First generation of fermionic content of the SM, listed are both the particle and anti-particle sector.

different from zero. Quarks are fermions, which in addition carry the strong charge. The up type quarks occur as well in three families up, charm and top (u,c,t) and the down type quarks are labelled down, strange and bottom (d, s, b).

The gauge eigenstates of the electroweak interaction are the W bosons $W^{\pm}$, W^0 and the B^0 boson. The Higgs particle H^0 is the manifestation of a scalar field introduced to the SM to give masses to the particles via spontaneous symmetry breaking.

The W^0 and the B^0 mix to fields that can be identified with the mass eigenstates Z and the massless photon γ. Effective mediating particles are the photon γ, the Z boson and the $W^{\pm}$ bosons for the electroweak and the gluon g for the strong force. In Tab. 2.2 the masses of the particle of the SM are summarized. The heaviest particle found to date is the top quark with 172.5 GeV. The massive $W^{\pm}$ and Z have masses of 80.4 GeV and 91.2 GeV, respectively. Particle masses are taken from Ref. [20]. The Higgs particle mass was not measured yet, but a recent observation of a new particle [18, 19] indicates that its mass could be around 125 GeV.

2.2 Theoretical formulation of the SM

The SM is formulated in the language of Quantum Field theory (QFT). It is based on the principle of least action and the fundamental symmetries of special relativity and quantum mechanics. In classical mechanics the trajectory from time t_0 to t' that minimizes the action is identified to be the physical one. The action A is defined as the integral of a Lagrange density $\mathcal{L}$ which is in general a function of the space three-vector, the time and its derivative with respect to time. Minimizing the action leads to the equations of motion. In classical field theory the trajectory is replaced by a "history" of field configurations. The

Name	mass
γ	-
$W^{\pm}$	80.4 GeV
Z	91.2 GeV
gluons	-
H^0	(∼125 GeV)
$e^{\pm}$,$\mu^{\pm}$,$\tau^{\pm}$	0.51, 105.7, 1776.8 MeV
ν_e,ν_μ,ν_τ	$<$ 2 eV
u, c, t	∼ 2.2 MeV, ∼ 1.3 GeV, ∼ 172.5 GeV
d, s, b	∼ 4.7 MeV, ∼ 90 MeV, ∼ 4 GeV

Table 2.2: Masses (or upper limits on masses) of the particles of the SM.

action can be written as:

$$A = \int \mathcal{L}(\phi, \frac{\partial \phi}{\partial x}) d^4x \tag{2.2}$$

with L being the Lagrangian density or simply Lagrangian and ϕ being a field.
In quantum mechanics the principle of least action is the same, but trajectories are interpreted in a different way, that is as amplitudes of a probabilistic theory. In this sense an amplitude is a complex number which square represents a probability. A probabilistic amplitude is e.g. $-\frac{i}{\hbar}A$. A difference to the classical approach is that all possible amplitudes are summed over, not only the one trajectory which minimizes the action. The extension to quantum field theory is the same as in classical theories, that is the integral over the 4D space-time rather than only over time. $|i\rangle$ represents the initial state field configuration at time t_0 and $|f\rangle$ represents the final state configuration at time t_1. a_i stands for the value of the i-th infinitesimal cell. The integral of the action sums over all possible field configurations of the values a_i in the infinitesimal cells.
A probabilistic theory can be set up with the help of the path integral formalism. The contribution of a history (or a set of field configurations leading to $|f\rangle$ at time t_1 starting from $|i\rangle$ at time t_0) to the amplitude is assumed to be proportional to $e^{-\frac{i}{\hbar}A}$. Thus the total probability amplitude $A_{|i\rangle \to |f\rangle}$ to go from $|i\rangle$ to $|f\rangle$ can be written as:

$$A_{|i\rangle \to |f\rangle} = \sum_{history} e^{-\frac{i}{\hbar}\int \mathcal{L}(\phi, \frac{\partial \phi}{\partial x_\mu}) d^4x} \tag{2.3}$$

The formalism ensures Lorentz invariance in writing the action in dependence of a Lagrangian. The Lagrangian terms are given by symmetries and inference from experiments. Possible terms are dependent on the field ϕ and its derivatives $\frac{\partial \phi}{\partial x_\mu}$, e.g. the kinetic terms $\frac{1}{2}(\frac{\partial \phi}{\partial t})^2$ and $\frac{1}{2}(\frac{\partial \phi}{\partial x_i})^2$ with i denoting the space three vector indices. If ϕ is a scalar field other possible terms are a mass term $\frac{1}{2}m^2\phi^2$, which can be seen as a weight of a path in the history and higher order terms containing $g_3\phi^3$ or $g_4\phi^4$. The $g_3\phi^3$ and $g_4\phi^4$ term do correspond to 3 or 4 lines either outgoing or in-going, which is sketched in Fig. 2.1.

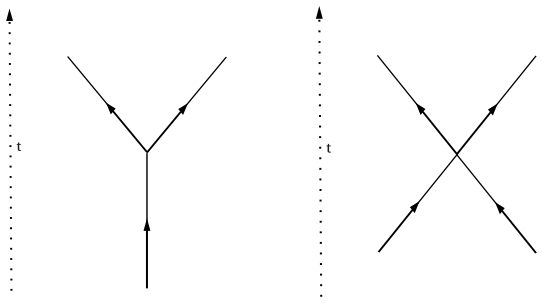

Figure 2.1: Sketch of allowed terms for a scalar field ϕ in a Lagrangian corresponding to 3 or 4 in- or outgoing lines.

2.3 The SM Lagrangian

Let $\psi(x)$ be a complex field. Local gauge invariance requires that $\psi(x)$ is invariant under the transformation:

$$\psi(x) \rightarrow \psi(x') = e^{i\epsilon(x)}\psi(x) \tag{2.4}$$

To fulfill this requirement gauge fields and covariant derivatives are introduced in the theory as described below.
The SM Lagrangian $\mathcal{L}$ can be separated into

$$\mathcal{L} = \mathcal{L}_{gauge,SU(2)_L\times U(1)_Y} + \mathcal{L}_{higgs} + \mathcal{L}_{leptons} + \mathcal{L}_{gauge,SU(3)_C} + \mathcal{L}_{quarks} \tag{2.5}$$

The single terms are:

- $\mathcal{L}_{gauge,SU(2)_L\times U(1)_Y}$ contains the gauge fields associated to the $SU(2)_L \times U(1)_Y$ symmetry of the electroweak sector.

  $$\mathcal{L}_{gauge,SU(2)\times U(1)} = -\frac{1}{4}B_{\mu\nu}B^{\mu\nu} - \frac{1}{4}W^j_{\mu\nu}W^{j,\mu\nu} \tag{2.6}$$

  with the Lorentz indices μ and ν. $B_{\mu\nu} = \partial_\mu B_\nu - \partial_\nu B_\mu$ is the abelian field strength tensor corresponding to the $U(1)_Y$ symmetry. $W^i_{\mu\nu} = \partial_\mu W^i_\nu - \partial_\nu W^i_\mu - g_2\epsilon^{ijk}W^j_\mu W^k_\nu$ is the non-abelian field strength tensor corresponding to the $SU(2)_L$ symmetry and g_2 is the respective structure constant.

- $\mathcal{L}_{higgs}$ consist of the dynamical and the mass term of the Higgs sector.

  $$\mathcal{L}_{higgs} = (D_\mu\boldsymbol{\phi})^\dagger(D^\mu\boldsymbol{\phi}) + \mu_h^2\boldsymbol{\phi}^\dagger\boldsymbol{\phi} - \frac{\lambda}{4}(\boldsymbol{\phi}^\dagger\boldsymbol{\phi})^2 \tag{2.7}$$

  with $\boldsymbol{\phi}$ being a two component complex scalar field. By convention $\boldsymbol{\phi}$ is chosen to be $\boldsymbol{\phi} = \begin{pmatrix}\phi^+\\ \phi^0\end{pmatrix}$.
  The covariant derivative $D_\mu = \partial_\mu + i\frac{g_1}{2}Y_W B_\mu + i\frac{g_2}{2}\sigma^i W^i_\mu$ working on ϕ with g_1 being the structure constant of U(1). Y_W is the hypercharge from Eq. 2.1 and σ^i are the Pauli matrices[1]. $(D_\mu\phi)^\dagger(D^\mu\phi)$

[1]The Pauli matrices σ^i are $\boldsymbol{\sigma} = (\sigma^0, \sigma^1, \sigma^2, \sigma^3) = \begin{pmatrix}1 & 0\\ 0 & 1\end{pmatrix}, \begin{pmatrix}0 & 1\\ 1 & 0\end{pmatrix}, \begin{pmatrix}0 & -i\\ i & 0\end{pmatrix}, \begin{pmatrix}1 & 0\\ 0 & -1\end{pmatrix}$ and $\tilde{\boldsymbol{\sigma}} = (\sigma^0, -\sigma^1, -\sigma^2, -\sigma^3)$

is the dynamical term with † indicating the hermitian conjugate. μ_h is the higgs mass parameter and $\lambda > 0$ the higgs self coupling parameter. For $\mu_h^2 < 0$ the minimum of the potential is at $\boldsymbol{\phi} = \begin{pmatrix} 0 \\ v \end{pmatrix}$ with the vacuum expectation value(vev) $v = \sqrt{\frac{-\mu_h^2}{\lambda}}$. The non zero vacuum expectation value induces spontaneous symmetry breaking of the electroweak group $SU(2)_L \times U(1)_Y$ to the electromagnetic group $U(1)_{EM}$. $\boldsymbol{\phi}$ can be written in terms of the vev, the Higgs boson H and the goldstone modes $\phi_{1,2,3}$.

$$\boldsymbol{\phi} = \begin{pmatrix} \phi_1 + i\phi_2 \\ v + H + i\phi_3 \end{pmatrix} \tag{2.8}$$

The three goldstone modes are absorbed into the massive gauge bosons $W^\pm$ and Z. The masses of the massive gauge bosons, the coupling constants and the vev are connected via:

$$\frac{M_W}{M_Z} = cos(\theta_W) \tag{2.9}$$

with θ_W being the weak mixing angle $\theta_W = arctan(\frac{g_1}{g_2})$

- $\mathcal{L}_{leptons}$ holds the dynamical $\mathcal{L}_{leptons,dyn}$ and the mass terms $\mathcal{L}_{leptons,mass}$ of the leptons.

$$\mathcal{L}_{leptons} = \mathcal{L}_{leptons,dyn} + \mathcal{L}_{leptons,mass} \tag{2.10}$$

Fermions can be represented by left or right chiral two-component Weyl spinors, e.g e_L and e_R denoting the left and right handed electron, respectively.

$$\mathcal{L}_{leptons,dyn} = \sum_{a \in e,\mu,\tau} \bar{\boldsymbol{L}}_L^a \tilde{\sigma^\mu} i D_\mu \boldsymbol{L}_L^{a,T} + \sum_{a \in e,\mu,\tau} \bar{E}_R^a \sigma^\mu i D_\mu E_R^a + (h.c.) \tag{2.11}$$

with $\boldsymbol{L}_L^a = (\nu_{e,L}, e_L), (\nu_{\mu,L}, \mu_L), (\nu_{\tau,L}, \tau_L)$ being the lepton doublets describing the left chiral neutrinos $\nu_{e,L}, \nu_{\mu,L}, \nu_{\tau,L}$ and left chiral e_L, μ_L, τ_L -leptons (T indicates the transponent vectors) and $E_R^a \in (e_R, \mu_R, \tau_R)$ the right chiral e_R, μ_R, τ_R -leptons. The $\boldsymbol{L}_L^a$ transform according to the representation $\boldsymbol{L}_L^a(1,2)_{-1}$that is (1) under $SU(3)_C$, (2) under $SU(2)_L$ and -1 under $U(1)_Y$. The E_R^a transform according to the representation $\boldsymbol{E_R^a}(1,1)_{-2}$.

The difference of left chiral to right chiral fields manifests in the covariant derivate. While the left chiral leptons transform under $SU(2)_L \times U(1)_Y$:

$$D_\mu \boldsymbol{L}_L^a = (\partial_\mu + i\frac{g_1}{2} Y_W B_\mu + i\frac{g_2}{2} \sigma^i W_\mu^i) \boldsymbol{L}_L^a \tag{2.12}$$

the right chiral fields only transform under $U(1)_Y$:

$$D_\mu E_R^a = (\partial_\mu + i\frac{g_1}{2} Y_W B_\mu) E_R^a \tag{2.13}$$

Leptons acquire masses through the Yukawa interaction of the scalar field $\boldsymbol{\phi}$ and the lepton field.

$$\mathcal{L}_{leptons,mass} = \sum_{a,b\in e,\mu,\tau} y_e^{a,b} \bar{\boldsymbol{L}}_L^a \boldsymbol{\phi} e_R^b + (h.c.) \tag{2.14}$$

with $y_e^{a,b}$ being the Yukawa coupling constants.

- $\mathcal{L}_{gauge,SU(3)_C}$ contains the gauge fields associated to the $SU(3)_C$ color symmetry of the strong sector.

$$\mathcal{L}_{gauge,SU(3)_C} = -\frac{1}{4} \sum_{a\in 1..8} G_{\mu\nu}^a G^{a,\mu\nu} \tag{2.15}$$

$\boldsymbol{G}$ is the spin 1 gluon field. $G_{\mu\nu}^a = \partial_\mu G_\nu^a - \partial_\nu G_\mu^a - i g_s f^{abc} G_\mu^b G_\nu^c$ is the non-abelian field strength tensor corresponding to the $SU(3)_C$ symmetry and g_s the coupling constant. f^{abc} are the structure constants of the $SU(3)_C$ and a, b and c are running over the 8 gluon states.

- $\mathcal{L}_{quarks}$ contains the dynamical and mass terms of the quarks.

$$\mathcal{L}_{quarks} = \mathcal{L}_{quarks,dyn} + \mathcal{L}_{quarks,mass} \tag{2.16}$$

Let f denote the flavor states and α the color states of the quarks. The dynamical term is given by

$$\mathcal{L}_{quarks,dyn} = \sum_{f,\alpha} \bar{\boldsymbol{Q}}_L^{f,\alpha} \tilde{\sigma^\mu} i D_\mu \boldsymbol{Q}_L^{f,\alpha,T} + \bar{U}_R^{f,\alpha} \sigma^\mu i D_\mu D_R^{f,\alpha} + \bar{D}_R^{f,\alpha} \sigma^\mu i D_\mu D_R^{f,\alpha} \tag{2.17}$$

with $\boldsymbol{Q}_L$ containing the left chiral quark content and U_R and D_R the right chiral quark content. The $\boldsymbol{Q}_L$ transform according to the representation $\boldsymbol{Q}_L(3,2)_{+\frac{1}{3}}$, the right handed quarks fields according to $U_R(3,1)_{+\frac{4}{3}}$ and $D_R(3,1)_{-\frac{2}{3}}$, respectively. The covariant derivatives working on $\boldsymbol{Q}_L$ take the form

$$D_\mu \boldsymbol{Q}_L = (\partial_\mu + i\frac{g_1}{2} Y_W B_\mu + i\frac{g_2}{2} \sigma^i W_\mu^i + i g_s T^a G_\mu^a) \boldsymbol{Q}_L \tag{2.18}$$

with T^a being the generators of $SU(3)_C$. As the right handed fields transform trivially under $SU(2)_L$ the covariant derivate working on the right handed parts D_R and U_R is given by:

$$D_\mu(D_R, U_R) = (\partial_\mu + i\frac{g_1}{2} Y_W B_\mu + i g_s T_A G_\mu^A)(D_R, U_R) \tag{2.19}$$

The quark masses are given by

$$\mathcal{L}_{quarks,mass} = \sum_{a,b\in family} y_d^{a,b} \bar{\boldsymbol{Q}}_L^{'a} \boldsymbol{\phi} D_R^{'b} + y_u^{a,b} \bar{\boldsymbol{Q}}_L^{'a} \tilde{\boldsymbol{\phi}} U_R^{'b} + (h.c.) \tag{2.20}$$

with $y_d^{a,b}$, $y_u^{a,b}$ being the Yukawa coupling constants. The indices a,b are running over the three family indices as in Eq. 2.14. The primes (') indicate the weak eigenstates.

The quarks underly the strong and the electroweak force. In the Lagrange density above the strong eigenstates and the weak eigenstates are distinguished. They turned out to be different by experimental observations. The transformation between both can be achieved with the help of the CKM matrix V_{CKM}.

$$V_{CKM} = \begin{pmatrix} V_{ud} & V_{us} & V_{ub} \\ V_{cd} & V_{cs} & V_{cb} \\ V_{td} & V_{ts} & V_{tb} \end{pmatrix} = \begin{pmatrix} 0.97425 \pm 0.00022 & 0.2252 \pm 0.0009 & (3.89 \pm 0.44) \times 10^3. \\ 0.230 \pm 0.011 & 1.023 \pm 0.036 & (40.6 \pm 1.3) \times 10^3 \\ (8.4 \pm 0.6) \times 10^3 & (38.7 \pm 2.1) \times 10^3 & 0.89 \pm 0.07 \end{pmatrix} \quad (2.21)$$

The observed values are all taken from the PDG [20]. V_{CKM} can be described by four independent observables, that are three mixing angles and one phase factor.

2.4 Status of the SM

Besides the parameters of the mechanism to include massive neutrinos there are 18 free parameters in the SM which are not explained by a deeper theory, their values are obtained by measurements. These are nine fermion masses, three mixing angles and one phase of the CKM matrix, the coupling constants of the electromagnetic, weak and strong interactions and the quadratic and quartic couplings parameters μ and λ of the Higgs sector. Fitting electroweak precision observables to all experimental observations to date [23, 24] gives information on how well the SM is consistent with the data. The most recent fit to the data including the potential Higgs particle of mass ~125 GeV yields a p-value of 0.07 [25]. However most of this small discrepancy does not origin from the measurement of the potential Higgs particle. The parameters with the largest pulls between the best fit and the data are the forward backward asymmetry parameter for b-quarks $A_{FB}^{0,b}$ with 2.5 σ, the partial Z-width ratio for b-quarks R_b^0 with -2.4 σ and the lepton asymmetry parameter A measured by the SLD collaboration $A_l(SLD)$ with -1.9 σ. There are some further open issues in the SM which are as follows.

- The anomalous magnetic moment of the muon shows a $\sim 3\sigma$ deviation between measurement and prediction [26] . This variable is sensitive to new physics beyond the SM, e.g. SUSY.
- Neutrinos are massless in the SM, but experiments showed that this is not the case. Beta decay spectra give a upper limit on the neutrino masses as listed in Tab. 2.2. Neutrino oscillation observations however indicate that their mass must be different from 0. Therefore the SM must be extended by a formalism that gives neutrino masses.
- In principle there are terms in the QCD Lagrangian allowed that violate CP symmetry. They can be expressed in dependence of an angle θ_{QCD} which is different from 0 in case of CP-violation. However, there is no CP violation observed in the QCD sector which introduces the so called strong CP problem.
- Gravity is not included in the SM. Attempts to construct a renormalizable theory including Gravity and the SM were not succesful so far.

- Dark matter is not explained by the SM. Experimental observation implies that there must be a component of dark matter and dark energy in the universe. There is no particle in the SM that can fulfil the dark matter density criterion.

Chapter 3

The supersymmetric extension to the SM

A first attempt to link half-integer spin particles and integer spin particles in particle physics was made in Ref. [27]. An algebra to describe the observed particles to date was developed, thus baryons and mesons were grouped into a representation. To achieve this a Baryon number changing operator was introduced which can be seen as a first attempt to connect half-integer spin particles to integer spin particles. Asking more fundamentally the authors of Ref. [28] discussed an extension to the Poincare symmetry or a higher degree of symmetry. They extended the algebra of the Poincare group by additional generators of "spinor translations". Their analysis of this algebra showed that parity is not conserved. In the development of string theory a two dimensional supersymmetry was introduced in Refs. [29–32]. A major development towards state-of-the-art supersymmetric theories has been published in Ref. [33,34], where a four dimensional theory emerged together with a proposal for a Lagrangian behaving invariant under "super-gauge" transformations. They showed that the proposed model is renormalizable and massive particles are allowed.
A short introduction to SUSY is given in Sec. 3.1. The minimal realization of a theory with SUSY is discussed in Sec. 3.2. The chapter closes with Sec. 3.3 listing some properties of models including SUSY.

3.1 Introduction to supersymmetry

An introduction to SUSY is given, e.g., in Refs. [35–37]. Supersymmetry relates fermions to bosons and vice versa. The generators of the symmetry $\boldsymbol{Q}, \boldsymbol{Q}^\dagger$ turn bosonic states $|b\rangle$ into fermion states $|f\rangle$ and fermion states into bosonic states [35].

$$\begin{aligned} \boldsymbol{Q}\,|b> &\rightarrow |f\rangle \\ \boldsymbol{Q}^\dagger\,|f\rangle &\rightarrow |b\rangle \end{aligned} \tag{3.1}$$

$\boldsymbol{Q}, \boldsymbol{Q}^\dagger$ and can be expressed in annihilation and creation operators of fermions c and $c^\dagger$ and bosons a and $a^\dagger$. Simple versions of the operators $\boldsymbol{Q}$ and $\boldsymbol{Q}^\dagger$ could take the form $Q \sim a^\dagger c$ and $Q^\dagger \sim c^\dagger a$.
The algebra part describing space time symmetries of the SM is given by the generators of special relativity (or Lorentz symmetry) M and the generators of translations P and its commutation relations.

Adding to this algebra the commutation relation (with spinor indices suppressed)

$$\{\boldsymbol{Q}, \boldsymbol{Q}^{\dagger}\} = P_{\mu} \tag{3.2}$$

with $\boldsymbol{Q}, \boldsymbol{Q}^{\dagger}$ being two component spinors a closed "super-algebra" can be defined. This algebra extends the normal space time symmetries.
It turned out that theories including supersymmetry can be described by expanding the space-time coordinates with Grassman numbers $\theta, \bar{\theta}$ describing the supersymmetric transformations [38]. The Lagrangian is replaced by a Super-Lagrangian. The Super-Lagrangian depends on θ and $\bar{\theta}$ and their derivatives. Super-fields $\boldsymbol{\phi}(\boldsymbol{x}, \theta, \bar{\theta})$ have to be introduced. Chiral super-fields obey the constraint

$$D^{\dagger}\boldsymbol{\phi}(\boldsymbol{x}, \theta, \bar{\theta}) = 0 \tag{3.3}$$

It can be shown that a chiral super-field $\boldsymbol{\phi}$ takes then the form:

$$\boldsymbol{\phi} = \phi(\boldsymbol{x}^{'}) + \sqrt{(}2)\theta\psi(x^{'}) + \bar{\theta}\theta F(x^{'}) \tag{3.4}$$

with ϕ being a complex scalar field, ψ a two-component Weyl fermion field and F an auxiliary field. $x^{'}$ are shifted space time coordinates depending on θ and $\bar{\theta}$. The action A expands to an integral over $\boldsymbol{x}, \theta$ and $\bar{\theta}$.

$$A = \int \mathcal{L}(\boldsymbol{x}, \theta, \bar{\theta}) dx^4 d\theta d\bar{\theta} \tag{3.5}$$

In a chiral theory the action takes again the form $A = \int \mathcal{L}(\boldsymbol{x}, \frac{\partial}{\partial x_{\mu}}) dx^4$ after integration over θ and $\bar{\theta}$. Within this framework it is possible to order the SM particles and their potential supersymmetric particles into super-mulitplets. A super-multiplet can be described by a chiral super-field.

3.2 The Minimal Supersymmetric Standard Model (MSSM)

The Minimal Super-Symmetric Model(MSSM) [39–43] is constructed so that the minimal number of particles occur. The Super-Lagrangian is discussed in Sec. 3.2.1. A quantum number to conserve lepton and baryon numbers, called R-Parity is introduced in Sec. 3.2.2. Terms leading to supersymmetry breaking are discussed in Sec. 3.2.3 and the particle content of the MSSM in Sec. 3.2.4.

3.2.1 Lagrangian

Let $\boldsymbol{Q}$, $\boldsymbol{U}$, $\boldsymbol{D}$, $\boldsymbol{L}$ and $\boldsymbol{E}$ be the matter fields of Sec. 2.3 with all color, family and chirality indexes suppressed. These are part of the chiral super-fields $\tilde{\boldsymbol{Q}}$, $\tilde{\boldsymbol{U}}$, $\tilde{\boldsymbol{D}}$, $\tilde{\boldsymbol{L}}$ and $\tilde{\boldsymbol{E}}$ belonging to chiral super-multiplets each containing the SM matter particles with spin $\frac{1}{2}$ and the super-partners to them with spin 0. Supersymmetric partners to the SM particles are marked with a tilde, their anti-particles are marked with a

tilde and a star(*). For example the super-field $\tilde{\boldsymbol{L}}_{\boldsymbol{e,L}}$ containing the left handed electron e_L and its super-partner the left selectron $\tilde{e}_L$ can be written as $\tilde{\boldsymbol{L}}_{\boldsymbol{e,L}} = \tilde{e}_L + \sqrt{2}\theta e_L + ...$
The super-potential of the MSSM in the Super-Lagrangian $S\mathcal{L}$ is:

$$S\mathcal{L}_{pot} = \sum_{a,b} -y_d^{a,b}\tilde{\boldsymbol{Q}}^a H_d \tilde{\boldsymbol{D}}^b + y_u^{a,b}\tilde{\boldsymbol{Q}}^a H_u \tilde{\boldsymbol{U}}^b - y_e^{a,b}\tilde{\boldsymbol{L}}^a H_d \tilde{\boldsymbol{E}}^b + (h.c.) \tag{3.6}$$

with $H_u = \begin{pmatrix} H_u^+ \\ H_u^0 \end{pmatrix}$ and $H_d = \begin{pmatrix} H_d^0 \\ H_d^- \end{pmatrix}$ after the Higgs mechanism. It is possible to chose $H_u = \frac{1}{\sqrt{2}}\begin{pmatrix} 0 \\ v_1 \end{pmatrix}$ and $H_d = \frac{1}{\sqrt{2}}\begin{pmatrix} v_2 \\ 0 \end{pmatrix}$ with v_1 and v_2 being two independent vacuum expectation values. The corresponding term in the Super-Lagrangian is

$$S\mathcal{L}_{Higgs} = \mu H_u H_d \tag{3.7}$$

3.2.2 R-Parity

The introduction of an addidtional $\mathbb{Z}_2$ symmetry, called R-Parity R [39–43] suppresses terms in the Lagrangian inducing baryon and lepton number violation. As these terms would lead to rapid proton decay R-Parity was introduced to stabilize the proton in supersymmetric theories. R is defined as

$$R = (-1)^{3(B-L)+2s} \tag{3.8}$$

with B being the Baryon number, L the Lepton number and the spin s. The quantum number R distinguishes between supersymmetric and SM particles. Supersymmetric particles carry R=-1 and SM particles R=1. This implies that supersymmetric particles are produced in pairs. The R-Parity assumption has a large impact on the topology of signatures from supersymmetric particles at the LHC. If R-Parity is violated signatures of supersymmetric particles may not be accessible with hadron colliders as was pointed out in, e.g. Ref. [44].

3.2.3 Supersymmetry breaking in the MSSM

If SUSY would be unbroken then superpartners to all SM particles must exist with the same mass. This have not been observed and therefore SUSY must be broken at a higher energy scale. In contrast to the spontaneous symmetry breaking mechanism in the SM induced by the form of the potential and the choice of parameters in the Higgs sector symmetry breaking in supersymmetry is more complex. Several mechanism were proposed among them, e.g., gravity or gauge mediated supersymmetry breaking. However for phenomenological considerations it is sufficient to induce supersymmetry breaking by introducing additional terms into the super-Lagrangian. In the MSSM the so called soft supersymmetry breaking terms including the gaugino masses take the form

$$S\mathcal{L}_{soft} = -\frac{1}{2}(M_3\tilde{g}\tilde{g} + M_2\tilde{W}\tilde{W} + M_1\tilde{B}\tilde{B} + c.c.) + ... \tag{3.9}$$

Names	spin 0	spin $\frac{1}{2}$	spin 1	spin $\frac{3}{2}$	spin 2
quarks, squarks(3 families)	$(\tilde{u_L}\ \tilde{d_L})$	$(\mathbf{u}_L\ \mathbf{d}_L)$			
	$\tilde{u_R}$	$\mathbf{u}_R$			
	$\tilde{d_R}$	$\mathbf{d}_R$			
leptons, sleptons(3 families)	$(\tilde{e_L}\ \tilde{\nu})$	$(\mathbf{e}_L\ \boldsymbol{\nu})$			
	$\tilde{e_R}$	$\mathbf{e}_R$			
higgs, higgsinos	$(H_u^+\ H_u^0)$	$(\tilde{H_u^+}\ \tilde{H_u^0})$			
	$(H_d^0\ H_d^-)$	$(\tilde{H_d^0}\ \tilde{H_d^-})$			
gluon, gluino		$\tilde{g}$	$\mathbf{g}$		
W, wino		$\tilde{W^\pm}$, $\tilde{W^0}$	$\mathbf{W}^\pm$, $\mathbf{W}^0$		
B, Bino		$\tilde{B^0}$	$\mathbf{B}^0$		

Table 3.1: Gauge Eigenstates of the MSSM super-multiplets. Particles of the SM are highlighted with bold letters.

with $\tilde{g}, \tilde{W}$ and $\tilde{B}$ describing the gluino, wino and bino, respectively. M_3, M_2 and M_1 are the gluino, wino and bino mass parameters.
The following terms are similar to the Yukawa mass terms in the SM Lagrangian, but with the fermion fields replaced by the corresponding scalar fields:

$$.. + a_d^{a,b}\tilde{Q}^{a,\dagger}H_d\tilde{D}^b + a_u^{a,b}\tilde{Q}^{a,\dagger}H_u U^b - a_e^{a,b}\tilde{L}^{a,\dagger}H_d E^b + c.c.) + ... \tag{3.10}$$

The trilinear couplings a_d, a_u, a_e are 3×3 matrices.
The "usual" mass terms for scalar fields (like in the SM Higgs sector proportional to $(scalar)^2$) are

$$... + \boldsymbol{m_Q^2}\tilde{Q}^\dagger\tilde{Q} + \boldsymbol{m_U^2}\tilde{U}^\dagger\tilde{U} + \boldsymbol{m_D^2}\tilde{D}^\dagger\tilde{D} + \boldsymbol{m_L^2}\tilde{L}^\dagger\tilde{L} + \boldsymbol{m_E^2}\tilde{E}^\dagger\tilde{E} + ... \tag{3.11}$$

with $\boldsymbol{m_Q^2}, \boldsymbol{m_U^2}, \boldsymbol{m_D^2}, \boldsymbol{m_L^2}, \boldsymbol{m_E^2}$ being the mass matrices of the squarks.
The soft supersymmetry breaking terms are completed by

$$.. + m_{H_u}^2 H_u^* H_u + m_{H_d}^2 H_d^* H_d + (bH_d H_u + c.c.) \tag{3.12}$$

with $m_{H_u}^2$, $m_{H_d}^2$ and b being Higgs mass parameters.

3.2.4 Particle content of the MSSM

In Tab. 3.1 the gauge eigenstates for the MSSM are summarized. There are four Higgs eigenstates H_u^+, H_u^0, H_d^0 and H_d^-. All particles have also antiparticles, which have opposite charge, but same mass and spin.
The super-partners to quarks with spin $\frac{1}{2}$ are scalar quarks with spin 0. Scalar leptons are super-partners to leptons.

Names	spin 0	spin $\frac{1}{2}$
squarks	$\tilde{u}_{L,R}$, $\tilde{d}_{L,R}$	
	$\tilde{c}_{L,R}$, $\tilde{s}_{L,R}$	
	$\tilde{b}_{1,2}$, $\tilde{t}_{1,2}$	
sleptons	$\tilde{e}_{L,R}$, $\tilde{\nu}_e$	
	$\tilde{\mu}_{L,R}$, $\tilde{\nu}_\mu$	
	$\tilde{\tau}_{1,2}$, $\tilde{\nu}_\tau$	
Higgs	h^0,H^0 , A^0 and $H^\pm$	
gluino		$\tilde{g}$
neutralino		$\tilde{\chi}^0_1$,$\tilde{\chi}^0_2$,$\tilde{\chi}^0_3$,$\tilde{\chi}^0_4$
chargino		$\tilde{\chi}^\pm_1$,$\tilde{\chi}^\pm_2$

Table 3.2: Mass eigenstates of the MSSM supersymmetric particles.

The mass eigenstates are summarized in Tab. 3.2. The super-partners of the Higgs particles and those of the gauge particles mix and form mass eigenstates, called neutralinos $\tilde{\chi}^0{}_i$ and charginos $\tilde{C}_i$. The uncharged sparticles $\tilde{H}^0_d$, $\tilde{H}^0_u$, $\tilde{B}^0$ and $\tilde{W}^0$ form the neutral eigenstates $\tilde{\chi}^0_1$, $\tilde{\chi}^0_2$, $\tilde{\chi}^0_3$ and $\tilde{\chi}^0_4$. The charged sparticles $\tilde{W}^\pm$, $\tilde{H}^+_u$ and $\tilde{H}^-_d$ form the charged eigenstates $\tilde{\chi}^\pm_1$ and $\tilde{\chi}^\pm_2$. Their order "i" is usually determined by their masses. Usually $\tilde{\chi}^0_1$ is the Lightest Supersymmetric Particle (LSP) and therefore important for collider physics as it will not deposit energy in a detector and give large contributions to the missing transverse energy. After electroweak symmetry breaking it turns out that there are 5 higgs mass eigenstates h^0, H^0 , A^0 and $H^\pm$. If one assumes that mixing between the first two families of scalar fermions are negligible, their gauge and mass eigenstates are the same. The sbottom, stops and stau gauge eigenstates are mixing each into two mass eigenstates.

3.2.5 Constrained MSSM (CMSSM)

In the CMSSM the mass spectrum is determined by only five parameters. The gaugino masses are assumed to be equal at the GUT energy scale: $M_1 = M_2 = M_3 = m_{1/2}$. The same assumption is made for the scalar masses: $m^2_Q = m^2_U = m^2_D = m^2_L = m^2_E = m^2_{H_u} = m^2_{H_d} = m^2_0$. A_0 fixes the trilinear couplings to the Yukawa couplings with e.g. $a_Q = A_0 y_Q$.

The mass spectrum is thus determined by the parameters m_0, $m_{1/2}$, A_0, $tan(\beta) = \frac{v1}{v2}$ and $sign(\mu)$. $sign(\mu)$ is the sign of the Higgs mass parameter.

3.3 Properties of supersymmetric models

In the calculation of the SM Higgs boson mass some parameters must be tuned to have a relatively light boson (as observed at ~125 GeV). The mass of the Higgs boson is sensitive to physics above the electroweak scale via loop contributions [45–48]. Without further fine tuning a light Higgs boson is only possible if there are no further loop corrections above the electroweak energy scale or by a cancellation effect. SUSY provides such a cancellation effect [43, 49–53], but as SUSY must be broken

the cancellation is not perfect. If supersymmetric particles have masses around the TeV scale, they will be observable at the LHC. The larger the masses of the supersymmetric particles the worse the cancellation effect gets, leading to another but reduced hierarchy problem. However supersymmetric theories have more properties that make them worth being tested at the LHC, these are:

- **Towards unification**

  In the MSSM it is possible for the coupling constants of the electroweak and strong forces to unify at an energy scale well below the Planck energy scale [52, 54–61]. In a scenario with no new physics other than MSSM-like supersymmetry between the TeV energy scale and the Planck energy scale, the coupling constant unify right below the Planck scale. The running of the couplings is shown in Fig. 3.1.

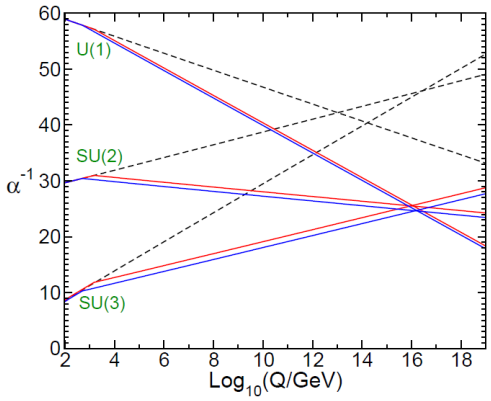

Figure 3.1: Group evolution of the coupling constants from Ref. [35]. The black dotted lines indicate the behavior in the SM and the red and blue lines the behavior in the MSSM under changing conditions of the particle masses, α_S and two-loop corrections.

- **Dark Matter**

  The most recent measurement of the cold dark matter density of WMAP [62] yields $\Omega_{CDM}h^2 = 0.1334 \pm 0.0056$. A cold dark matter particle candidate arises in SUSY quite naturally if one assumes in addition a conservation number for supersymmetric particles (R-Parity) [63, 64]. The LSP is a cold dark matter candidate as it is a neutral weakly interacting particle.

- **Similarities to other BSM models**

  Especially the R-Parity assumption shows similarities to other beyond SM models. Any theory which introduces a Z_2-Parity which distinguishes between SM and beyond SM particles has the effect that the lightest stable particle in the theory serves as dark matter candidate and the beyond SM particles are produced in pairs at the LHC. In collider physics this leads to typical SUSY signatures including large $E_{\mathrm{T}}^{\mathrm{miss}}$ and potentially jets, either from decay chains or from initial and final state radiation. The unified extra dimensions model [65–67] is such a szenario in which the lightest Kaluza-Klein particle is stable and serves as dark matter candidate. The main difference of this model to supersymmetric models is the spin of the BSM particles.

Chapter 4

The Large Hadron Collider(LHC) and the ATLAS Detector

4.1 The LHC

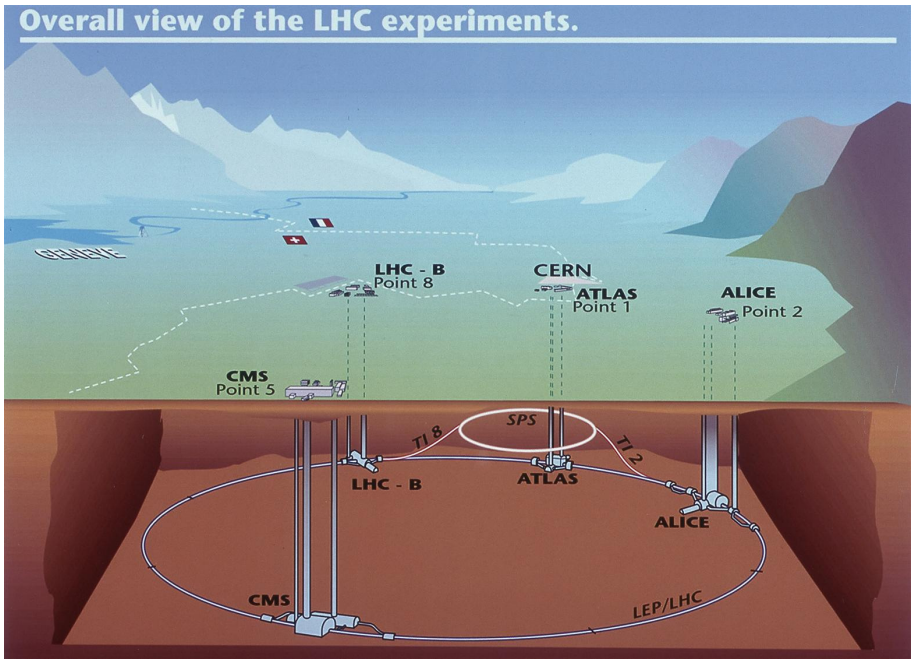

Figure 4.1: The Large Hadron Collider, picture from http://www.atlas.ch

The Large Hadron Collider (LHC) [16] is a ring with roughly 27 km circumference, in which protons or heavy-ions are circulated and is located approximately 100 m below the surface near to Geneva in Switzerland. Four main detectors are installed at interaction points around the circle, which is shown in Fig. 4.2. ATLAS and CMS are multi purpose detectors, whereas LHC-B is targeted at B-physics and Alice at heavy ion physics.

Before the injection to the LHC protons are accelerated in several experiments as depicted in Fig. 4.1. From the proton source the protons are first accelerated linearly by a radio frequency quadrupole then

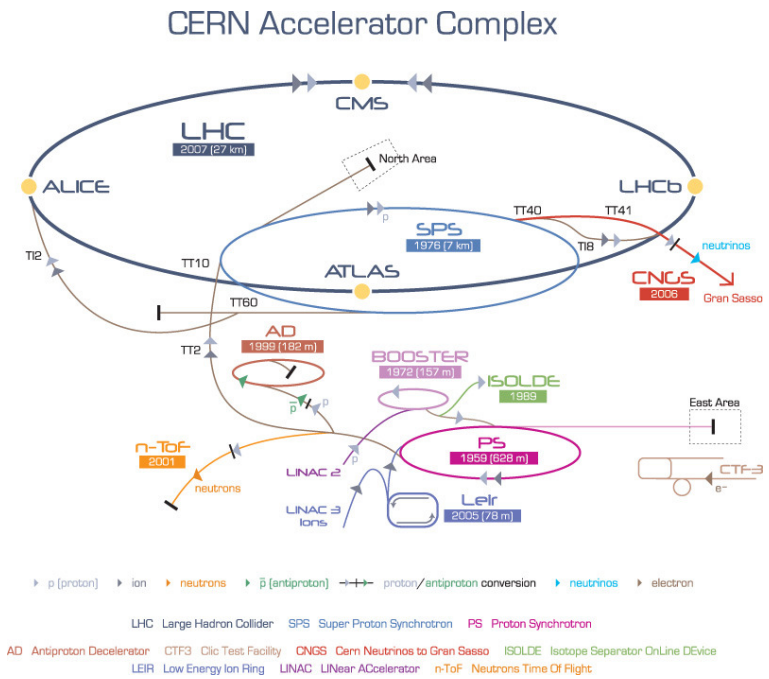

Figure 4.2: The Large Hadron Collider injection chain, picture from http://bigscience.web.cern.ch.

they are injected to the Linac2 accelerator where they gain energy up to 50 MeV. In the circular proton synchrotron booster they get further accelerated up to 1.4 GeV. They are then injected to the Proton Synchrotron (PS) and to an energy of 25 GeV at a velocity of 99.93% of the speed of light. The last acceleration step happens in the Super Proton Synchrotron (SPS), where the energy is increased to 450 GeV. In the Large Hadron Collider they reach up to 7 TeV of energy corresponding to a velocity very close to the speed of light.

There are two beam pipes close to each other where protons are injected in opposite directions. Eight super-conducting cavities per beam pipe are installed in several places to accelerate the protons. They are operated at a temperature of 4.5 K. Super-conducting dipole and quadrupole magnets are installed around the beam-pipe to keep the proton beams on track. These magnets have to be operated at very low temperatures of ~1.9 K. The magnetic field strength goes up to ~8.3 Tesla.

The intense cooling of the magnets requires a cooling system with tons of fluid He.

Protons can be accelerated up to energies of 7 TeV, thus resulting in a collision center of mass energy of 14 TeV. In 2010 and 2011 protons were collided with a center of mass energy of 7 TeV and in 2012 of 8 TeV. The design luminosity is $10^{34}\frac{1}{cm^2 s}$ and in 2012 it reached instantaneous luminosities of $\sim 10^{33}\frac{1}{cm^2 s}$. This mixture of high center of mass energy and high luminosity makes the LHC a promising experiment to explore a new energy range in HEP. The integrated luminosity of proton-proton collisions delivered by the LHC and recorded by the ATLAS detector is shown in a cumulative way in Fig. 4.3.

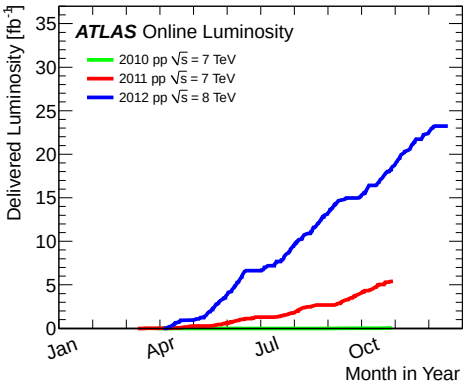

Figure 4.3: Integrated luminosity of proton-proton collisions recorded by ATLAS in 2010-2012.

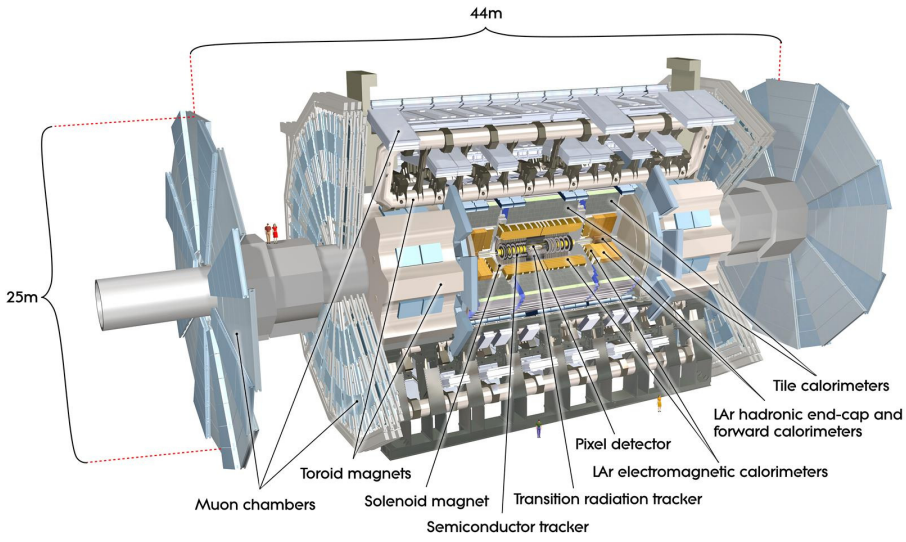

Figure 4.4: The ATLAS detector

4.2 The ATLAS Detector

The ATLAS detector [17] is a multi purpose detector with almost 4π coverage and is sketched in Fig. 4.4. It consists of the inner tracking system, the hadronic and electromagnetic calorimeters, the muon detection system and a system to provide magnetic fields.

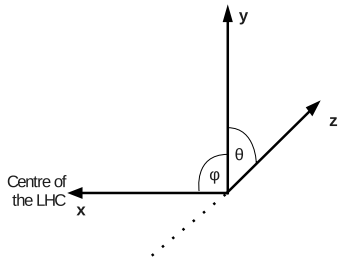

Figure 4.5: Coordinate system of the interaction point

In Fig. 4.5 a scheme of the interaction point and the system of coordinates is depicted. The z-axis is the direction of the beam axis, the x-y plane is perpendicular to it and the x-axis is pointing into the middle of the LHC ring. ϕ measures the angle around the beam axis and θ measures the angle from the beam axis . Pseudo-rapidity $\eta = -ln\ tan(\frac{\theta}{2})$ is often used instead of θ, as it is invariant under Lorentz boosts along the beam direction. R is the pseudo-rapidity-azimuthal angle and defined as $R = \sqrt{(\theta)^2 + (\phi)^2}$.

4.2.1 Inner Detector

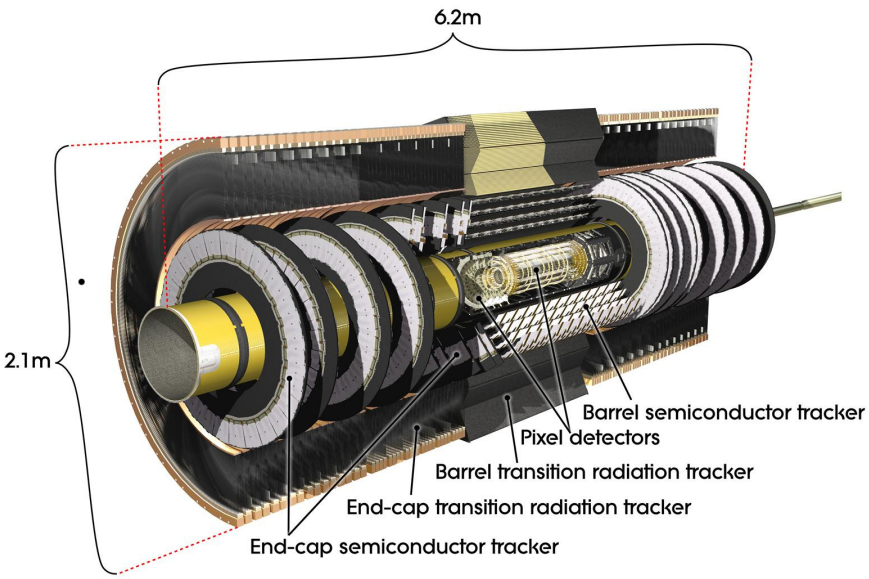

Figure 4.6: Sketch of the inner detector.

The inner detectors purpose is to track and measure momenta and charge of particles and is depicted in Fig. 4.6. It covers the pseudo rapidity range $|\eta| < 2.5$ and has full ϕ coverage. A silicon pixel detector, a

silicon micro strip detector (SCT) and a transition radiation tracker (TRT) are built inside a 2 T magnetic field, which provides the magnetic field to bend charged particles. A charged particle traversing the detector would typically have three hits in the pixel detector, eight in the SCT detector and more than 30 in the TRT.
Close to the interaction point the particle flux density is largest and a high resolution pixel detector is installed. Three pixel layers are surrounding the beam pipe in $R-\phi$ segments in the barrel region. In the end cap pixel layers are arranged perpendicular to the beam axis. The size of an average pixel is $50\times400\,\mu m^2$ and is made out of silicon. Of special importance is the radiation hardness of the innermost pixels layers. The pixels are exposed to high radiation doses over a long time due to the high luminosity. The high granularity of the pixels and arrangement in several layers allow for very good resolution of charged particles, ionizing the silicon sensors. The pixel detector has a resolution of $\sim12\,\mu m$ in the $R-\phi$ coordinate, and $\sim110\,\mu m$ in the z coordinate resulting in total of ~80 million readout channels.
In the Semiconductor Tracker (SCT) silicon micro strip detectors are used. The particle flux density is reduced compared to the pixel detector area, thus silicon strips instead of pixels are used, decreasing the number of readout channels. The resolution per module in the barrel is $\sim17\,\mu m$ in $R-\phi$ and $\sim580\,\mu m$ in z. The total number of readout channels is ~6 million.
The Transition Radiation Tracker(TRT) forms the outer layer of the inner detector. The components of the TRT are straws of diameter of 4 mm filled with gas mixture based on Xenon, which serves as ionizing material. Charged particles ionize the gas and the time drift of the charged cluster to the wire in the middle of the straw is measured. The TRT has a resolution in $R-\phi$ of $130\,\mu m$ per straw. Radiator material is filled in the gaps between the straws, thus transition radiation occurs when an electron crosses medias. Thus electrons can be identified with high precision. For electron energies above 1 GeV, the TRT has an electron identification efficiency of ~90 %. The number of readout channels is ~350k.

4.2.2 Calorimetry

Calorimeters are used to measure energy deposition and position of electrons, photons, charged and neutral hadrons. The components of the calorimeter are arranged to cover full ϕ symmetry and are depicted in Fig. 4.7. They do as well measure information about the missing transverse energy which is especially crucial for the analysis described later. The electromagnetic calorimeters in the ATLAS detector are the Liquid Argon (LAr) calorimeters in the barrel (EMB) and end-cap covering a range of $|\eta| < 3.2$. The LAr functions as ionizing material and lead is used as absorber. The thickness of more than 22 radiation lengths is sufficient for high energy jets and to suppress punch through (combined with the hadronic calorimeters) to the muon spectrometer. A radiation length is the mean time between two interactions. The efficiency of pion-photon and pion-electron is enhanced in the electromagnetic calorimeter due to the high spatial resolution and provides a precision η measurement. The energy resolution is $\sim \frac{\sigma_E}{E} = \frac{10\%}{E} \times 3\%$.

The tile scintillator hadronic calorimeter covers $|\eta| < 1.7$ and consists of iron with scintillators interleaved. It surrounds the EMB. The LAr hadronic end-cap calorimeter covers $1.5 < |\eta| < 3.2$. Radiation is much harder in the forward regions, thus LAr is used as ionizing material and Copper/tungsten

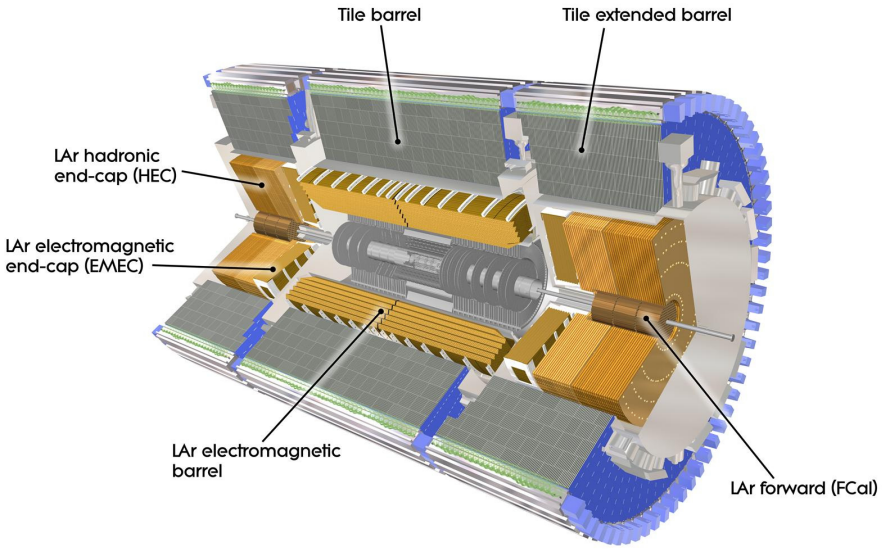

Figure 4.7: Sketch of the calorimeter system.

as absorber. The thickness is ∼10 radiation length in the barrel region. The spatial jet resolution is $\delta\phi \times \delta\eta = 0.1 \times 0.1$ and the energy resolution in the barrel region $\sim \frac{\sigma_E}{E} = \frac{50\%}{E} \times 3\%$.

The LAr forward detector ($3.1 < |\eta| < 4.9$) lies in the region with the highest radiation doses. It consist out of a electromagnetic and a hadronic part and is placed 1.2 m further away from the interaction point than the end-cap calorimeters.

4.2.3 Muon Spectrometer

Due to their high mass muons will only slightly interact in the calorimeter system and can therefore be detected separately in a muon detector system. Muons are bended by the magnetic field provided by the large super conducting air-core toroid magnets.
The Monitored Drift Tube (MDT) chambers and Cathode Strip Chambers (CSCs) are used for precision track measurements in η. MDT chambers consist of aluminum tubes with a wire in the center. The tubes are floated with a mixture of Argon and CO2. A muon ionizes the gas and electrons are moving towards the wire, due to the high voltage applied. The muon track is determined by measuring the drift time of the electrons. The MDTs are located in the barrel at $0 < |\eta| < 1.05$, in the end-cap at $1.05 < |\eta| < 2.7$ with the only exception in the inner-most end-cap where the CSC chambers take over.
The CSC chambers are located in the inner-most end-cap, closest to the beam-pipe at $2 < |\eta| < 2.7$ and have to operate under conditions with larger background.
Resistive Plate Chambers (RPC) cover $0 < |\eta| < 2.4$ and deliver trigger information in the barrel. A gas mixture is filled in between two resistive plates. A charged particle ionizes the gas mixture and the charge is collected at the plates through the high voltage applied. The drift time is very short compared

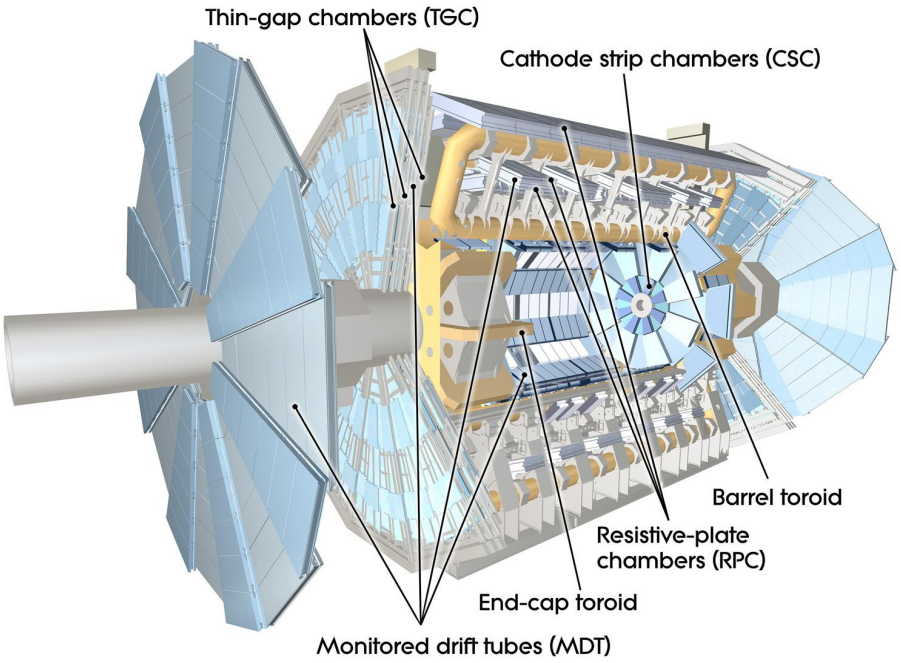

Figure 4.8: Sketch of the muon spectrometer.

to the one in the MDTs, so a fast response is ensured, which is needed for the trigger. The time resolution of the RPCs is $O(ns)$. Thin Gap Chambers (TGC) complete the muon trigger system and are installed in the end-cap. They deliver trigger information in the end-cap and the determination of the azimuthal coordinate. They function like multi-wire proportional chambers. The drift time of ionized particles is again very short to need trigger requirements.

4.2.4 Trigger and data acquisition system

The design bunch crossing rate of the LHC is 40 MHz with ~25 interactions per bunch crossing. The purpose of the ATLAS trigger system [68] is to reduce this enormous amount of information. The rate of recorded events is ~200 Hz and limited by processing of the data and offline storage. The trigger system has three levels as depicted in Fig. 4.9. Level 1 (L1) is a hardware trigger using information from the calorimeter and muon sub detectors, the second (L2) and third (Event Filter, EF) levels are software-based systems using information from all sub detectors. The combined L2 and EF is called High Level Trigger (HLT). The information from the muon spectrometer, the calorimeters and the inner detector is stored temporarily in front end pipelines. In the meantime a subset of information from the muon spectrometer and the calorimeters is fed to the L1 trigger system which takes the decision to keep the event or not within 2.5 μs. At design luminosity the L1 trigger reduces the rate to max. 75 kHz. In addition it defines Regions of Interest (RoI) which are fed to the HLT. In case an event gets accepted by L1 data from all detectors is stored in readout buffers and awaits the decision from L2. The L2 trigger system reduces the rate to ~3 kHz. If the L2 system accepts the event the information is fed to the event builder. The event builder combines the information from all sub detector and feeds the full

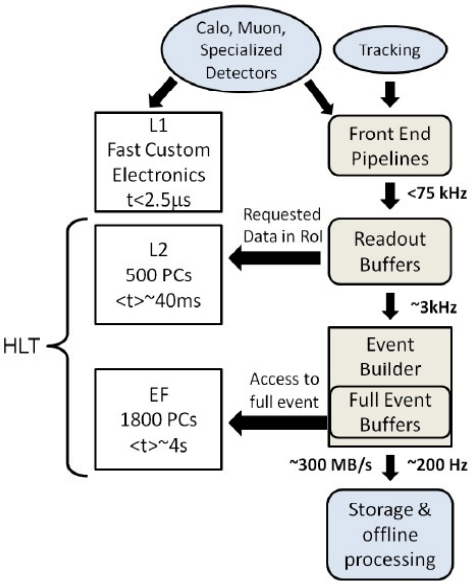

Figure 4.9: Sketch of the trigger system from Ref. [68].

event information to the EF. The EF reduces the rate to ~200 Hz, which is then stored for further offline reprocessing. Different data streams are defined based on the trigger type, they are called ”Egamma”, ”Muons”, ”JetTauEtmiss” and calibration streams.

.

Chapter 5

SM and SUSY signatures in proton-proton scattering at the LHC

5.1 SM signatures and cross sections

The description of hadron-hadron collisions can be split into regimes according to the scale of the momentum transfer. The area of large momentum transfer, where the matrix elements of the sub-process involved can be calculated from first order principle, is well described by pertubative QCD(pQCD). pQCD stops working at energy levels when confinement takes over, usually at ∼1 GeV. In the non-pertubative region at lower momentum transfer models are used to describe data.
Searches for supersymmetry require predictions of rates and distributions of observables sensitive to signatures of the new particles. The Monte Carlo method [69] is used to calculate predictions due to the probabilistic behavior of quantum physics ever since the development of computers. The description of proton-proton collisions at the LHC with MC generators can be separated in several parts, a review is given in Ref. [70]:

- **Hard sub-process**

  Beginning from the highest scale the hard sub-process can be calculated with pQCD. Partons of the proton are gluons and quarks. Deep inelastic proton-proton scattering can be described in terms of hard scattering of partons. Parton density functions describe the fraction of momentum carried by quarks and gluons. The primary processes are quark-(anti-)quark, quark-gluon and gluon-gluon reactions. The hard scattering processes are defined to be those with a large transverse momentum transfer and thus with a large angle θ perpendicular to the beam axis. The cross section of proton proton scattering to a final state X $\sigma_{pp\to X}$ can be expressed in terms of cross sections of hard processes $\hat{\sigma}_{ab\to X}$ with a,b being the partons of the proton involved:

$$\sigma_{pp\to X} = \sum_{a,b} \int dx_a dx_b f^a(x_a, \mu_F) f^b(x_b, \mu_F) \hat{\sigma}_{ab\to X} \tag{5.1}$$

x_a and x_b are the momentum fractions of the partons a and b, respectively, relative to the proton. f^a and f^b are the parton density functions (pdfs). The expansion of the cross section in terms of α_S yields:

$$\hat{\sigma}_{ab\to X} = \hat{\sigma}^0_{ab\to X} + \alpha_S \times \hat{\sigma}^1_{ab\to X} + \alpha_S^2 \times \hat{\sigma}^2_{ab\to X} + ... \tag{5.2}$$

The first order cross section is calculated like:

$$\hat{\sigma}^0_{ab\to X} = \int \frac{1}{2\hat{s}} \int |M_{ab\to X}|^2(\mu_F, \mu_R) \prod_{i\in X} \frac{d^3 p_i}{(2\pi)^3 2E_i} (2\pi)^4 \delta^{(4)}(p_a + p_b + \sum_{i\in X} p_i) \tag{5.3}$$

$\hat{s} = x_a x_b s$ with s being the center of mass squared. $|M_{ab\to X}|^2$ is the matrix element (ME) squared, μ_F the factorization scale and μ_R the renormalisaion scale. The dependency on μ_F and μ_R represents our lack of knowledge of all order of the perturbation series. The renormalization scale μ_R is set to an energy characteristic to the process. The DGLAP equations are used to describe the dependence of observables on the scales [71–73].

- **Parton shower**

  In the hard sub-process most of the particles underly QCD and thus can radiate gluons which itself can radiate other gluons and quark-anti-quark pairs. This is simulated by a parton shower (PS) algorithm starting at the scale of the hard sub-process and evolutes to lower scales. Most of the additional partons are emitted collinear or are soft.

- **Hadronization**

  At scales of ~1 GeV QCD confinement takes over and the perturbation series breaks down. The parton description must be replaced by a hadronization model which describes the formation of colorless states. Most of the hadrons are not stable with respect to the detector surrounding the interaction point and thus algorithms simulating the decay to lighter hadrons and finally stable particles were developed.

- **Jets**

  The signature that a hard sub-process with its parton shower and the subsequent hadronization leaves in a detector is bundled into a jet. The reconstruction of a jet in a detector via its energy depositions is done via a jet algorithm.

In the generation of spectra the pertubation series in Eq. 5.2 and the PS algorithms have to opposed. PS algorithms describe parton radiation as successive emission of particles. This works well in the soft and collinear regime. Opposed to this the calculation of ME is successful when the emission is well separated, but breaks done in the soft regime. Therefore several approaches exist in the algorithms used to make predictions of rates and spectra in proton-proton collisions. PYTHIA6 [74] is a classical example on a tool based on PS.

In Fig. 5.1 several measurement of the total cross section of SM processes ATLAS carried out so far

are listed and opposed to theoretical calculations[1]. The W and Z vector-boson inclusive cross sections were measured with 35 pb^{-1} of integrated luminosity. The top quark pair production cross-section uses up to 1.02 fb^{-1} of data. The single-top measurement uses 0.7 fb^{-1} of data, while the WZ measurement uses 1.02 fb^{-1} . The WW and ZZ measurements were made with the full 2011 dataset corresponding to ~5 fb^{-1} . The measurements are opposed to theoretical calculations at NLO or higher.

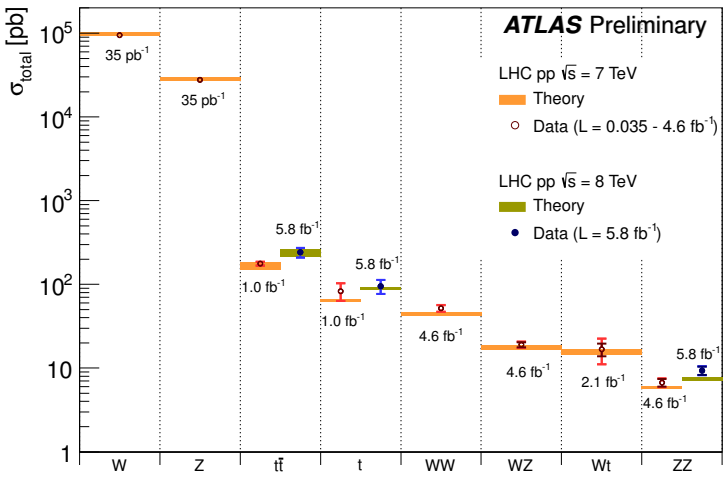

Figure 5.1: Summary of SM cross section measurements ATLAS carried out so far. The dark error bar represents the statistical uncertainty. The red error bar represents the full uncertainty, including systematics and luminosity uncertainties. All theoretical expectations were calculated at NLO or higher.

5.2 SUSY signatures and cross sections

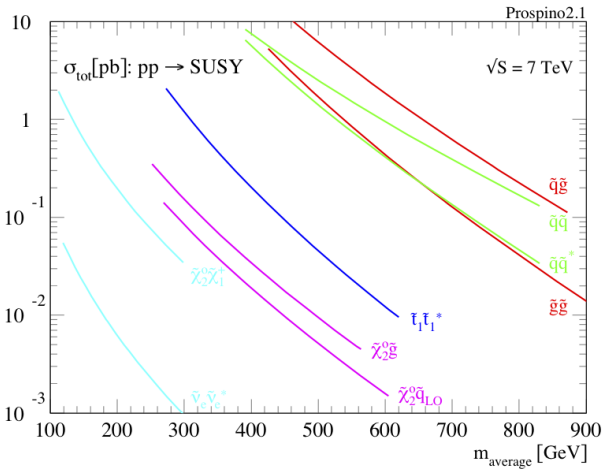

Figure 5.2: Cross section of various supersymmetric processes calculated with Prospino [75].

[1] from https://twiki.cern.ch/twiki/bin/view/AtlasPublic/CombinedSummaryPlots, March 2013)

In Fig. 5.2 the production cross section of various supersymmetric processes are plotted in dependence of their masses. The dominant production modes are squark-squark ($\tilde{q}\tilde{q}$), squark-anti-squark ($\tilde{q}\tilde{q}^*$), squark-gluino ($\tilde{q}\tilde{g}$) and gluino-gluino ($\tilde{g}\tilde{g}$) pair production. The Feynman graphs associated to these processes are depicted at LO in Fig. 5.3. Gluons are depicted with a curly line, gluinos with a curly line crossed by a straight line. Quarks are depicted with a solid line and an arrow, squarks with a dashed line and an arrow.

NLO order corrections can go up to 100 % of the LO cross section and usually have positive sign. The cross sections used in this thesis are calculated up to next-to-leading order in α_S, including the resummation of soft gluon emission at next-to-leading-logarithmic accuracy (NLO+NLL) [75–79]. The authors of Ref. [80] showed that even at NLO+NLL accuracy there are further terms that enhance the cross section by up to 30%. The SUSY signal cross sections used in this thesis are calculated following as close as possible the PDF4LHC [81] recommendations as described in Ref. [82], i.e. the mean of the envelope from several PDF sets. In these calculations two pdf sets were used, CTEQ6L1 [83] and MRST2007LO* [84].

The couplings of supersymmetric particles are the same as of SM particles. Gluinos decay to squarks and quarks. In a three body decay gluinos can directly decay via a virtual squark to two quarks and the neutralino. Squarks can decay to gauginos and quarks. In Fig. 5.4 an example of a mass spectrum of the particles of the MSSM from Ref. [85] is shown. The topology of the signatures seen at hadron colliders depends heavily on the mass spectra of the supersymmetric particles. The primary produced particles, gluinos and squarks, may decay to kinematically accessible other supersymmetric particles. In the example above gluino with a mass of ~600 GeV can decay to a squark $\tilde{u}_R$ at ~480 GeV and a jet. $\tilde{u}_R$ can decay further to the lightest chargino $\tilde{\chi}_1^{\pm}$ and a jet. $\tilde{\chi}_1^{\pm}$ further decays to the neutralino $\tilde{\chi}_1^0$ and a lepton.

Depending on the mass spectra there can be more complex topologies e.g. a $\tilde{\chi}_2^0$ decaying into a slepton-lepton pair, which decays further into a lepton pair plus the $\tilde{\chi}_1^0$. A typical signature leading to the topology investigated in this thesis is depicted in Fig. 5.5. A gluino pair is produced and each gluino decays into a squark and an anti-quark. The squarks are decaying into the lightest neutralino (depicted by a dashed line) and a quark. In the detector visible will be jets coming from the quark and anti-quarks and missing energy from the neutralinos $q\bar{q} \rightarrow jets + E_{\mathrm{T}}^{\mathrm{miss}}$.

The sensitivity to these kind of signatures were studied before the LHC started to acquire data, e.g. in Refs. [86], [8].

The spectra of SUSY signal samples used in this thesis are generated with Herwig++ [87], [88] or with MadGraph/PYTHIA6 [89, 90].

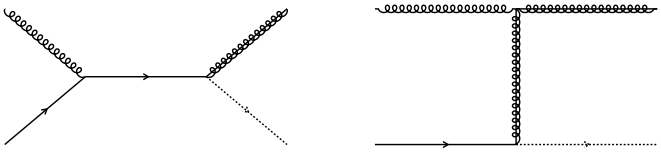

(a)

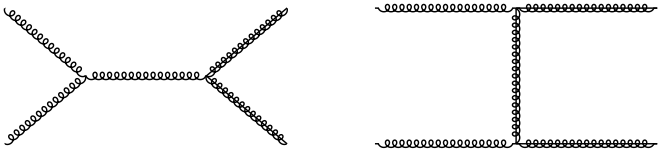

(b)

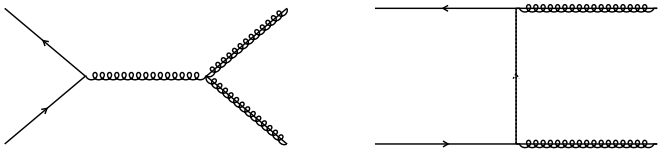

(c)

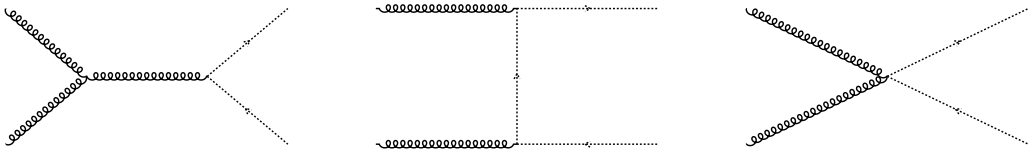

(d)

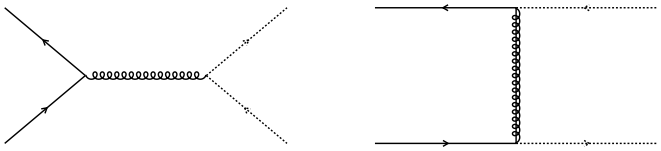

(e)

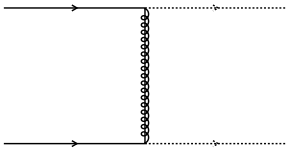

(f)

Figure 5.3: Feynman graphs depicting the pair production of supersymmetric particles at leading order. Diagrams with crossing lines in the final state are not drawn explicitly.

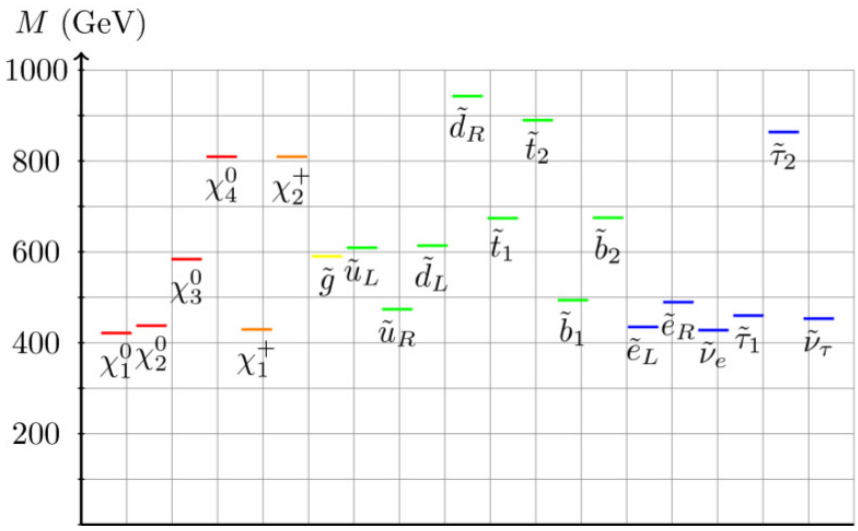

Figure 5.4: Example of spectrum of masses of supersymmetric particles in the MSSM.

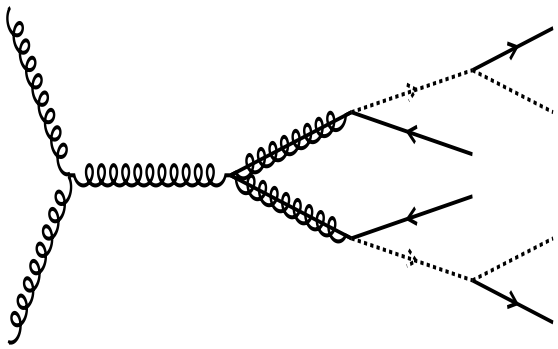

Figure 5.5: Feynman graph(s) of gluinos pair production decaying into anti-quarks and squarks, which itself decay into the lightest neutralino and quarks.

Chapter 6

Search for supersymmetric signatures with large missing transverse momentum, jets and a veto on leptons

6.1 Introduction

This search is targeted at heavy squarks and gluinos decaying into jets and neutralinos. Typical signatures are multiple jets and $E_{\mathrm{T}}^{\mathrm{miss}}$ from the neutralino. The jet multiplicity can range from two, e.g. squarks decaying directly to a neutralino and a jet, up to large multiplicities depending on cascade decays and initial or final state radiation. Examples of the production and decay modes to the first order are depicted in Tab. 6.1 and opposed to the minimal jet multiplicity in the final state in the search channels. Initial and final state radiation do increase the jet multiplicity in the final state, whereas soft jets due to small mass splittings or jets that fall out of the acceptance or kinematic selection of the analysis decrease the measured final state multiplicity. Thus the correspondence of the processes to the search channels listed in the table must not necessarily be true in the experiment.

Analyses channels are defined, ranging from an inclusive two jets and more selection up to six jets and more, labelled as channel A-E. The lower jet multiplicity channels focus on models characterized by squark pair production, intermediate jet multiplicities on squark pair and associated squark-gluino production and high jet multiplicities are optimized for gluino pair production and/or long cascade decay chains. In addition a separate two jets and more channel selection, labelled A* was defined to be more sensitive to compressed spectra by allowing the events to have a larger $E_{\mathrm{T}}^{\mathrm{miss}}$ component relative to the scalar sum of the p_{T} of the jets. This additional search channel was triggered by the study in Refs. [91,92] showing that initial state radiation jets can increase the sensitivity to these decay modes.

The properties of the supersymmetric signatures are condensed in the effective mass m_{eff}(incl.) variable which is defined to be the scalar sum of the transverse momenta p_{T} over all jets with $p_{\mathrm{T}} > 40\,\mathrm{GeV}$

Channel	Min. jet mult.	production	decay
A	2	$\tilde{q}\tilde{q}$	$\tilde{q} \rightarrow \tilde{\chi}_1^0 \mathrm{j}$
A*	2	$\tilde{q}\tilde{q}$,$\tilde{q}\tilde{g}$,$\tilde{g}\tilde{g}$	compressed spectra
B	3	$\tilde{q}\tilde{q}$,$\tilde{q}\tilde{g}$	$\tilde{q} \rightarrow \tilde{\chi}_1^0 \mathrm{q}$,$\tilde{g} \rightarrow \tilde{\chi}_1^0 \mathrm{qq}$
C	4	$\tilde{q}\tilde{q}$, $\tilde{q}\tilde{g}$,$\tilde{g}\tilde{g}$	$\tilde{g} \rightarrow \tilde{\chi}_1^0 \mathrm{qq}$, $\tilde{q} \rightarrow \tilde{\chi}_1^{\pm} q \rightarrow W^{\pm}\tilde{\chi}_1^0 \mathrm{q}$
D	5	$\tilde{q}\tilde{g}$,$\tilde{g}\tilde{g}$	$\tilde{g} \rightarrow \tilde{\chi}_1^0 \mathrm{qq}$, $\tilde{q} \rightarrow \tilde{\chi}_1^{\pm} q \rightarrow W^{\pm}\tilde{\chi}_1^0 \mathrm{q}$
E	6	$\tilde{g}\tilde{g}$	$\tilde{g} \rightarrow \tilde{\chi}_1^{\pm} qq \rightarrow W^{\pm}\tilde{\chi}_1^0 \mathrm{qq}$

Table 6.1: Examples on first order production and decay modes leading to final states with jets and $E_{\mathrm{T}}^{\mathrm{miss}}$ opposed to the search channels and the jet multiplicity per search channel. This is not a one to one correspondence as the jet multiplicity in the final event selection is modulo additional jet radiation, detector acceptance and reconstruction efficiency of jets.

and $E_{\mathrm{T}}^{\mathrm{miss}}$.

$$m_{eff}(incl.) = \sum_{p_{\mathrm{T}}>40\,GeV} p_{\mathrm{T}} + E_{\mathrm{T}}^{\mathrm{miss}} \tag{6.1}$$

This variable is used as the discriminating variable between signal and background. Each of the six channels is used to construct between one and three signal regions with tight, medium and/or loose meff (incl.) selections, giving a total of 11 SRs.

The event selection is depicted in Tab. 6.2 which is taken from Ref. [5] and detailed in section Sec. 6.6. $E_{\mathrm{T}}^{\mathrm{miss}}$ is required to be larger than 160 GeV. The hardest jet p_{T} must be larger than 130 GeV and the p_{T} of the other jets in the event 60 GeV, respectively 40 GeV as listed in the table. The cuts on the ratio of $E_{\mathrm{T}}^{\mathrm{miss}}$ and m_{eff} and on the angular separation $\Delta\phi(j_i, E_{\mathrm{T}}^{\mathrm{miss}})$ between the missing momentum vector in the transverse plane and the i-th jet are introduced solely to reject multi-jet background. Thus this analysis is designed to have very good rejection against this kind of background. Note that the m_{eff} definition in the ratio of $E_{\mathrm{T}}^{\mathrm{miss}}$ and m_{eff} cut is different from the final selection m_{eff} (incl.) variable. m_{eff} is defined as the scalar sum of $E_{\mathrm{T}}^{\mathrm{miss}}$ and all jets used in the given channel multiplicity, opposed to m_{eff} (incl.) where all jets with a p_{T} of 40 GeV are used. $\Delta\phi(j_i, E_{\mathrm{T}}^{\mathrm{miss}})$ is the angular separations between the missing momentum vector in the transverse plane($\mathbf{P}_{T,miss}$) and the jets. In channel A, A* and B, the selection requires $\Delta\phi(j_i, E_{\mathrm{T}}^{\mathrm{miss}})$ to be larger than 0.4 radians using up to three leading jets. In the other channels an additional requirement of $\Delta\phi(j_i, E_{\mathrm{T}}^{\mathrm{miss}})$ larger than 0.2 radians is applied to the remaining jets with p_{T} larger than 40 GeV to further suppress multi-jets background. In the final signal region boxes defined by the m_{eff} cuts in the last row counting experiments have been carried out to test if the data shows deviations from the background prediction.

The m_{eff} (incl.) distribution of all search channels are shown in Fig. 6.1. The Z+jets, W+jets, $t\bar{t}$ and diboson component are estimated via MC normalised to the integrated luminosity and the multi-jets background from the data driven method described in Sec. 6.7.3. Two supersymmetric model parameter points are shown as well to illustrate different topologies. Both points correspond to simplified models, that is not all possible production and decay chains are considered rather than some specific ones. In both points only $\tilde{q}\tilde{q}$, $\tilde{q}\tilde{g}$ and $\tilde{g}\tilde{g}$ production are switched on. Only the squarks of the first two generations are considered and their masses are assumed to be degenerate. The only other allowed particle in the kinematic range is a massless neutralino ($m(\tilde{\chi}^0) = 0$). All other supersymmetric particles are switched

Requirement	Channel					
	A	A*	B	C	D	E
$E_{\mathrm{T}}^{\mathrm{miss}}$[GeV] >	160					
$p_{\mathrm{T}}(j_1)$ [GeV] >	130					
$p_{\mathrm{T}}(j_2)$ [GeV] >	60					
$p_{\mathrm{T}}(j_3)$ [GeV] >	–	–	60	60	60	60
$p_{\mathrm{T}}(j_4)$ [GeV] >	–	–	–	60	60	60
$p_{\mathrm{T}}(j_5)$ [GeV] >	–	–	–	–	40	40
$p_{\mathrm{T}}(j_6)$ [GeV] >	–	–	–	–	–	40
$\Delta\phi(j_i, E_{\mathrm{T}}^{\mathrm{miss}})$ >	0.4 ($i = \{1, 2, (3)\}$)			0.4 ($i = \{1, 2, 3\}$), 0.2 ($p_{\mathrm{T}} > 40$ GeV jets)		
$E_{\mathrm{T}}^{\mathrm{miss}}/m_{\mathrm{eff}}(Nj)$ >	0.3 (2j)	0.4 (2j)	0.25 (3j)	0.25 (4j)	0.2 (5j)	0.15 (6j)
m_{eff}(incl.) [GeV] >	1900/1400/–	–/1200/–	1900/–/–	1500/1200/900	1500/–/–	1400/1200/900

Table 6.2: Channels used in the analysis.

off in making their masses artificially very heavy, so the do not play a role in the spectrum. The first model point corresponds to a neutralino mass of $m(\tilde{\chi}^0) = 0\,\mathrm{TeV}$, the squark mass of the first two generations $m(\tilde{q}) = 1.0\,\mathrm{TeV}$ and the gluino mass $m(\tilde{g}) = 2.0\,\mathrm{TeV}$. The other point corresponds to the case where the squarks are heavier than the gluino with $m(\tilde{\chi}^0) = 0\,\mathrm{TeV}$, $m(\tilde{q}) = 2.0\,\mathrm{TeV}$ and $m(\tilde{g}) = 1.0\,\mathrm{TeV}$. If squarks are light relative to the gluinos the low jet multiplicity channels are more sensitive whereas when the gluino is lighter sensitivity is enhanced in the high jet multiplicity channels.
The plots in Fig. 6.1 do not show data in the regions where the hypothesis test are carried out. This depicts the stage of the analysis where the background estimation was performed blindly to protect from human bias in the statistical analysis. Full distributions with data in the SRs are showed in the results section after the hypothesis tests have been carried out.

The dominant sources of background are: W +jets, Z +jets, top pair, multi-jet, single top and diboson production. Non-collision backgrounds are found to be negligible. For each of the main background components a control region (CR) was defined with requirements as close as possible to the signal region selection, see Tab. 6.3 which is taken from Ref. [5], thus minimizing systematic uncertainties arising from extrapolation from each CR to the SR. For each selection a simultaneous normalization of backgrounds is performed, taking into account correlations in the systematic uncertainties and controlling signal contamination to the CRs.

The irreducible background Z +jets is dominated by $Z \rightarrow \nu\nu$ events with large $E_{\mathrm{T}}^{\mathrm{miss}}$Ċontrol samples requiring isolated photons and jets are used and the reconstructed momentum of the photon is added to the $\mathbf{P}_{T,miss}$ vector to estimate the $E_{\mathrm{T}}^{\mathrm{miss}}$Às cross check $Z(\rightarrow ee \setminus \mu\mu)$ + jets events are used via dileptonic control regions. The multi-jet background is caused by rare instances of poor reconstruction of jet energies in calorimeters leading to fake missing transverse momentum and as well by neutrinos in the semi-leptonic decay of heavy quarks. It is estimated using control regions in which the cut on the

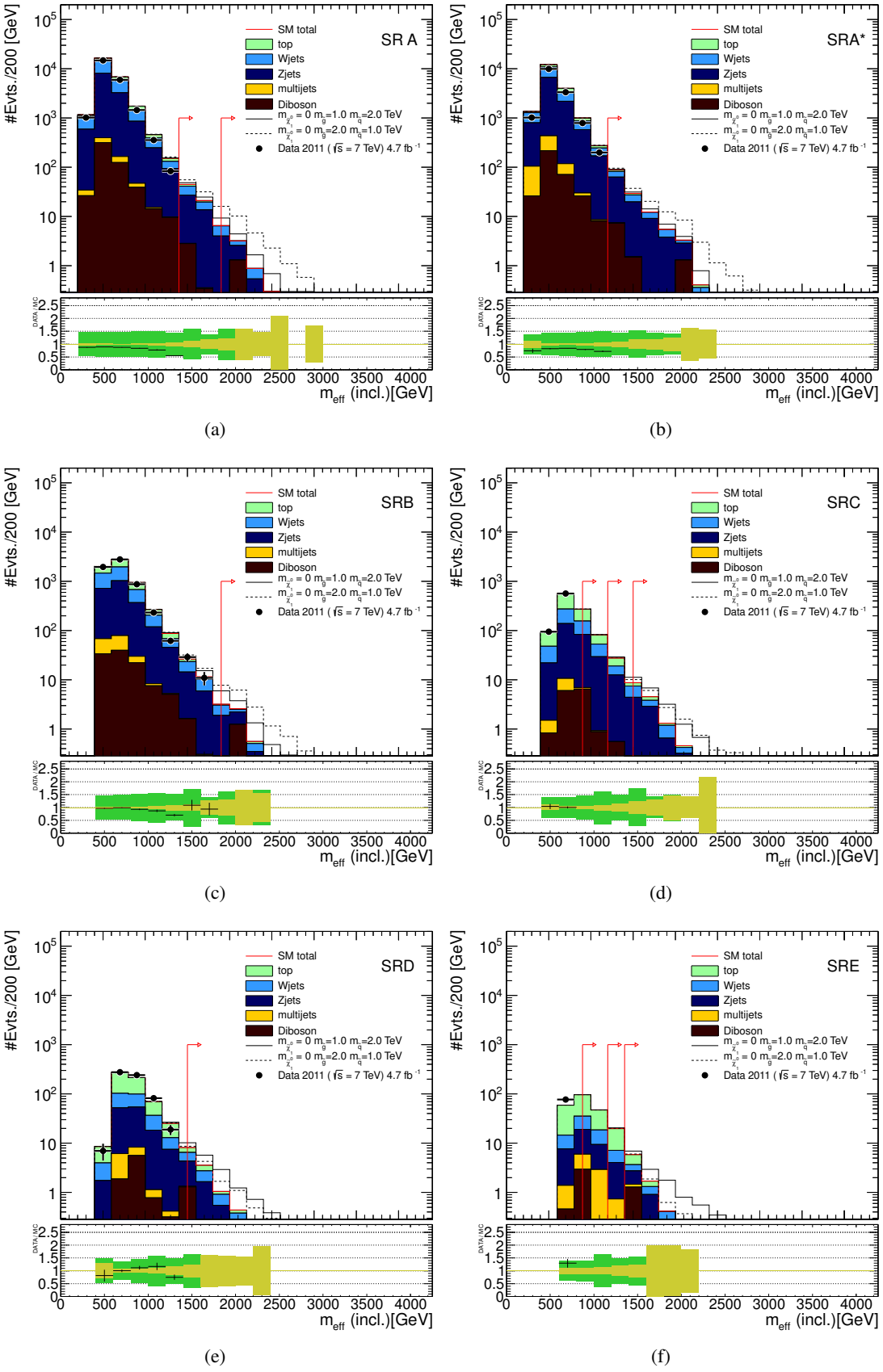

Figure 6.1: Blinded $meff$ (incl.) distributions of all search channels A-E. Each top panel shows the SM background expectations. MC simulation expectations are normalized to luminosity. The multi-jet background is estimated using the jet smearing method described in the text. Two benchmark model points with m($\tilde{\chi}^0$) =0 TeV, m($\tilde{q}$)=1.0 TeV, m($\tilde{g}$)=2.0 TeV and m($\tilde{\chi}^0$) =0 TeV, m($\tilde{q}$)=2.0 TeV, m($\tilde{g}$)=1.0 TeV, respectively. The arrows indicate the locations of the lower edges of the signal regions. The bottom panel shows the fractional deviation of the data from the total unscaled background estimate. The light (yellow) band shows the combined experimental uncertainties on the unscaled background estimates from jet energy scale, jet energy resolution, the effect of pile-up, the treatment of energy outside of reconstructed jets and MC simulation sample size. The medium (green) band includes also the total theoretical uncertainties.

CR	SR Background	CR process	CR selection
CR1a	$Z(\to \nu\nu)$+jets	γ+jets	Isolated photon
CR1b	$Z(\to \nu\nu)$+jets	$Z(\to \ell\ell)$+jets	66 GeV $< m(\ell,\ell) <$ 116 GeV
CR2	multi-jets	multi-jets	Reversed $\Delta\phi(j_i, E_{\mathrm{T}}^{\mathrm{miss}})$ cut
CR3	$W(\to \ell\nu)$+jets	$W(\to \ell\nu)$+jets	30 GeV $< m_T(\ell, E_{\mathrm{T}}^{\mathrm{miss}}) <$ 100 GeV, b-veto
CR4	$t\bar{t}$ and single-t	$t\bar{t} \to bbqq'\ell\nu$	30 GeV $< m_T(\ell, E_{\mathrm{T}}^{\mathrm{miss}}) <$ 100 GeV, b-tag

Table 6.3: Control Regions used in the analysis , indicating the main SR background targeted, the process used to model the background, and main CR cut(s) used to select this process. See Sec. 6.7 for details of event selections used.

VR	VR selection	sensitive to
VR1b	as CR1b, but $\lvert m(\ell,\ell) - m(Z)\rvert > 25GeV$	fully leptonic $t\bar{t}$
VR1c	as CR1b, 2 OSOF leptons, no req. on $\lvert m(\ell,\ell)\rvert$	fully leptonic $t\bar{t}$
VR2	as CR2,but $0.2 < \Delta\phi(j_i, E_{\mathrm{T}}^{\mathrm{miss}}) < 0.4$	multi-jets
VR5	as SR, but inverted $E_{\mathrm{T}}^{\mathrm{miss}}/m_{\mathrm{eff}}(Nj)$	multi-jets

Table 6.4: Validation Regions used in the analysis, indicating the process the selection is sensitive to , and the main VR cut(s) used.

minimum azimuthal separation between $\mathbf{P}_{T,miss}$ and jets is reversed and set to be smaller than 0.2, thus selecting events in which the $\mathbf{P}_{T,miss}$ is aligned with one of the three leading jets in the transverse plane. The W +jets background is composed of $W \to \tau\nu$ events or $W \to l\nu$ events in which no electron or muon candidate is reconstructed. It is estimated from a sample of events with a lepton, significant $E_{\mathrm{T}}^{\mathrm{miss}}$ and a transverse mass of the lepton-$E_{\mathrm{T}}^{\mathrm{miss}}$ system between 30 GeV and 100 GeV consistent with the W mass. A veto on jets from b-quark decays, using a secondary vertex requirement, is applied to split events with top decays. The lepton in the events is treated as a jet to calculate the kinematic variables.
Hadronic τ decays in $tt \to bb\tau\nu qq$ and single top events can generate large $E_{\mathrm{T}}^{\mathrm{miss}}$ and pass the jet and lepton requirements. The background from top quark events is estimated using the same procedure as that used for $W \to \nu$+jets events, but replacing the b-veto with a b-tag requirement.

The information on backgrounds via MC or data driven methods as well as the observed data in all region is fed into a likelihood for each channel. Thus the likelihood includes all information about background processes, systematic uncertainties, their correlations as well as potential signal contamination in CRs.
The transfer factor TF is defined to be

$$\begin{aligned} N_i(SR, scaled) &= TF_i * n_{CR} \\ TF_i &= N_i^{SR}/N_i^{CR} \end{aligned} \tag{6.2}$$

where

- $N(SR, scaled)$ is the number of estimated events for process i in the SR after normalization to CR
- N_i^{SR} is the number of estimated events for process i in the SR before normalization to CR
- N_i^{CR} is the number of estimated events for process i in the CR before normalization to CR
- n_{CR} is the number of observed events in the CR

'Validation' regions (VR) are defined and are summarized in Tab. 6.4. The procedure to verify the validity of the likelihood is ensured with different types of fits:

- *Background* : Only the CRs are included in the fit.
- *Extended Background*: Only the CRs and VRs are included in the fit
- *Discovery/Exclusion*: The CRs and the SR are included in the fit

In the Background and Extended Background fit setup the simultaneous normalization to the CRs and the extrapolation to the VRs is tested.. In the Discovery/Exclusion mode the SR is added. Test are carried out to detect deviation from the background expectation in data. Exclusion limits on parameters of specific supersymmetric models are set. As test statistic the profile log likelihood ratio is used. Limits on models are set choosing for each specific model the best expected channel in terms of exclusion power.

6.2 MC Simulation

Monte Carlo samples of simulated multi-jet events are generated with PYTHIA6 [74], using the MRST2007LO* modified leading-order parton distribution functions (PDFs) [84], Top quark pairs, W and Z/ γ plus jets are simulated with ALPGEN [93] and the CTEQ6L1 [83] PDF set. Herwig [94,95] is used for modelling fragmentation and hadronisation and JIMMY [96] for the underlying event.
W W , W Z, ZZ and W/ γ and the γ + *jets* processes are simulated with SHERPA [97] and single top quark production with AcerMC [98]. The spectra of SUSY signal samples are generated with Herwig++ [87, 88] or with MadGraph/PYTHIA6 [89, 90]. The SUSY signal cross section and their uncertainty are taken following as close as possible the PDF4LHC [81] recommendations as described in Ref. [82], i.e. the mean of the envelope from several PDF sets as nominal signal cross section and the uncertainty form the global envelope. In these calculations two pdf sets were used, CTEQ6L1 and MRST2007LO*. The cross sections are calculated up to next-to-leading order in α_S, including the re-summation of soft gluon emission at next-to-leading-logarithmic accuracy (NLO+NLL) [75–79].
The ATLAS collaboration optimized the generation of those processes to their needs and created software "tunes" [99–101]. Finally the simulated events are passed through the ATLAS detector simulation [102] based on GEANT4 [103].

6.3 Trigger

Triggering on the supersymmetric signals is straightforward in this analysis as the striking signal contains large $E_{\mathrm{T}}^{\mathrm{miss}}$ and multiple jets with large p_{T} . The ATLAS $E_{\mathrm{T}}^{\mathrm{miss}}$ trigger is described in Ref. [104] and the jet p_{T} trigger in Ref. [105]. A combination of both triggers is optimal for searches in final states with large $E_{\mathrm{T}}^{\mathrm{miss}}$ and multiple jets. Jets measured at the electromagnetic energy scale are required to have a p_{T} larger than 75 GeV at the first trigger stage. The amount of $E_{\mathrm{T}}^{\mathrm{miss}}$ must exceed 45 - 55 GeV at the first trigger stage depending on the instantaneous luminosity which changed during the data taking. The combination of those two triggers reach an efficiency of data taking > 98% for events with the hardest jets having more then 130 GeV of p_{T} and the total missing transverse momentum being larger than 160 GeV.

6.4 Object selection

Electrons, muons, photons, jets, b-jets and missing transverse momentum are defined in the following.

6.4.1 Jets

Jets are reconstructed using the anti-k_t jet algorithm [106] with a radius parameter of $R = 0.4$. Jets with $p_{\mathrm{T}} > 20$ GeV and $|\eta| < 2.8$ are considered. The "topological" jet algorithm [107] clusters neighboring cells and combines their information leading to a good signal to noise rate. Starting from a seed cell surrounding sells are subsequently added to the cluster until a energy threshold level for the next neighboring cell is reached. This approach suppresses potential noise quite efficiently as needed in measurements using jets and missing transverse momentum.
Jets are calibrated using the "EM+JES" scheme [108], that is jets are reconstructed at the electromagnetic scale and a correction to the jets is applied, derived from data and systematic MC studies. The correction is applied as a function of jet energy and pseudo-rapidity and covers effects from additional proton-proton interactions (pile-up), primary vertex of the event, jet energy and direction. The calibrated jet energy E_{EM+JES} is given by

$$E_{EM+JES} = (E_{EM} - O(N_{PV}, \eta, \tau_b))/F_{calib,EM+JES} \tag{6.3}$$

where E_{EM} is the energy measured at the electromagnetic scale, $O(N_{PV}, \eta, \tau_b)$ the energy from multiple proton-proton interactions , N_{PV} the number of primary vertices,τ_b the bunch spacing time and F_{calib} a correction function depending on the jet energy and pseudo-rapidity.
The term $O(N_{PV}, \eta, \tau_b)$ estimates the amount of energy from multiple interaction within one bunch crossing which depends on N_{PV}. In addition energy deposition from interaction from a nearby bunch depend on τ_b. This η dependence comes from the geometry of the calorimeters and the different particle content in η. Its magnitude is measured from minimum bias data.
$F_{calib,EM+JES}$ is calculated via MC studies where bins in un-calibrated jet energy $E_{uncalib} = E_{EM} - O(N_{PV}, \eta, \tau_b)$ and η are defined and within these bins the jet energy is corrected depending on the jet response $R_{EM} = E_{uncalib}/E_{truth}$ where E_{truth} is the jet energy from MC. The uncertainty on this calibration is in the following denoted as JES uncertainty.

B-jets are identified using a neural network algorithm, which takes as inputs variables from impact parameter measurements and from the topological structure of b-quark decays, as described in Refs. [109, 110]

6.4.2 Electrons and Muons

Electron candidates are required to have $p_{\mathrm{T}} > 20\,\mathrm{GeV}$ and $|\eta| < 2.47$, and to pass the medium selection criteria described in Ref. [111]. Cut on shower shape variables and on the amount of energy deposited in the hadronic calorimeters are applied. Additionally track requirements like the number of hits in the pixel and SCT detectors, the distance of the track to the primary vertex and the matching of the energy cluster to the track are considered.

Muon candidates [112, 113] are required to have matching tracks in the inner detector and muon spectrometer with $p_{\mathrm{T}} > 10\,\mathrm{GeV}$ and $|\eta| < 2.4$.

6.4.3 Resolving overlapping objects

Overlaps between candidate jets with $|\eta| < 2.8$ and leptons are resolved as fol- lows and are based on the $\Delta R = \sqrt{\Delta\phi^2 + \Delta\eta^2}$ variable:

- If an electron and a jet are found within $\Delta R < 0.2$, the object is interpreted as an electron and the overlapping 'jet' is ignored.
- If a muon and a jet are found within $\Delta R < 0.4$, the object is treated as a jet and the muon is ignored.
- If an electron and a jet are found within $0.2 \leq \Delta R < 0.4$, the object is interpreted as a jet and the nearby 'electron' is ignored.

6.4.4 Missing transverse momentum

The reconstruction of the missing transverse momentum vector in the x,y plane $\mathbf{P}_{T,miss}$ depends on the identification of all objects as described before and all calorimeter clusters not associated with one of these objects. All jet candidates with $|\eta| > 2.8$ are discarded. As there is no significant initial transverse momentum component in the colliding particle system the $\mathbf{P}_{T,miss}$ corresponds to the difference of the vectorial sum over all momentum vectors in the x,y plane of identified particles and unassigned clusters to the $\mathbf{0}$ vector. The magnitude of $\mathbf{P}_{T,miss}$ is $E_{\mathrm{T}}^{\mathrm{miss}}$. If an event is very unbalanced, i.e. all identified objects point into one direction a large $E_{\mathrm{T}}^{\mathrm{miss}}$ component is expected. $E_{\mathrm{T}}^{\mathrm{miss}}$ consists of several terms as follows, where $E_{\mathrm{T}}^{\mathrm{miss}}(x, y)$ being the x or the y component.

$$E_{\mathrm{T}}^{\mathrm{miss}}(x,y) = (E_{\mathrm{T}}^{\mathrm{miss}})_{\mathrm{x,y}}^{\mathrm{RefEle}} + (E_{\mathrm{T}}^{\mathrm{miss}})_{\mathrm{x,y}}^{\mathrm{RefJet}} + (E_{\mathrm{T}}^{\mathrm{miss}})_{\mathrm{x,y}}^{\mathrm{RefMuo}} + (E_{\mathrm{T}}^{\mathrm{miss}})_{\mathrm{x,y}}^{\mathrm{CellOut}}, \tag{6.4}$$

Electron objects are summed up in $(E_{\mathrm{T}}^{\mathrm{miss}})_{\mathrm{x,y}}^{\mathrm{RefEle}}$ using electrons passing 'medium' selection criteria described above with p_{T} >20 GeV before overlap removal. Jet objects are included at the jet energy scale in $(E_{\mathrm{T}}^{\mathrm{miss}})_{\mathrm{x(y)}}^{\mathrm{RefJet}}$ term using jets with p_{T} >20 GeV and over the full η range. Contributions from

muons are summed up in $(E_{\mathrm{T}}^{\mathrm{miss}})_{\mathrm{x(y)}}^{\mathrm{RefMuo}}$, using the muons with p_{T} >10 GeV) before overlap removal. $(E_{\mathrm{T}}^{\mathrm{miss}})_{\mathrm{x(y)}}^{\mathrm{CellOut}}$ is computed from energy clusters at the EM scale which are not included in reconstructed objects, in particular, clusters associated to jets with p_{T} <20 GeV are included in this term.

6.4.5 Photons

Photons are used with the 'tight' photon identification criteria from the ATLAS prompt photon cross section analysis [114].

6.5 Data

The full dataset of the proton-proton collisions provided by the LHC at a center-of-mass energy of 7 TeV in 2011 is analyzed. A total integrated luminosity of 4.7 fb^{-1} suitable for this analysis was recorded [115, 116]. The peak instantaneous luminosity ranges from 1.3×10^{30} to 3.7×10^{33} $\frac{1}{cm^2 s}$ and the peak mean number of interactions per bunch crossing from 2 to 12. The precision of the luminosity measurement is 3.9 %.

6.6 Event selection

After having defined physics objects like jets, electrons, muons as well as having resolved potential overlap, the main selection criteria targeted at distinguishing between potential supersymmetric signals and background processes are applied. As a first step a veto on electrons or muons is applied to reduce backgrounds from all final states containing one good isolated lepton and missing transverse momentum. This is mainly W's decaying leptonically accompanied with jets and $t\bar{t}$ events in the semi-leptonic decay mode. In both cases the lepton is coming from a W decaying leptonically and the missing transverse momentum from the corresponding neutrino. Electron and muons are vetoed when the p_{T} exceeds 20 GeV and 10 GeV, respectively.
The signal selections after the event cleaning and the lepton veto are listed in Tab. 6.2. The main requirements on $E_{\mathrm{T}}^{\mathrm{miss}}$ to be larger than 160 GeV and the p_{T} of the leading jet to be larger than 130 GeV ensure the analyses to be in the in a high efficiency triggering regime. The distribution of the $E_{\mathrm{T}}^{\mathrm{miss}}$ variable and the p_{T} of the hardest jet without the cut on the m_{eff} variable are shown in Fig. 6.2. Note that all distributions are derived from MC. Clearly the multi-jets backgrounds is not sufficiently described as it lacks of MC sample size. These cuts do already suppress a large amount of background, especially the QCD multi-jets background.

In both distributions it is visible that the ALPGEN MC estimates in the extreme phase-space regions with large $E_{\mathrm{T}}^{\mathrm{miss}}$ are harder than those observed in data. This is especially true for W+jets and Z+jets, but also for $t\bar{t}$ +jets generated with ALPGEN. The reasons for this can be manifold. The signal region selections cover final states from 2 to X jets. Additional requirements are applied on the transverse momenta of jets in the inclusive 2-, 3-, 4-, 5- and 6-jet events search channels A/A* , B, C, D and E, respectively.

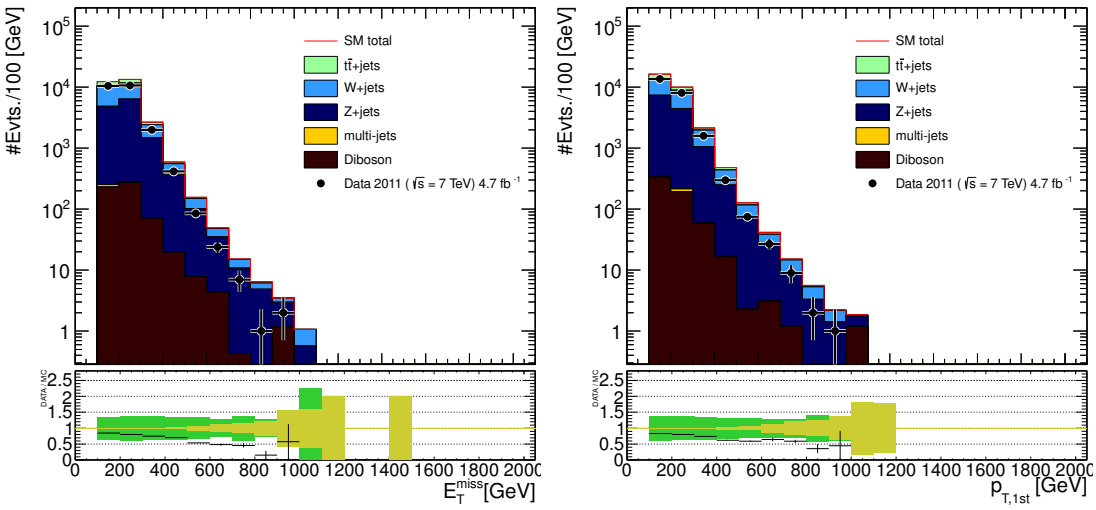

(a) (b)

Figure 6.2: Distributions of $E_{\mathrm{T}}^{\mathrm{miss}}$ and p_{T} of the hardest jet in search channel A without the m_{eff} requirement. All processes are estimated using MC normalized to the integrated luminosity. The light (yellow) band shows the combined experimental uncertainties on the unscaled background estimates from jet energy scale, jet energy resolution, the effect of pile-up, the treatment of energy outside of reconstructed jets and MC simulation sample size. The medium (green) band includes also the total theoretical uncertainties.

The jet p_{T} thresholds for the next to leading up to four jets are set at 60 GeV and those of five and six jets to 40 GeV. The jet multiplicity is plotted in Fig. 6.3. Prediction on rates of large jet multiplicity final states and especially predictions in signal regions which cover a broad range of jet multiplicities with MC generators is very difficult and challenging. The exact reason for this overshoot of ALPGEN MC over data is not known yet and needs extensive testing. However as this search is carried out in extreme phase space regions it was a priori to the search clear that we may not rely on the MC generators to describe the data. Therefore data driven and semi-data driven background estimation techniques were used which are described later on.

Further suppressing multi-jets background is the purpose of the following selection criteria, that is a requirement on $\Delta\phi(j_i, E_{\mathrm{T}}^{\mathrm{miss}})$. Mis-measurement of jet energy and emission of neutrinos from heavy flavour decay leads to missing energy in the same direction as the jet. The SR selection requires $\Delta\phi(j_i, E_{\mathrm{T}}^{\mathrm{miss}})$ of up to the first three leading jets to be larger than 0.4 for SR A*, A, and B and for C,D and E any further jet is required to have a $\Delta\phi(j_i, E_{\mathrm{T}}^{\mathrm{miss}})$ of larger than 0.2, whereas the CR serving as normalization region for the multi-jet background requires $\Delta\phi(j_i, E_{\mathrm{T}}^{\mathrm{miss}})$ to be smaller 0.2. To test the normalization in SR VR2 is defined within $0.2 < \Delta\phi(j_i, E_{\mathrm{T}}^{\mathrm{miss}}) < 0.4$. The separation of the hardest jet and $E_{\mathrm{T}}^{\mathrm{miss}}$ is shown in Fig. 6.3.

The multi-jet background is further suppressed by the $E_{\mathrm{T}}^{\mathrm{miss}}/m_{\mathrm{eff}}$ (Nj) cut. Only events with a minimum fraction of $E_{\mathrm{T}}^{\mathrm{miss}}$ relative to m_{eff} are selected. The VR5 is defined as the inverse of this requirement.

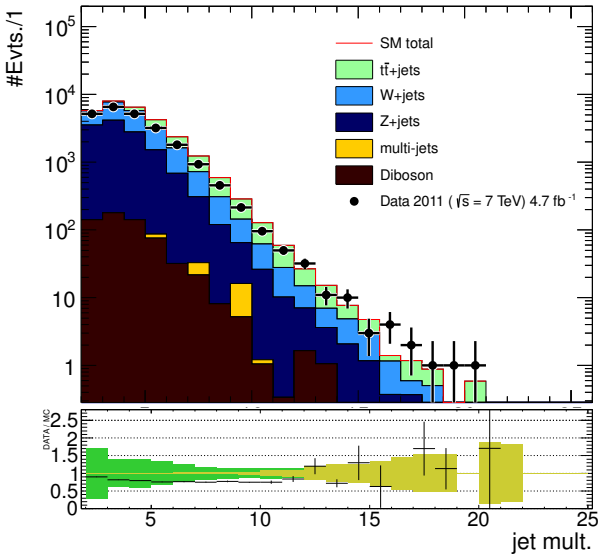

Figure 6.3: Distribution of the jet multiplicity in search channel A without the m_{eff} requirement. All processes are estimated using MC normalized to the integrated luminosity. The light (yellow) band shows the combined experimental uncertainties on the unscaled background estimates from jet energy scale, jet energy resolution, the effect of pile-up, the treatment of energy outside of reconstructed jets and MC simulation sample size. The medium (green) band includes also the total theoretical uncertainties.

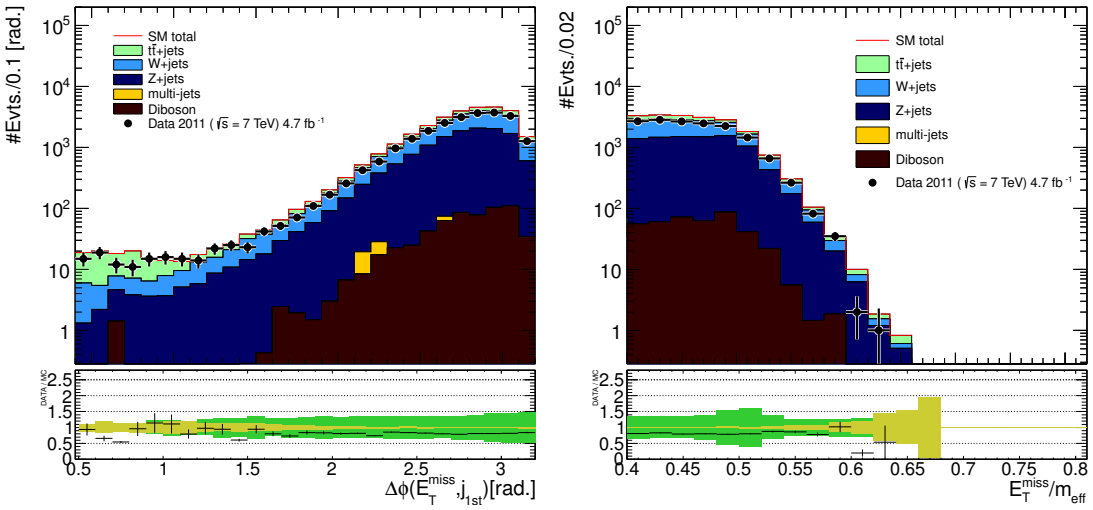

(a) (b)

Figure 6.4: Distributions of the separation of the hardest jet and $E_{\text{T}}^{\text{miss}}$ in ϕ and the ratio $E_{\text{T}}^{\text{miss}}/m_{\text{eff}}$ (Nj) in search channel A without the m_{eff} requirement. All processes are estimated using MC normalized to the integrated luminosity. The light (yellow) band shows the combined experimental uncertainties on the unscaled background estimates from jet energy scale, jet energy resolution, the effect of pile-up, the treatment of energy outside of reconstructed jets and MC simulation sample size. The medium (green) band includes also the total theoretical uncertainties.

Note that the fraction $E_{\mathrm{T}}^{\mathrm{miss}}/m_{\mathrm{eff}}$ (Nj) decreases with jet multiplicity due to the signal efficiency. If the jet multiplicity is high the channel is sensitive to multi-body SUSY decay chains. In those chains the probability to have a large momentum of the LSP is smaller than in decay chains with less intermediate states. This looser requirement on the higher multiplicity jets is also motivated by the fact that the cross section for multi-jet events decreased with multiplicity.

The SR where the hypothesis tests are carried out are defined in m_{eff} (incl.). m_{eff} (incl.) further suppresses background and is sensitive to any SUSY signal including jets and $E_{\mathrm{T}}^{\mathrm{miss}}$. Up to three m_{eff} (incl.) values are specified per channel, which are defined as tight, medium and loose, depending on the hardness of the requirement in m_{eff} (incl.).

6.7 Background Estimation

The background estimates require calculation of transfer functions and uncertainties between the control regions and signal regions. The information of the absolute level of background and the uncertainties as well as the observed data is fed into the likelihood which is constructed per signal region. Uncertainties attached to the different estimation techniques are discussed, common to all of the techniques are uncertainties from limited MC generation (MC stats.), jet energy scale calibration (JES), jet energy resolution (JER), luminosity (lumi), changing pile-up conditions (Pileup), uncertainties from MC modelling (Theory) and limited data in the CRs (CR stats.).
The main irreducible background is coming from Z +jets and is dominated by $Z \rightarrow \nu\nu$ events. The background estimation technique is described in Sec. 6.7.1 and 6.7.2. Control samples requiring isolated photons and jets are used and the reconstructed momentum of the photon is added to the $\mathbf{P}_{T,miss}$ vector to estimate the $E_{\mathrm{T}}^{\mathrm{miss}}$. As cross check $Z(\rightarrow ee(\mu\mu))$ + jets events are used via di-leptonic control regions.
The multi-jet background TF is estimated using a jet smearing method where a jet response function is defined allowing to smear low $E_{\mathrm{T}}^{\mathrm{miss}}$ jet event to higher $E_{\mathrm{T}}^{\mathrm{miss}}$ jet events. Control regions in which the cut on the minimum azimuthal separation between $\mathbf{P}_{T,miss}$ and jets is reversed and set to be smaller than 0.2. This is described in Sec. 6.7.3
The W +jets background is mainly composed of $W \rightarrow \tau\nu$ events or $W \rightarrow l\nu$ events in which no electron or muon candidate is reconstructed. It is estimated from a sample of events with a lepton, significant $E_{\mathrm{T}}^{\mathrm{miss}}$ and a transverse mass of the lepton-$E_{\mathrm{T}}^{\mathrm{miss}}$ system between 30 GeV and 100 GeV consistent with the W mass. A veto on jets from b-quark decays, using a secondary vertex requirement, is applied to split events with top decays. The lepton in the events is treated as a jet to calculate the kinematic variables.
Hadronic τ decays in $tt \rightarrow bb\tau\nu qq$ and single top events can generate large $E_{\mathrm{T}}^{\mathrm{miss}}$ and pass the jet and lepton requirements. The background from top quark events is estimated using the same procedure as that used for $W \rightarrow \nu$+jets events, but replacing the b-veto with a b-tag requirement. Both the W+jets and $t\bar{t}$ +jets estimate is described in Sec. 6.7.4

Control region/Process	Signal Region										
	SRC loose	SRE loose	SRA medium	SRAp medium	SRC medium	SRE medium	SRA tight	SRB tight	SRC tight	SRD tight	SRE tight
SR	210	148	59	85	36	25	1	1	14	9	13
CR1a / Z/γ+jets	223	77	90	170	48	26	9	5	6	3	11
CR1b / Z/γ+jets	28	0	12	25	6	0	1	1	3	2	0
CR2 / QCD jets	192	243	30	16	42	67	4	5	10	11	29
CR3 / W+jets	234	57	77	178	60	25	10	8	16	13	13
CR4 / $t\bar{t}$+ Single Top	164	87	26	63	51	35	18	17	14	13	15

Table 6.5: Observed data counts in all signal and control regions.

Control region/Process	Signal Region										
	SRC loose	SRE loose	SRA medium	SRAp medium	SRC medium	SRE medium	SRA tight	SRB tight	SRC tight	SRD tight	SRE tight
CR1a / Z/γ+jets	0.32	0.27	0.36	0.39	0.34	0.32	0.3	0.38	0.32	0.29	0.31
CR1b / Z/γ+jets	2.9	6.5	2.5	2.2	2.9	5	5.3	4.2	1.8	2.1	2.7
CR2 / multi jets	0.016	0.048	0.032	0.1	0.003	0.038	0.009	0.011	0.0034	0.02	0.04
CR3 / W+jets	0.36	0.74	0.31	0.19	0.2	0.39	0.25	0.14	0.16	0.26	0.26
CR4 / $t\bar{t}$+ Single Top	0.52	0.92	0.34	0.23	0.3	0.62	0.013	0.022	0.15	0.2	0.32

Table 6.6: Summary of initial Transfer Factors from the main control regions of each background component in every channel.

Single top is estimated via MC and normalized alongside the $t\bar{t}$ process, Wbb is present in the $t\bar{t}$ dominated CR4 and normalized alongside the W+jets process. Diboson processes are normalized to luminosity and taken from MC. Background from non-collision sources was found to negligible.
The information on backgrounds via MC or data driven methods as well as the observed data in all region is fed into a likelihood for each channel. The observed events in data in all region used in the analyses are summarized in Tab. 6.5. The information obtained by the estimation of the extrapolation from CRs top SRs via TF are shown in Tab. 6.6, which shows an overview of the central values of TFs. The calculation of those TF are described in the following sections.

The background estimates are not independent from each other, so transfer functions between control regions have to be considered as well to ensure a coherent simultaneous normalization. The transfer factors and uncertainties obtained from these techniques are fully tabulated in Appendix E, as an examples the inter-CR TF are given for the channel SR-C medium in Tab. 6.7 as well as full list of estimated uncertainties for the TF to the signal region for the same channel SR-C medium in Tab. 6.8. All uncertainties listed are parametrised as nuisance parameters in the likelihood defined in Sec. 6.9.2. A quantitative discussion of the impact of uncertainties to the analysis is given in Sec. 6.11.

6.7.1 $Z(\rightarrow \nu\nu)$+jets estimate using a γ + jets control region

The main irreducible background in this analysis is $Z(\rightarrow \nu\nu)$+jets. However a small component of $Z(\rightarrow ee/\mu\mu/\tau\tau)$+jets survives the SR selection cuts.
Two different samples are defined to control this background, that is a sample of γ+jets events (CR1a) and $Z(\rightarrow \ell\ell)$+jets sample (CR1b). The interpolation to the SR is done via MC estimates. As can be seen in Tab. 6.5, the CR1b data statistic is very poor, so the estimate of Z+jets in the SR is mainly based on the photon sample method. This is because the cross-section for photon production is considerably

Region	Main CR/Process				
	CR1a / Z/γ+jets	CR2 / multi jets	CR4 / $t\bar{t}$+ Single Top	CR3 / W+jets	CR1b / Z/γ+jets
CR1a	1	0	0	0	
CR2	0.097	1	0.37	0.2	0.85
CR4	0.0032	0	1	0.093	0.028
CR3	0.0073	0	0.36	1	0.064
CR1b		0	0.027	0	1
SR	0.34	0.003	0.3	0.2	2.9

Table 6.7: Initial cross Transfer Factors for SRC (medium).

Region	Main CR/Process				
	CR1a / Z/γ+jets	CR2 / multi jets	CR4 / $t\bar{t}$+ Single Top	CR3 / W+jets	CR1b / Z/γ+jets
Central value	0.34	0.003	0.3	0.2	2.9
JER	0.0029 0		0.022 0	−0.00042 0	1.5 0
JES	0.0094 −0.028		0.018 −0.0026	0.018 −0.01	0.82 0.68
Pileup			0 −0.0057	0 −0.009	
l resoln.			−0.0014 0.0059	−0.00091 0.00063	0 −0
Trigger			−0.0017 0.0018	−0.0011 0.0011	−0.037 0.038
b-tag/veto eff.			−0.017 0.025	−0.0032 0.0033	
acc. Z+jets/ γ	0.09 −0.09				
l scale.			−0.0016 0.0047	−0.00077 0.00021	0 −0.071
QCD smear.		0.0047 −0.0014			
MET CellOut cluster	0.00093 −0.00029		0.0012 0.00087	0.002 −0.0021	
Top Theory			0.08 −0.08		
l eff.			−0.0022 0.0023	−0.0013 0.0013	−0.043 0.044
MET CellOut pileup	$7.9e{-}05$ −0.0022		−0.0011 $-9.5e{-}05$	$-1.8e{-}05$ −0.0017	
PDF			−0.0026 0.0037	−0.0038 0.008	
Z+jets Theory					0.035 −0.035
MC stat.			0.057 −0.057	0.027 −0.027	0.66 −0.66
W+jets Theory				0.043 −0.043	

Table 6.8: Initial uncertainties of Transfer Factors to signal region for SRC (medium).

larger than that for Z production.
The magnitude of the irreducible background from $Z \to \nu\nu$ events in the SRs is estimated using a photon + jets sample. At large transverse momenta the Z and γ production cross sections mainly differ by their coupling constants with respect to quarks. The ratio of the cross section of γ+jets and $Z \to \nu\nu$+jets should therefore be constant in a large part of phase space and thus provides an good estimate for an interpolation to the SR. Furthermore a lot of systematic uncertainties e.g. MC modelling issues cancel out in this ratio.

The control sample is defined by selecting photon events. The sample is defined having exactly one isolated photon, which fulfills the 'tight' criteria as in the ATLAS prompt photon cross section analysis [114]. The photon trigger has an efficiency close to 100 % at a p_{T} of 85 GeV of the photon. The photons are required to lie within $|\eta| < 1.37$ and $1.52 \leq |\eta| < 2.37$.
The event selection criteria from Tab. 6.6 are applied. In the overlap removal of objects an additional step is included, that is any jet within $\Delta R = 0.2$ of the leading photon is removed.
The photon events are then modified to estimate the proper amount of $E_{\mathrm{T}}^{\mathrm{miss}}$in the event. The contribution from photons to the missing momentum vector $\vec{E}_{\mathrm{T}}^{\mathrm{miss}}$ is removed, thus the $E_{\mathrm{T}}^{\mathrm{miss}}$does behave as if the $E_{\mathrm{T}}^{\mathrm{miss}}$is from $Z \to \nu\nu$.

To estimate the proper amount of $Z \to \nu\nu$ + jets events in the SRs each CR1a event is scaled by factors correcting for experimental acceptance and efficiencies for the photons according to

$$N^{Z_{\nu\nu}}\left(p_T^V, m_{\mathrm{eff}}(incl.)\right) = N^{\gamma}\left(p_T^V, m_{\mathrm{eff}}(incl.)\right) \cdot \left[\frac{1}{\varepsilon^{\gamma}(p_T^V) \cdot A^{\gamma}(p_T^V)} \cdot R_{Z/\gamma}(p_T^V) \cdot Br(Z \to \nu\nu)\right], \tag{6.5}$$

with $\varepsilon^{\gamma} \cdot A^{\gamma}$ being the reconstruction efficiency and detector acceptance for reconstructed photons and are corrected for effects that are not present for Z boson background events in the SR. These effect are estimated from ratio between the MC γ p_{T} distributions in the CRs with and without including the photon event selection step. The combined reconstruction efficiency and detector acceptance is 86%, with an uncertainty of less than 1% and decreases with increasing photon p_{T} . A further uncertainty of 5% is included to account for differences in efficiency of the photon isolation criteria in different event samples. Backgrounds of multi-jets and W decays where a lepton is misidentified as photon are found to be < 1% and thus are neglected, however a 5% uncertainty is assigned to the number of events.
$R_{Z/\gamma}(p_T^V) \cdot Br(Z \to \nu\nu)$ is the cross-section ratio for $Z \to \nu\nu$ production over γ production taken from `ALPGEN` MC. A conservative estimate of the uncertainty on the cross section ratio is made of 25%. Studies showed that the ratio is not completely independent from phase space consideration, i.e. different jet multiplicities. Thus studies have been carried out with PYTHIA8 [117] and GAMBOS/VECBOS [118]. The uncertainties are combined into one nuisance parameter and referred to as "acc. Z+jets/ γ" further in the text. JES, JER and the impact of changing pile-up conditions on $E_{\mathrm{T}}^{\mathrm{miss}}$(MET CellOut pileup and MET CellOut cluster) are modelled as nuisance parameters as well.
The full Z+jet estimation in the SR is then obtained by multiplying the amount of estimated $Z_{\nu\nu}$ + jets

event by the ratio of $Z(\rightarrow \nu\nu/ee/\mu\mu/\tau\tau)$+jets to $Z_{\nu\nu}$+jets events for each SR. This correction factor c_Z is tabulated in Tab. 6.9.

Signal Region	c_Z
SRA medium	1.01 ± 0.07
SRA tight	1 ± 0.2
SRAp medium	1.07 ± 0.07
SRB tight	1 ± 0.3
SRC loose	1.11 ± 0.05
SRC medium	1.1 ± 0.1
SRC tight	1 ± 0.2
SRD tight	1 ± 0.2
SRE loose	1.03 ± 0.09
SRE medium	1.09 ± 0.19
SRE tight	1 ± 0.2

Table 6.9: Ratio c_Z of $Z + jets$ to $Z \rightarrow \nu\nu + jets$ in the SR obtained by MC. The shown uncertainties are those from limited MC statistics.

Process	Generator	Dataset ID	Cross-section [pb]	k-factor	Efficiency
$Z \to ee\ (NP0)$	ALPGEN	107650	6.7e+02	1.2	1
$Z \to ee\ (NP1)$	ALPGEN	107651	1.3e+02	1.2	1
$Z \to ee\ (NP2)$	ALPGEN	107652	41	1.2	1
$Z \to ee\ (NP3)$	ALPGEN	107653	11	1.2	1
$Z \to ee\ (NP4)$	ALPGEN	107654	2.9	1.2	1
$Z \to ee\ (NP5)$	ALPGEN	107655	0.83	1.2	1
$Z \to eebb\ (NP0)$	ALPGEN	109300	6.6	1.2	1
$Z \to eebb\ (NP1)$	ALPGEN	109301	2.5	1.2	1
$Z \to eebb\ (NP2)$	ALPGEN	109302	0.89	1.2	1
$Z \to eebb\ (NP3)$	ALPGEN	109303	0.39	1.2	1

Table 6.10: $Z \to ee$ + *jets* MC samples used in this thesis. Listed are the process, the generator, a ID for bookkeeping, the cross-section, the k-factor and the efficiency.

Process	Generator	Dataset ID	Cross-section [pb]	k-factor	Efficiency
$Z \to \mu\mu\ (NP0)$	ALPGEN	107660	6.7e+02	1.2	1
$Z \to \mu\mu\ (NP1)$	ALPGEN	107661	1.3e+02	1.2	1
$Z \to \mu\mu\ (NP2)$	ALPGEN	107662	40	1.2	1
$Z \to \mu\mu\ (NP3)$	ALPGEN	107663	11	1.2	1
$Z \to \mu\mu\ (NP4)$	ALPGEN	107664	2.8	1.2	1
$Z \to \mu\mu\ (NP5)$	ALPGEN	107665	0.77	1.2	1
$Z \to \mu\mu bb\ (NP0)$	ALPGEN	109305	6.6	1.2	1
$Z \to \mu\mu bb\ (NP1)$	ALPGEN	109306	2.5	1.2	1
$Z \to \mu\mu bb\ (NP2)$	ALPGEN	109307	0.89	1.2	1
$Z \to \mu\mu bb\ (NP3)$	ALPGEN	109308	0.39	1.2	1

Table 6.11: $Z \to \mu\mu$ + *jets* MC samples used in this thesis. Listed are the process, the generator, a ID for bookkeeping, the cross-section, the k-factor and the efficiency.

6.7.2 Z+jets estimate using a $Z(\to \ell\ell)$ + jets control region

An alternative approach to estimate the Z +jets contribution to the SR is via the control region CR1b containing two opposite sign electrons or muons with a p_{T} larger than 25 and 20 GeV for electrons and larger than 20 and 20 GeV for muons, respectively. The leading lepton is required to have a p_{T} larger than 25 GeV to be in the plateau of the trigger. To select events from Z decays the invariant mass of the di-lepton invariant mass is required to lie in $66\,GeV < m(ll) < 116\,GeV$. The vector of the reconstructed Z is added to the measured $\vec{E}_{\mathrm{T}}^{\mathrm{miss}}$ to estimate the $E_{\mathrm{T}}^{\mathrm{miss}}$ amount properly. The selection criteria are relaxed with respect to the SR selections as the data statistics turned out to be too poor. That is the requirement on $\Delta\phi(j_i, E_{\mathrm{T}}^{\mathrm{miss}})$ and $E_{\mathrm{T}}^{\mathrm{miss}}/m_{\mathrm{eff}}$ are ignored. This introduced an additional uncertainty in the extrapolation from the CR to the SR. The MC samples of the the processes $Z \to ee$ + *jets*, $Z \to \mu\mu$ + *jets* and $Z \to \tau\tau$ + *jets* used are listed in Tabs. 6.10, 6.11 and 6.12, respectively. The MC samples used to estimate the $Z \to \nu\nu$ + *jets* processes are listed in Tab. 6.13. The k-factors are used to normalize the generated event samples to NNLO precision and are derived from Ref. [119]. The m_{eff} distributions of this selection are shown in Fig. 6.5. The ALPGEN Z-estimate is plotted in blue. The selection is

Process	Generator	Dataset ID	Cross-section [pb]	k-factor	Efficiency
$Z \to \tau\tau$ $(NP0)$	ALPGEN	107670	6.7e+02	1.2	1
$Z \to \tau\tau$ $(NP1)$	ALPGEN	107671	1.3e+02	1.2	1
$Z \to \tau\tau$ $(NP2)$	ALPGEN	107672	40	1.2	1
$Z \to \tau\tau$ $(NP3)$	ALPGEN	107673	11	1.2	1
$Z \to \tau\tau$ $(NP4)$	ALPGEN	107674	2.8	1.2	1
$Z \to \tau\tau$ $(NP5)$	ALPGEN	107675	0.77	1.2	1
$Z \to \tau\tau bb$ $(NP0)$	ALPGEN	109310	6.6	1.2	1
$Z \to \tau\tau bb$ $(NP1)$	ALPGEN	109311	2.5	1.2	1
$Z \to \tau\tau bb$ $(NP2)$	ALPGEN	109312	0.89	1.2	1
$Z \to \tau\tau bb$ $(NP3)$	ALPGEN	109313	0.39	1.2	1

Table 6.12: $Z \to \tau\tau$ + *jets* MC samples used in this thesis. Listed are the process, the generator, a ID for bookkeeping, the cross-section, the k-factor and the efficiency.

Process	Generator	Dataset ID	Cross-section [pb]	k-factor	Efficiency
$Z \to \nu\nu$ $(NP0)$	ALPGEN	107710	3.6e+03	1.3	0.0075
$Z \to \nu\nu$ $(NP1)$	ALPGEN	107711	7.4e+02	1.3	0.61
$Z \to \nu\nu$ $(NP2)$	ALPGEN	107712	2.2e+02	1.3	0.88
$Z \to \nu\nu$ $(NP3)$	ALPGEN	107713	62	1.3	0.97
$Z \to \nu\nu$ $(NP4)$	ALPGEN	107714	16	1.3	0.99
$Z \to \nu\nu$ $(NP1)$ $p_{\mathrm{T}} > 20$	ALPGEN	144192	37	1.3	0.35
$Z \to \nu\nu$ $(NP2)$ $p_{\mathrm{T}} > 20$	ALPGEN	144193	34	1.3	0.3
$Z \to \nu\nu$ $(NP3)$ $p_{\mathrm{T}} > 20$	ALPGEN	144194	16	1.3	0.34
$Z \to \nu\nu$ $(NP4)$ $p_{\mathrm{T}} > 20$	ALPGEN	144195	5.5	1.3	0.4
$Z \to \nu\nu$ $(NP5)$ $p_{\mathrm{T}} > 20$	ALPGEN	144017	3.6	1.3	1
$Z \to \nu\nu$ $(NP6)$ $p_{\mathrm{T}} > 20$	ALPGEN	144021	0.92	1.3	1
$Z \to \nu\nu bb$ $(NP0)$ $p_{\mathrm{T}} > 20$	ALPGEN	118962	33	1.3	1
$Z \to \nu\nu bb$ $(NP1)$ $p_{\mathrm{T}} > 20$	ALPGEN	118963	14	1.3	1
$Z \to \nu\nu bb$ $(NP2)$ $p_{\mathrm{T}} > 20$	ALPGEN	118964	5.2	1.3	1
$Z \to \nu\nu bb$ $(NP3)$ $p_{\mathrm{T}} > 20$	ALPGEN	118965	1.6	1.3	1

Table 6.13: $Z \to \nu\nu$ + *jets* MC samples used in this thesis. Listed are the process, the generator, a ID for bookkeeping, the cross-section, the k-factor and the efficiency.

quite clean, only a very small fraction of diboson events in the low jet multiplicity channels and $t\bar{t}$ events in the high jet multiplicity channels are visible. However even with relaxed criteria the data statistics stays poor for the tight channels and even in the high jet multiplicity channel for SR-E loose.

The TF are defined as

$$TF = \frac{N(Z(\rightarrow \nu\nu/ee/\mu\mu/\tau\tau) + jets)_{MC,SR}}{N(Z(\rightarrow \nu\nu/ee/\mu\mu/\tau\tau) + jets)_{MC,CR}} \tag{6.6}$$

with $N(Z(\rightarrow \nu\nu/ee/\mu\mu/\tau\tau) + jets)_{MC,SR}$ being the amount of Z+jets event estimated from ALPGEN MC in the SR and $N(Z(\rightarrow \nu\nu/ee/\mu\mu/\tau\tau) + jets)_{MC,SR}$ the amount of Z+jets event estimated from ALPGEN MC in the CR.

Additional uncertainties to the common ones on the TF come from limited number of generated MC events, the electron and muon energy resolutions, the electron and muon selection efficiencies, the electron trigger efficiency and the electron energy scale calibration.

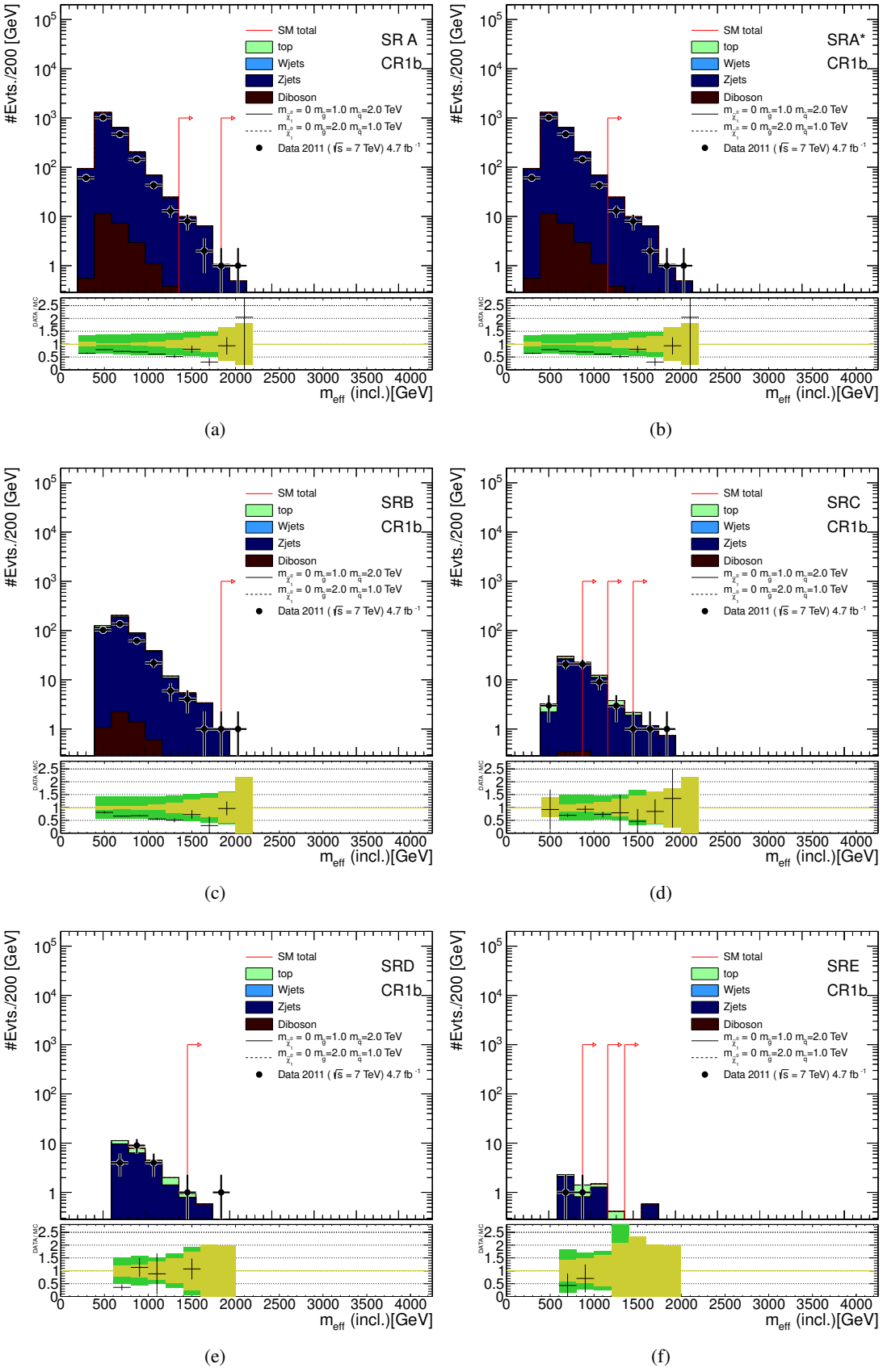

Figure 6.5: *meff* (incl.) distributions of all search channels A-E in CR1b. Each top panel shows the SM background expectations. MC simulation expectations are normalized to luminosity. The multi-jet background is estimated using the jet smearing method described in the text. Two benchmark model points with m($\tilde{\chi}^0$) =0 TeV, m($\tilde{q}$)=1.0 TeV, m($\tilde{g}$)=2.0 TeV and m($\tilde{\chi}^0$) =0 TeV, m($\tilde{q}$)=2.0 TeV, m($\tilde{g}$)=1.0 TeV, respectively. The arrows indicate the locations of the lower edges of the signal regions. The bottom panel shows the fractional deviation of the data from the total unscaled background estimate. The light (yellow) band shows the combined experimental uncertainties on the unscaled background estimates from jet energy scale, jet energy resolution, the effect of pile-up, the treatment of energy outside of reconstructed jets and MC simulation sample size. The medium (green) band includes also the total theoretical uncertainties.

Process	Generator	Dataset ID	Cross-section [pb]	k-factor	Efficiency
Di-jet ($2 \to 2$) J0	PYTHIA	105009	9.9e+09	1	1
Di-jet ($2 \to 2$) J1	PYTHIA	105010	6.8e+08	1	1
Di-jet ($2 \to 2$) J2	PYTHIA	105011	4.1e+07	1	1
Di-jet ($2 \to 2$) J3	PYTHIA	105012	2.2e+06	1	1
Di-jet ($2 \to 2$) J4	PYTHIA	105013	8.8e+04	1	1
Di-jet ($2 \to 2$) J5	PYTHIA	105014	2.4e+03	1	1
Di-jet ($2 \to 2$) J6	PYTHIA	105015	34	1	1
Di-jet ($2 \to 2$) J7	PYTHIA	105016	0.14	1	1
Di-jet ($2 \to 2$) J8	PYTHIA	105017	6e-06	1	1

Table 6.14: multi-jets MC samples used in this thesis. Listed are the process, the generator, a ID for bookkeeping, the cross-section, the k-factor and the efficiency.

6.7.3 QCD multi-jets

As discussed before the analysis is designed to reject multi-jet event by criteria on $E_{\mathrm{T}}^{\mathrm{miss}}$, $\Delta\phi(j_i, E_{\mathrm{T}}^{\mathrm{miss}})$, and p_{T} of jets, the expected amount of background in the SR of this kind is very small. Nevertheless it is important to estimate its contribution properly, as any observed excess must be clearly distinguished from this process. High cross section and a low acceptance makes it impossible to estimate via MC estimation, thus a data driven approach was followed. A detailed description of the method is given in Ref. [5]. A sample multi jets data at low $E_{\mathrm{T}}^{\mathrm{miss}}$ with large statistics is considered. A response function for jets is defined to model the response of the calorimeters, which is "tuned" by MC and additional data samples. The MC samples used are listed in Tab. 6.14. Pythia as a parton shower MC program describes parton radiation as successive parton emissions. The generation of these successive parton emission is splitted into the number X of additional partons emitted and labelled with JX in the table. These MC samples are not adequate to estimate the multi-jets background process in the phase space region of large m_{eff} , but are used for studies at low $E_{\mathrm{T}}^{\mathrm{miss}}$.
The effects of jet mis-measurement $E_{\mathrm{T}}^{\mathrm{miss}}$ from neutrinos and muons in heavy flavor decays are modelled with MC into the response function. Any other effects, also from MC modelling are tried to be compensated by two dedicated sideband measurements. Events with large $E_{\mathrm{T}}^{\mathrm{miss}}$ are generated using this response function and the low $E_{\mathrm{T}}^{\mathrm{miss}}$ jet events . These events can be used to determine the m_{eff} and $\Delta\phi(j_i, E_{\mathrm{T}}^{\mathrm{miss}})$ distribution to calculate the TF between the control region for the multi jet process and the signal region. That is the TF from low $\Delta\phi(j_i, E_{\mathrm{T}}^{\mathrm{miss}})$ events to higher $\Delta\phi(j_i, E_{\mathrm{T}}^{\mathrm{miss}})$ events. The TF obtained by this method are summarized in table 6.7. The combined uncertainty on the TF including those from interpolation effect, modelling of the response function, JES, JER and limited MC statistics is summarized in 'QCD smear.' e.g. in Tab. 6.8. The m_{eff} distribution in CR2 are shown in Fig. 6.6. An alternative approach was followed in Ref. [120] leading to similar results.

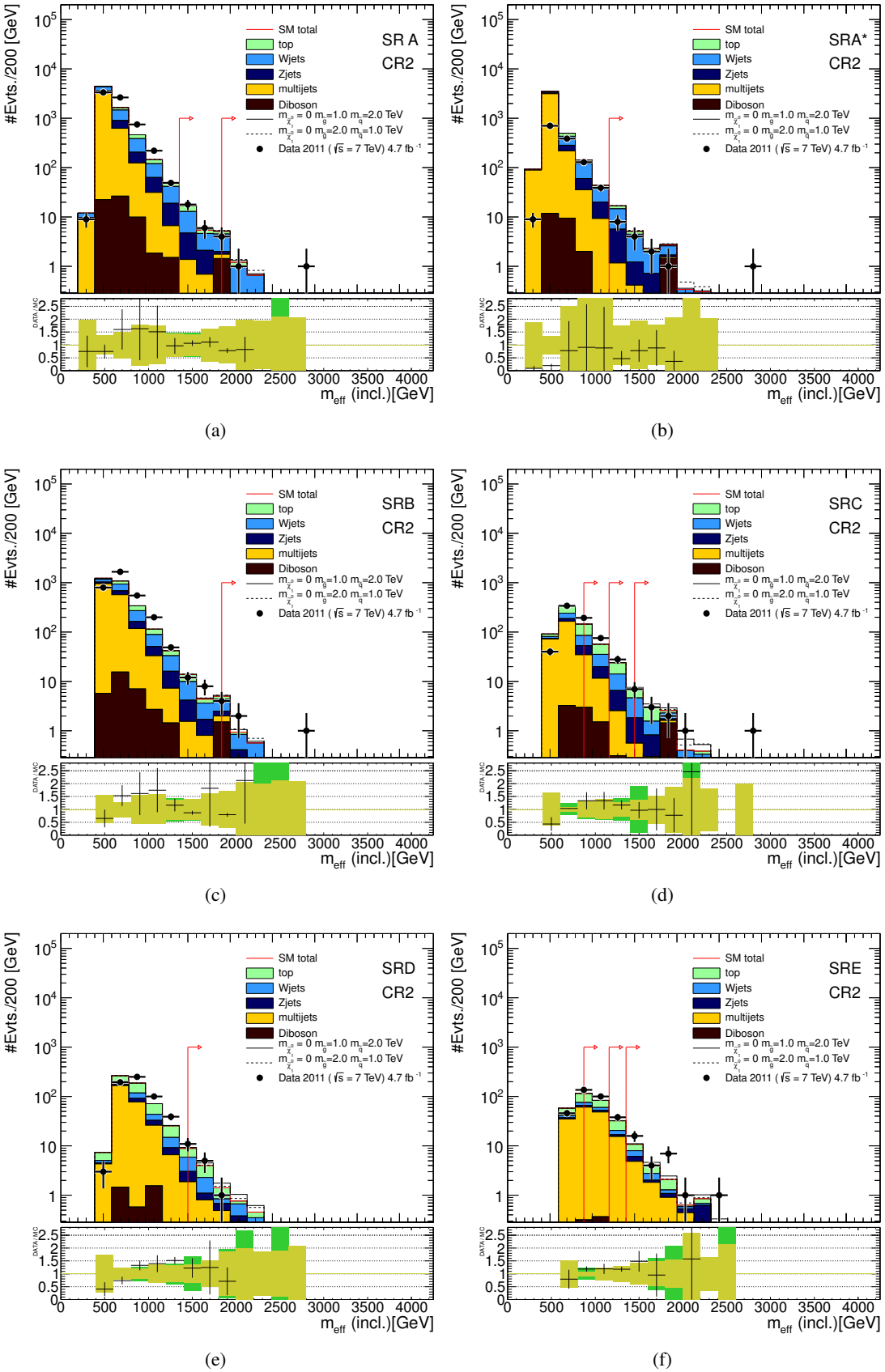

Figure 6.6: *meff* (incl.) distributions of all search channels A-E in CR2. Each top panel shows the SM background expectations. MC simulation expectations are normalized to luminosity. The multi-jet background is estimated using the jet smearing method described in the text. Two benchmark model points with m($\tilde{\chi}^0$) =0 TeV, m($\tilde{q}$)=1.0 TeV, m($\tilde{g}$)=2.0 TeV and m($\tilde{\chi}^0$) =0 TeV, m($\tilde{q}$)=2.0 TeV, m($\tilde{g}$)=1.0 TeV, respectively. The arrows indicate the locations of the lower edges of the signal regions. The bottom panel shows the fractional deviation of the data from the total unscaled background estimate. The light (yellow) band shows the combined experimental uncertainties on the unscaled background estimates from jet energy scale, jet energy resolution, the effect of pile-up, the treatment of energy outside of reconstructed jets and MC simulation sample size. The medium (green) band includes also the total theoretical uncertainties.

6.7.4 W+jets and $t\bar{t}$

The W+jets and $t\bar{t}$ and single top background is estimated via the control regions CR3 and CR4 and MC based TFs. The dominant source of background from $t\bar{t}$ + jets or W +jets are decays which are leptonically, but the lepton is out of acceptance, not reconstructed or a hadronically decaying τ is involved. Thus the control regions require exactly one isolated electron or muon. The transverse mass M_T of the lepton and $\mathbf{P}_{T,miss}$ system is required to lie within 30 GeV and 100 GeV. The lepton is then transformed into a jet and further counted as an additional jet, as if e.g. an electron is reconstructed as a jet. If a muon is not reconstructed it usually contributes to the $E_{\mathrm{T}}^{\mathrm{miss}}$İn τ decays jets from the hadrons and $E_{\mathrm{T}}^{\mathrm{miss}}$from the neutrino can occur. The choice of treating all leptons as jets is due to the fact that the main component of this background consists of hadronically decaying τ and that this ways a large statistics sample could be constructed from the electron and muon channel. CR3 targeted at W+jets requires a b-jet veto and CR4 targeted at $t\bar{t}$ +jets requires at least one b-tagged jet. Via this requirement the number of events populating both regions are to some extend anti-correlated, as e.g. an uncertainty on the b-tagging efficiency could swap events from one region into another. The $\Delta\phi(j_i, E_{\mathrm{T}}^{\mathrm{miss}})$ and $E_{\mathrm{T}}^{\mathrm{miss}}/m_{\mathrm{eff}}$ (Nj) requirements are not applied to increase statistics of the data samples.
The MC samples used for $t\bar{t}$ and single top are listed in Tab. 6.15. The cross sections and k-factors were calculated for a top quark mass of 172.5 GeV/c^2 and obtained from approximate NNLO QCD calculations [121].The samples used for $W \rightarrow e\nu + jets$, $W \rightarrow \mu\nu + jets$ and $W \rightarrow \tau\nu + jets$ background estimation are listed in Tab. 6.16, 6.17 and 6.18, respectively. The k-factors are used to normalize the generated event samples to NNLO precision and are derived from Ref. [119].

As this samples require lepton and b-jet criteria, several weights are applied to the MC samples involved. The efficiency of an electron or an muon being identified is different in data and MC. This efficiency is corrected for in the CR and the corresponding inefficiency corrected for in the SR as function of η and the lepton p_{T} . The lepton resolution differs as well between data and MC and is therefore adjusted in the MC. The b-tag efficiency is as well different in data and MC [109, 109], thus it must be corrected for in CR4 and the inefficiency in CR3 , respectively (but not in the SR).
The TFs were calculated between CR and SR as well as between CRs as shown in e.g. for SRC medium in Tab. 6.7. Uncertainties specific to these regions modelled as nuisance parameters as listed in e.g. for SRC medium in Tab. 6.8. These are terms from the lepton resolution (l resoln.), the lepton energy scale (l scale.), the b-tag efficiency (b-tag/veto eff.) and the uncertainties associated with the MC modelling of the W+jets (W+jets Theory) and $t\bar{t}$ +jets (Top Theory). The theoretical uncertainties include variations of hadronisation and factorization scales and effects of extra radiation of jets.
Fig. 6.7 and Fig. 6.8 show the m_{eff} distributions in CR3 and CR4. The ALPGEN MC estimate of W+jets is plotted in light blue, the $t\bar{t}$ component in green. In CR3 W+jets is dominant in CR4 $t\bar{t}$ +jets is dominant, but there is non-negligible contamination of $t\bar{t}$ in CR3 and W+jets in CR4. Thus a simultaneous normalization is needed.

Process	Generator	Dataset ID	Cross-section [pb]	k-factor	Efficiency
$t\bar{t} \to lvlv\ (NP0)$	ALPGEN	105890	3.5	1.7	1
$t\bar{t} \to lvlv\ (NP1)$	ALPGEN	105891	3.4	1.7	1
$t\bar{t} \to lvlv\ (NP2)$	ALPGEN	105892	2.1	1.7	1
$t\bar{t} \to lvlv\ (NP3)$	ALPGEN	117897	0.95	1.7	1
$t\bar{t} \to lvlv\ (NP4)$	ALPGEN	117898	0.33	1.7	1
$t\bar{t} \to lvlv\ (NP5)$	ALPGEN	117899	0.13	1.7	1
$t\bar{t} \to lvqq\ (NP0)$	ALPGEN	105894	14	1.8	1
$t\bar{t} \to lvqq\ (NP1)$	ALPGEN	105895	14	1.8	1
$t\bar{t} \to lvqq\ (NP2)$	ALPGEN	105896	8.4	1.8	1
$t\bar{t} \to lvqq\ (NP3)$	ALPGEN	117887	3.8	1.8	1
$t\bar{t} \to lvqq\ (NP4)$	ALPGEN	117888	1.3	1.8	1
$t\bar{t} \to lvqq\ (NP5)$	ALPGEN	117889	0.5	1.8	1
$t \to ev\ (t-chan.)$	AcerMC	117360	7	1	1
$t \to \mu v\ (t-chan.)$	AcerMC	117361	7	1	1
$t \to \tau v\ (t-chan.)$	AcerMC	117362	7	1	1
$t \to ev\ (s-chan.)$	AcerMC	117363	0.5	1	1
$t \to \mu v\ (s-chan.)$	AcerMC	117364	0.5	1	1
$t \to \tau v\ (s-chan.)$	AcerMC	117365	0.5	1	1
$Wt-chan.$	AcerMC	105500	16	1	1

Table 6.15: $t\bar{t}$ and single top MC samples used in this thesis. Listed are the process, the generator, a ID for bookkeeping, the cross-section, the k-factor and the efficiency.

Process	Generator	Dataset ID	Cross-section [pb]	k-factor	Efficiency
$W \to ev\ (NP0)$	ALPGEN	107680	6.9e+03	1.2	1
$W \to ev\ (NP1)$	ALPGEN	107681	1.3e+03	1.2	1
$W \to ev\ (NP2)$	ALPGEN	107682	3.8e+02	1.2	1
$W \to ev\ (NP3)$	ALPGEN	107683	1e+02	1.2	1
$W \to ev\ (NP4)$	ALPGEN	107684	26	1.2	1
$W \to ev\ (NP1)\ p_{\mathrm{T}} > 20$	ALPGEN	144196	1.3e+03	1.2	0.0057
$W \to ev\ (NP2)\ p_{\mathrm{T}} > 20$	ALPGEN	144197	3.8e+02	1.2	0.017
$W \to ev\ (NP3)\ p_{\mathrm{T}} > 20$	ALPGEN	144198	1e+02	1.2	0.034
$W \to ev\ (NP4)\ p_{\mathrm{T}} > 20$	ALPGEN	144199	26	1.2	0.056
$W \to ev\ (NP5)\ p_{\mathrm{T}} > 20$	ALPGEN	144018	5.8	1.2	1
$W \to ev\ (NP6)\ p_{\mathrm{T}} > 20$	ALPGEN	144022	1.5	1.2	1

Table 6.16: $W \to ev$ + *jets* MC samples used in this thesis. Listed are the process, the generator, a ID for bookkeeping, the cross-section, the k-factor and the efficiency.

Process	Generator	Dataset ID	Cross-section [pb]	k-factor	Efficiency
$W \to \mu\nu\,(NP0)$	ALPGEN	107690	6.9e+03	1.2	1
$W \to \mu\nu\,(NP1)$	ALPGEN	107691	1.3e+03	1.2	1
$W \to \mu\nu\,(NP2)$	ALPGEN	107692	3.8e+02	1.2	1
$W \to \mu\nu\,(NP3)$	ALPGEN	107693	1e+02	1.2	1
$W \to \mu\nu\,(NP4)$	ALPGEN	107694	26	1.2	1
$W \to \mu\nu\,(NP1)\ p_{\mathrm{T}} > 20$	ALPGEN	144200	1.3e+03	1.2	0.0054
$W \to \mu\nu\,(NP2)\ p_{\mathrm{T}} > 20$	ALPGEN	144201	3.8e+02	1.2	0.016
$W \to \mu\nu\,(NP3)\ p_{\mathrm{T}} > 20$	ALPGEN	144202	1e+02	1.2	0.034
$W \to \mu\nu\,(NP4)\ p_{\mathrm{T}} > 20$	ALPGEN	144203	26	1.2	0.056
$W \to \mu\nu\,(NP5)\ p_{\mathrm{T}} > 20$	ALPGEN	144019	5.8	1.2	1
$W \to \mu\nu\,(NP6)\ p_{\mathrm{T}} > 20$	ALPGEN	144023	1.5	1.2	1

Table 6.17: $W \to \mu\nu$ + *jets* MC samples used in this thesis. Listed are the process, the generator, a ID for bookkeeping, the cross-section, the k-factor and the efficiency.

Process	Generator	Dataset ID	Cross-section [pb]	k-factor	Efficiency
$W \to \tau\nu\,(NP0)$	ALPGEN	107700	6.9e+03	1.2	1
$W \to \tau\nu\,(NP1)$	ALPGEN	107701	1.3e+03	1.2	1
$W \to \tau\nu\,(NP2)$	ALPGEN	107702	3.8e+02	1.2	1
$W \to \tau\nu\,(NP3)$	ALPGEN	107703	1e+02	1.2	1
$W \to \tau\nu\,(NP4)$	ALPGEN	107704	26	1.2	1
$W \to \tau\nu\,(NP1)\ p_{\mathrm{T}} > 20$	ALPGEN	144204	1.3e+03	1.2	0.0084
$W \to \tau\nu\,(NP2)\ p_{\mathrm{T}} > 20$	ALPGEN	144205	3.8e+02	1.2	0.024
$W \to \tau\nu\,(NP3)\ p_{\mathrm{T}} > 20$	ALPGEN	144206	1e+02	1.2	0.05
$W \to \tau\nu\,(NP4)\ p_{\mathrm{T}} > 20$	ALPGEN	144207	26	1.2	0.082
$W \to \tau\nu\,(NP5)\ p_{\mathrm{T}} > 20$	ALPGEN	144020	5.8	1.2	1
$W \to \tau\nu\,(NP6)\ p_{\mathrm{T}} > 20$	ALPGEN	144024	1.5	1.2	1

Table 6.18: $W \to \tau\nu$ + *jets* MC samples used in this thesis. Listed are the process, the generator, a ID for bookkeeping, the cross-section, the k-factor and the efficiency.

Process	Generator	Dataset ID	Cross-section [pb]	k-factor	Efficiency
$Z \to \mu\mu qqqq$	SHERPA	125951	0.45	1.5	1
$Z \to ttqqqq$	SHERPA	125952	0.44	1.5	1
$Z \to eeqqqq$	SHERPA	125956	0.48	1.5	1
$Z \to \mu\mu qqqq$	SHERPA	125957	0.48	1.5	1
$Z \to ttqqqq$	SHERPA	125958	0.47	1.5	1
$WW \to lvlv$	SHERPA	128810	3	1.5	1
$WZ \to lllv$	SHERPA	128811	0.36	1.5	1
$WZ \to lllv$	SHERPA	128812	1	1.5	1
$ZZ \to llll$	SHERPA	128813	0.27	1.5	1
$ZZ \to llvv$	SHERPA	128814	0.24	1.5	1
$ZZ \to llvv$	SHERPA	128814	0.24	1.5	1
$WZ \to lvvv$	SHERPA	143062	0.72	1.5	1
$WZ \to qqvv$	SHERPA	143063	1.4	1.5	1
$W \to lvqqq$	SHERPA	143064	25	1.5	1
$Z \to vvqqq$	SHERPA	143065	1.3	1.5	1

Table 6.19: Di-boson MC samples used in this thesis. Listed are the process, the generator, a ID for bookkeeping, the cross-section, the k-factor and the efficiency.

6.7.5 Diboson

Diboson processes are taken from the SHERPA MC generator at LO. The separate components are listed in Tab. 6.19. The k-factors are used to normalize the generated event samples to NLO precision and are derived from Ref. [119]. A conservative 50% uncertainty on the number of events is applied to this background and further referred to as 'Generic Diboson' uncertainty.

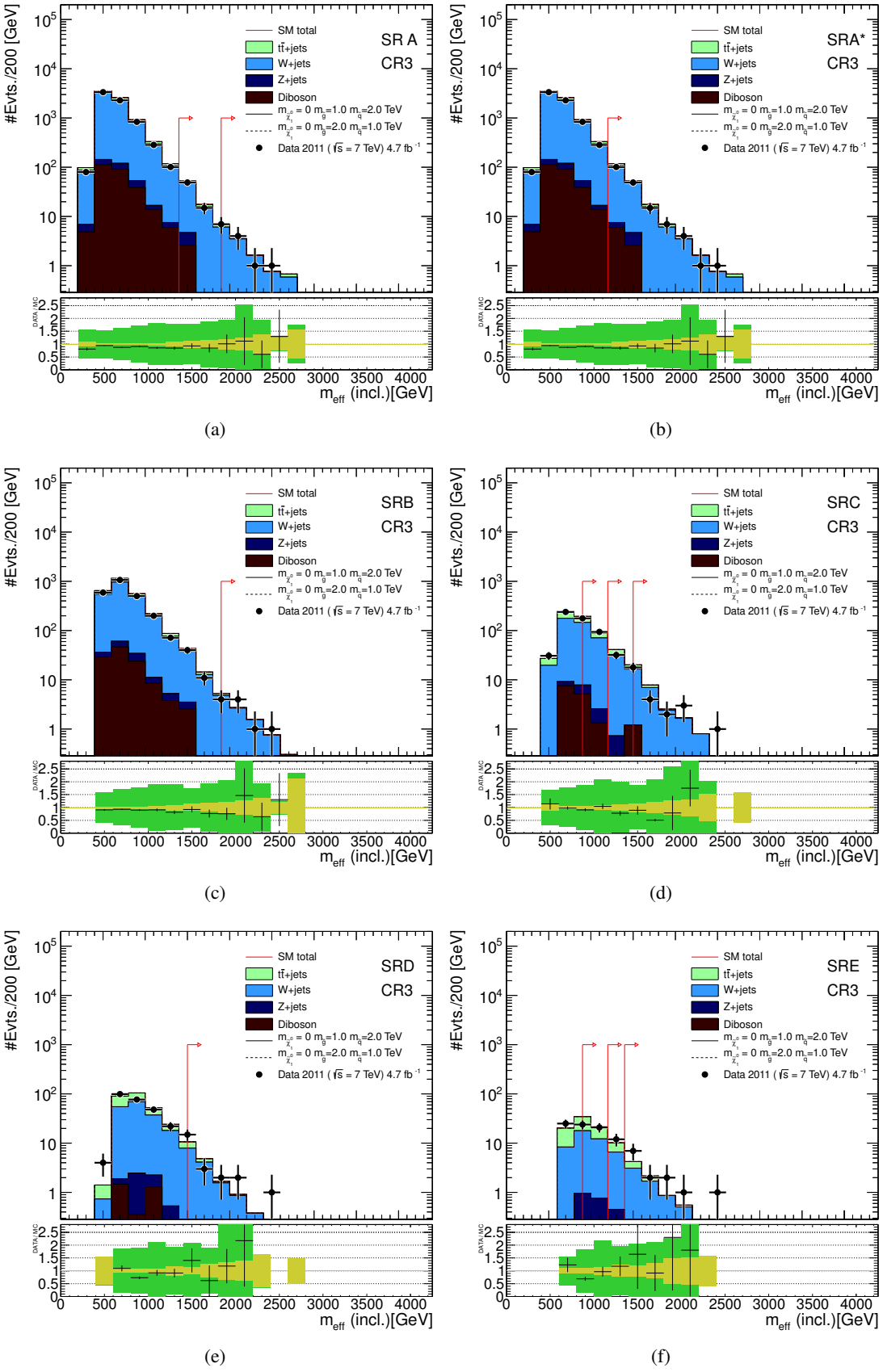

Figure 6.7: $meff$ (incl.) distributions of all search channels A-E in CR3. Each top panel shows the SM background expectations. MC simulation expectations are normalized to luminosity. The multi-jet background is estimated using the jet smearing method described in the text. Two benchmark model points with m($\tilde{\chi}^0$) =0 TeV, m($\tilde{q}$)=1.0 TeV, m($\tilde{g}$)=2.0 TeV and m($\tilde{\chi}^0$) =0 TeV, m($\tilde{q}$)=2.0 TeV, m($\tilde{g}$)=1.0 TeV, respectively. The arrows indicate the locations of the lower edges of the signal regions. The bottom panel shows the fractional deviation of the data from the total unscaled background estimate. The light (yellow) band shows the combined experimental uncertainties on the unscaled background estimates from jet energy scale, jet energy resolution, the effect of pile-up, the treatment of energy outside of reconstructed jets and MC simulation sample size. The medium (green) band includes also the total theoretical uncertainties.

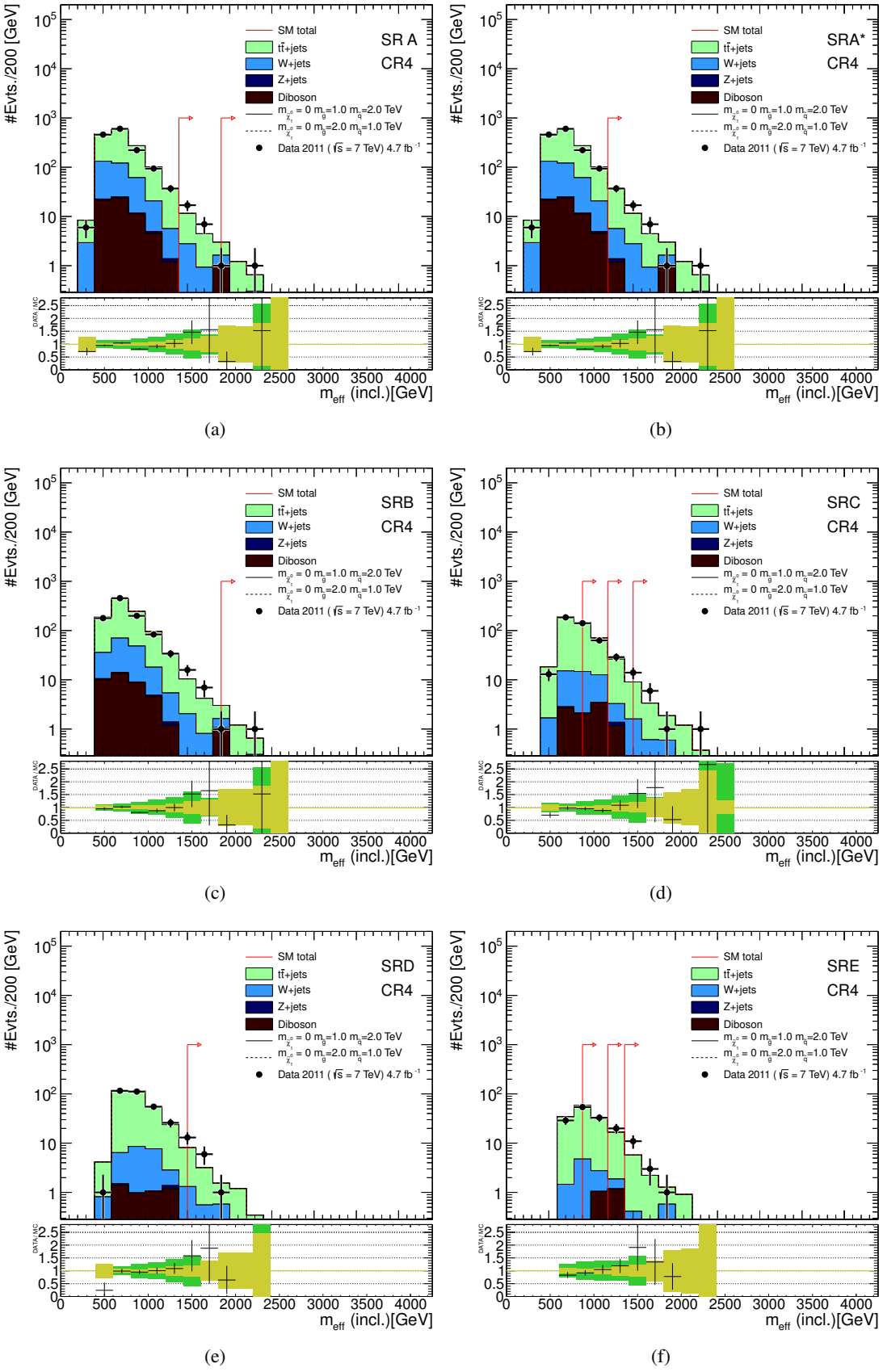

Figure 6.8: *meff* (incl.) distributions of all search channels A-E in CR4. Each top panel shows the SM background expectations. MC simulation expectations are normalized to luminosity. The multi-jet background is estimated using the jet smearing method described in the text. Two benchmark model points with m($\tilde{\chi}^0$) =0 TeV, m($\tilde{q}$)=1.0 TeV, m($\tilde{g}$)=2.0 TeV and m($\tilde{\chi}^0$) =0 TeV, m($\tilde{q}$)=2.0 TeV, m($\tilde{g}$)=1.0 TeV, respectively. The arrows indicate the locations of the lower edges of the signal regions. The bottom panel shows the fractional deviation of the data from the total unscaled background estimate. The light (yellow) band shows the combined experimental uncertainties on the unscaled background estimates from jet energy scale, jet energy resolution, the effect of pile-up, the treatment of energy outside of reconstructed jets and MC simulation sample size. The medium (green) band includes also the total theoretical uncertainties.

6.8 Validation regions

Two kinds of validation regions are defined. VR1b and VR1c are sensitive to fully leptonic $t\bar{t}$ decays as they require as CR1b exactly two opposite sign leptons. In VR1b the di-lepton invariant mass $m(ll)$ is required to be within $|m(ll) - m(Z)| > 25\,GeV$. The m_{eff} distributions are shown in Fig. 6.9. The statistics due to the requirement of the two leptons is poor especially in the high m_{eff} and high jet multiplicity channels, the cross check with this region is only meaningful in the low m_{eff} and low jet multiplicity channels.
VR1c does require exactly two opposite sign leptons with opposite flavour (electron and muon) with a p_{T} requirement of 25 GeV for electrons and 20 GeV for muons, repsectively. No cut on the di-lepton invariant mass is applied. Fig. 6.10 shows the m_{eff} distribution for all search channels, and as in VR1b the cross check with this region is only meaningful in low m_{eff} and low jet multiplicity search channels.

The other set of validation regions are targeted mainly at multi-jets events. A property of the multi-jets background is that jets and $E_{\text{T}}^{\text{miss}}$point in the same direction. Using this fact CR2 was defined with a cut on $\Delta\phi(j_i, E_{\text{T}}^{\text{miss}})$ of the selected jets to be smaller than 0.2. VR2 is defined in the intermediate $\Delta\phi(j_i, E_{\text{T}}^{\text{miss}})$ region so that $0.2 < \Delta\phi(j_i, E_{\text{T}}^{\text{miss}})(min) < 0.4$, with $\Delta\phi(j_i, E_{\text{T}}^{\text{miss}})$ (min) being the the minimum of the three hardest jets with $p_{\text{T}} > 40\,GeV$. The m_{eff} distributions are shown in Fig. 6.11. The intermediate $\Delta\phi(j_i, E_{\text{T}}^{\text{miss}})$ region is enriched with all background processes involved in this search, thus it provides a good candidate to cross check the simultaneous normalization of all processes.
VR5 requires the $E_{\text{T}}^{\text{miss}}/m_{\text{eff}}(Nj)$ cut to be inverted per channel, the m_{eff} distributions are shown in Fig. 6.12. VR5 is as well populated by all almost all background processes involved. For low values of $m_{\text{eff}}(incl)$ the distribution of data and MC expectation normalized to luminosity plus the data driven multi-jets estimate seem to match quite well, but the at higher values of $m_{\text{eff}}(incl)$ the data exceed the prediction. These events do carry only a small amount of $E_{\text{T}}^{\text{miss}}$ and the data driven multi-jets prediction carries a large uncertainty. Thus it does not serve as a good validation region.

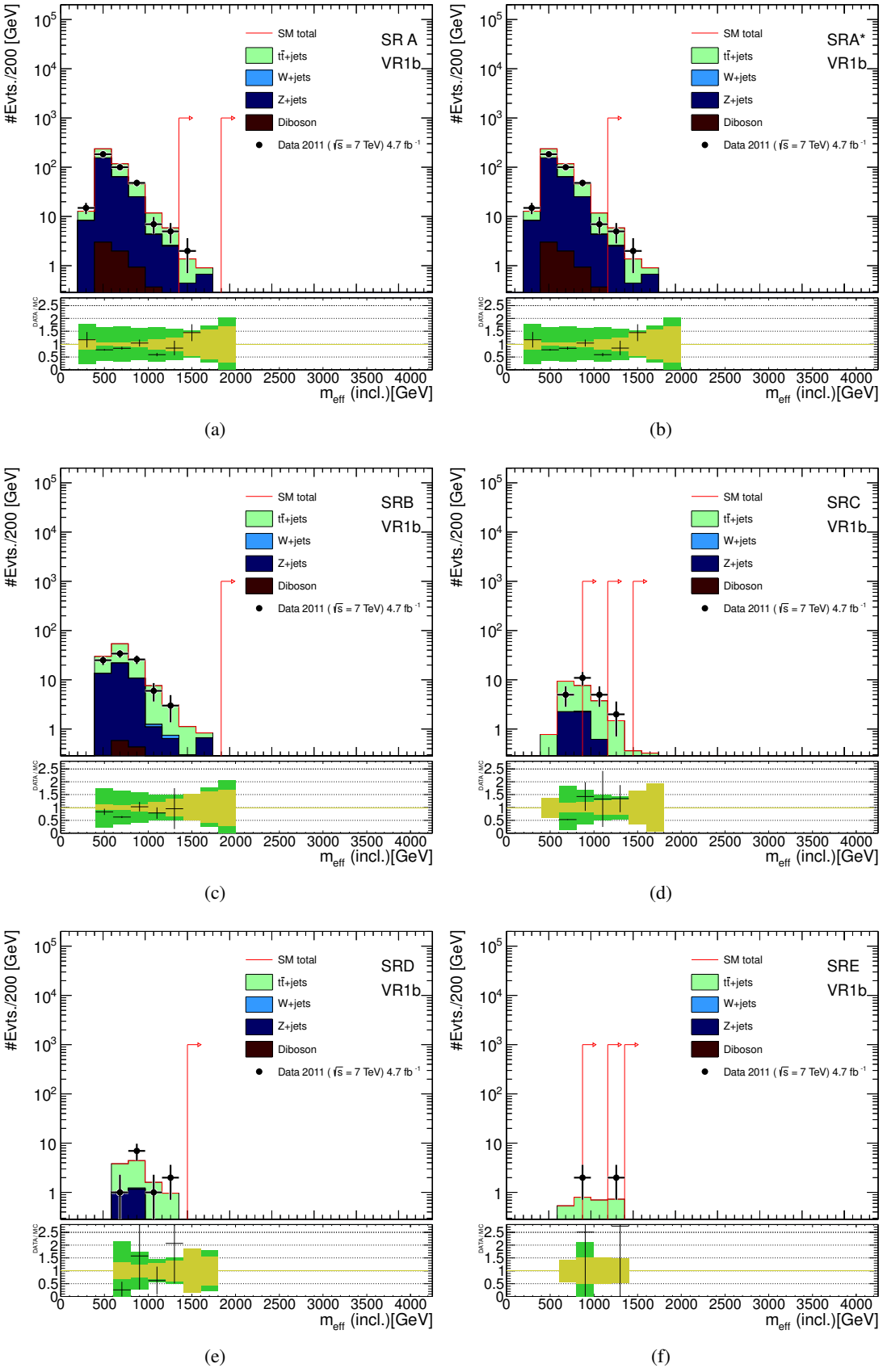

Figure 6.9: *meff* (incl.) distributions of all search channels A-E in VR1b. Each top panel shows the SM background expectations. MC simulation expectations are normalized to luminosity. The multi-jet background is estimated using the jet smearing method described in the text. The arrows indicate the locations of the lower edges of the signal regions. The bottom panel shows the fractional deviation of the data from the total unscaled background estimate. The light (yellow) band shows the combined experimental uncertainties on the unscaled background estimates from jet energy scale, jet energy resolution, the effect of pile-up, the treatment of energy outside of reconstructed jets and MC simulation sample size. The medium (green) band includes also the total theoretical uncertainties.

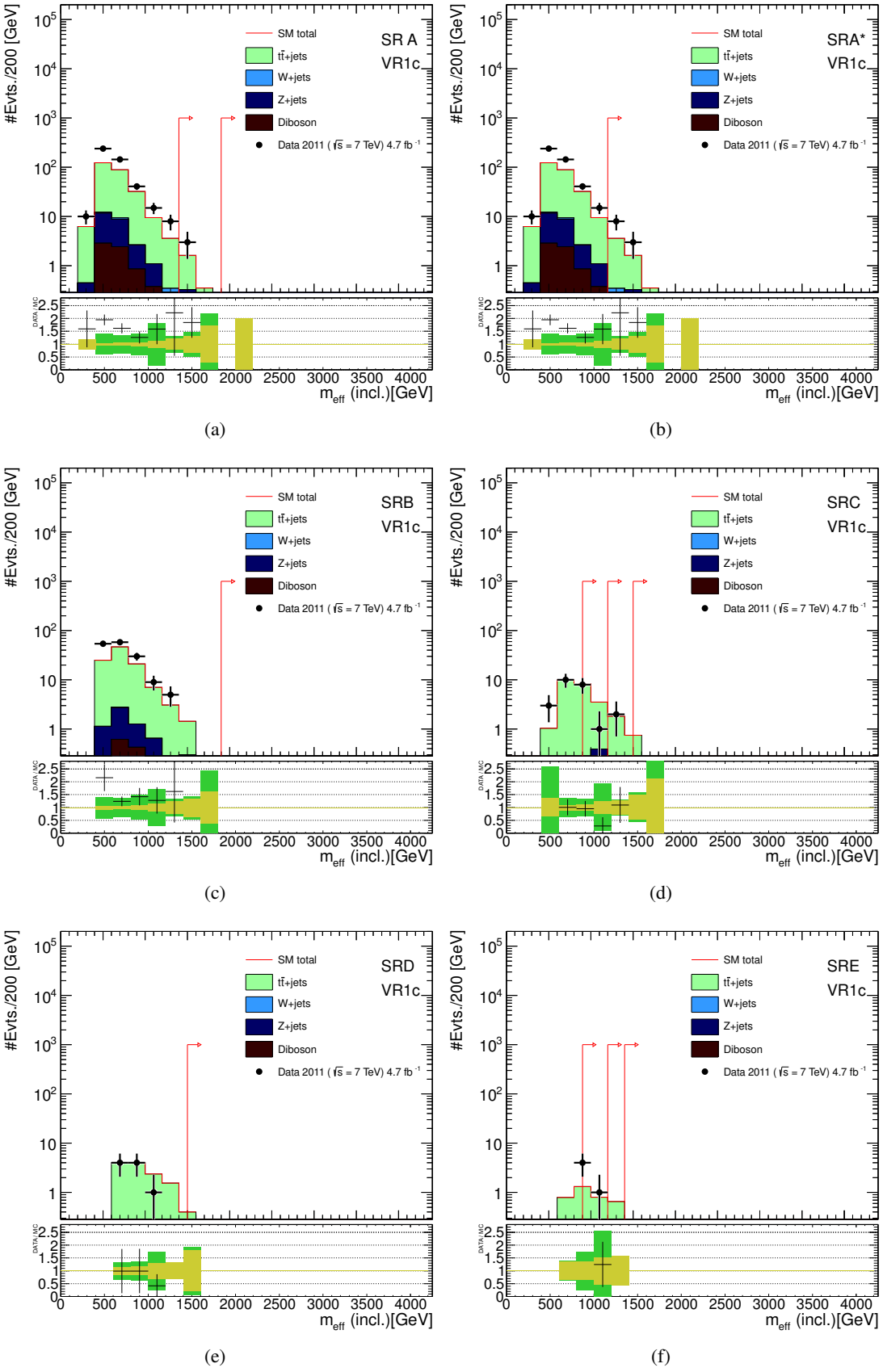

Figure 6.10: *meff* (incl.) distributions of all search channels A-E in VR1c. Each top panel shows the SM background expectations. MC simulation expectations are normalized to luminosity. The multi-jet background is estimated using the jet smearing method described in the text. The arrows indicate the locations of the lower edges of the signal regions. The bottom panel shows the fractional deviation of the data from the total unscaled background estimate. The light (yellow) band shows the combined experimental uncertainties on the unscaled background estimates from jet energy scale, jet energy resolution, the effect of pile-up, the treatment of energy outside of reconstructed jets and MC simulation sample size. The medium (green) band includes also the total theoretical uncertainties.

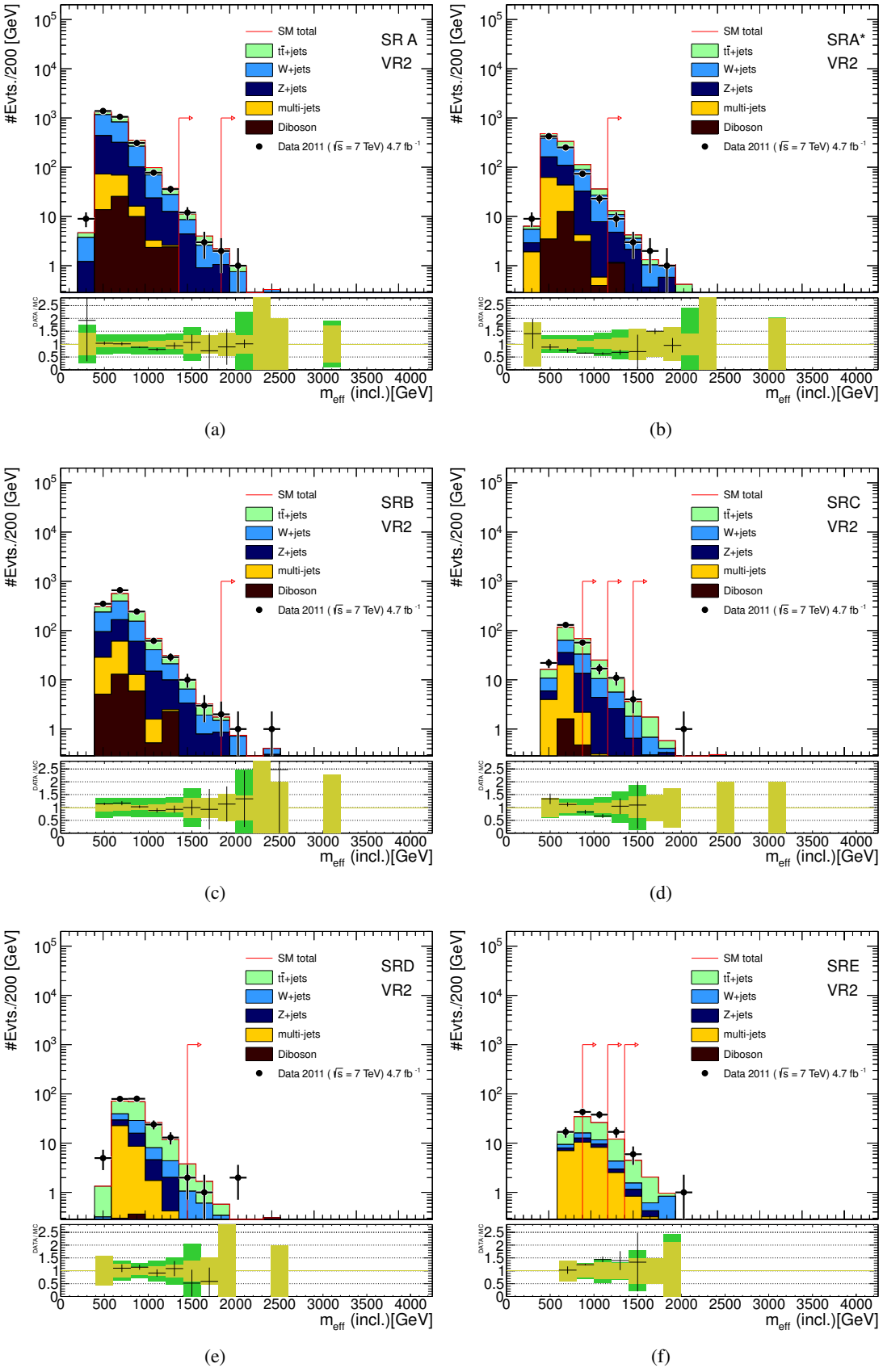

Figure 6.11: $meff$ (incl.) distributions of all search channels A-E in VR2. Each top panel shows the SM background expectations. MC simulation expectations are normalized to luminosity. The multi-jet background is estimated using the jet smearing method described in the text. The arrows indicate the locations of the lower edges of the signal regions. The bottom panel shows the fractional deviation of the data from the total unscaled background estimate. The light (yellow) band shows the combined experimental uncertainties on the unscaled background estimates from jet energy scale, jet energy resolution, the effect of pile-up, the treatment of energy outside of reconstructed jets and MC simulation sample size. The medium (green) band includes also the total theoretical uncertainties.

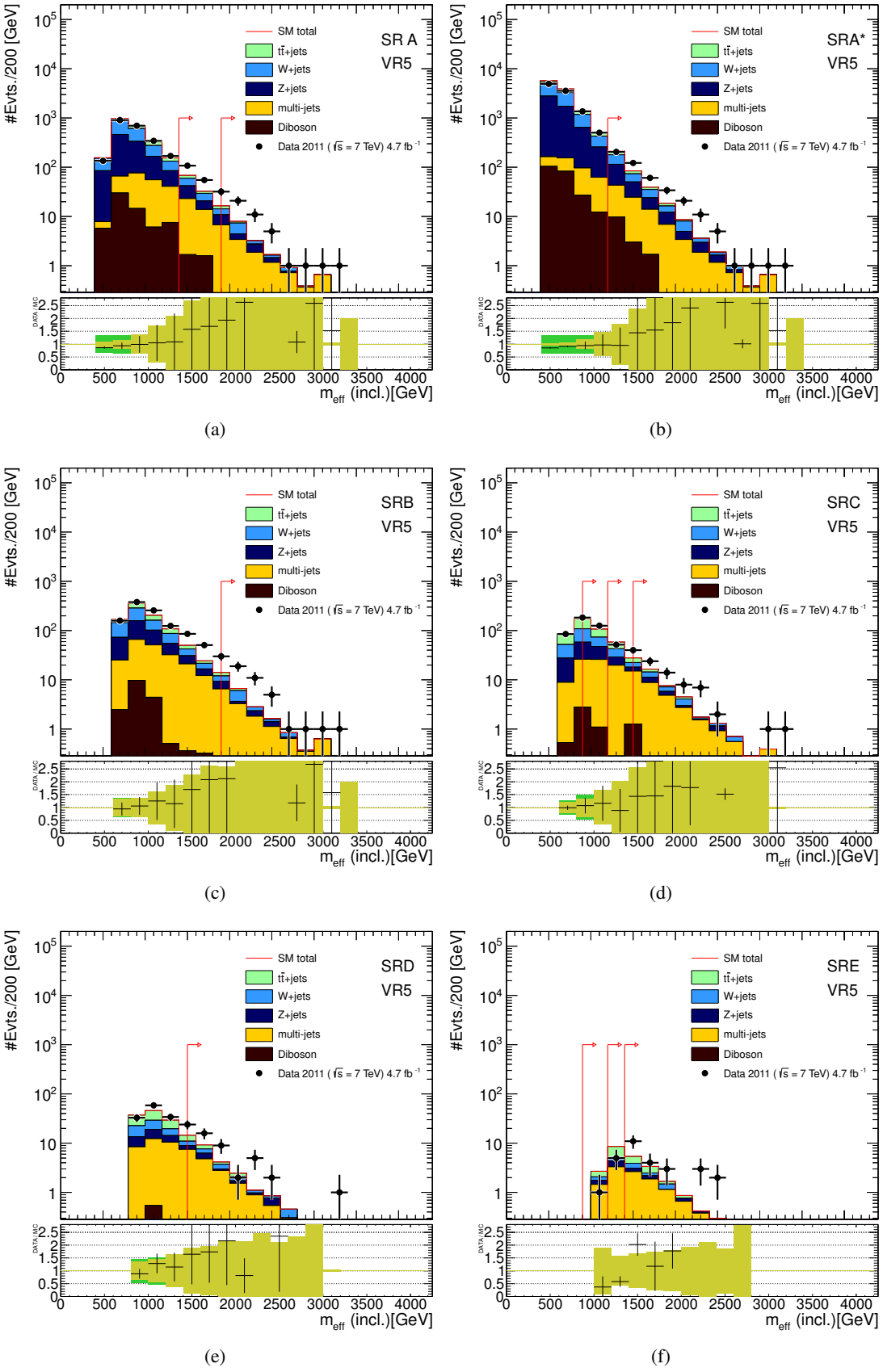

Figure 6.12: $meff$ (incl.) distributions of all search channels A-E in VR5. Each top panel shows the SM background expectations. MC simulation expectations are normalized to luminosity. The multi-jet background is estimated using the jet smearing method described in the text. The arrows indicate the locations of the lower edges of the signal regions. The bottom panel shows the fractional deviation of the data from the total unscaled background estimate. The light (yellow) band shows the combined experimental uncertainties on the unscaled background estimates from jet energy scale, jet energy resolution, the effect of pile-up, the treatment of energy outside of reconstructed jets and MC simulation sample size. The medium (green) band includes also the total theoretical uncertainties.

6.9 Simultaneous Normalisation and Statistical Interpretation

6.9.1 Introduction

This section presents the statistical methods used for the interpretation of the observed data [9, 10]. Is is mandatory to use the most accurate statistical methods available given the costs and effort that was put in the LHC and accompanying experiments. Little improvements in e.g. sensitivity to specific models due to improved statistical techniques can save valuable operation time of the LHC. Understanding the data most precisely is even more important when it comes to decisions on future operation times of the LHC. These arguments hold for every large scale experiment where the data taking is bound to enormous costs and large human efforts.

A basic introduction on the use of likelihoods and other statistical methods in HEP can be found in Ref. [122]. Hypothesis tests carried out in this analysis are based on the likelihood principle, which assumes that we can build a likelihood function that reflects the experimental environment and theoretical considerations accurately.

The likelihood and its components are implemented in the RooStats [123] framework which itself is based on the RooFit [124] framework. RooFit is designed to allow for model building independent of the specific choices of the probability density functions (pdf). RooStats is designed to use the models built with RooFit for hypothesis testing. HistFactory [125] is a tool on top of RooStats and RooFit providing solutions to likelihood model building in the most common cases.

The following Sec. 6.9.2 describes the construction of the likelihood function containing all information on a measurement of a counting experiment per channel A–E loose to tight. The examination and use of the likelihood is split in different modes, which are called “Background”, “Extended background” , “Discovery” and “Exclusion” fit modes. The “Background” and the “Extended background” modes are used to test the assumptions of the likelihood principle that the likelihood function reflects the experimental environment and theoretical considerations given observations in phase space regions not sensitive to supersymmetric signatures.

The “Background ” mode normalizes all background processes in all CR and is used to gather confidence in the normalization procedure, but is not used to estimate the background contamination in the SR. The “Extended background” mode normalizes all processes in the CR and VR. In the “Discovery ” mode the SR is added to the fit together with a generic non-SM signal process in the SR.

The “Discovery ” and “Exclusion ” fit modes are used to interpret observations in phase space regions sensitive to signatures from supersymmetric particles. The estimated background in Tab. 6.24 as well as the breakdown of the uncertainties in Tab. 6.27 in the SR are calculated in the “Discovery” mode. In the “Exclusion” mode the generic non-SM signal process is replaced by the signal prediction in SR and CRs from a given signal model together with its experimental uncertainties.

The minimization of the likelihood coincides with a simultaneous normalization of the SM background processes. A semi data-driven normalization of the main background processes is performed via the simultaneous normalization of the SM processes in the various CR. Thus a consistent background estimation and the proper propagation of statistical and systematic uncertainties in the SR is ensured.

The simultaneous normalization should in principle work for any number of events populating the various regions, however problems arise when the number of observed events in some regions are small or even zero. This situation is at the very edge of the profile likelihood idea and technical difficulties occur. This is discussed with the help of a toy example in Appendix F. The simultaneous normalization works from a technical point of view as long as there is no region with zero events. This fact was used to find the lower bounds on the m_{eff} requirements on the CRs in Sec. 6.1 and was therefore included in the optimization of the analysis.
Is the observed data in regions sensitive to supersymmetric particles compatible with the background estimation or not is the core question in every analysis. The agreement or disagreement must be given in a quantifiable way. Therefore a test statistic is defined based on the likelihood on which hypothesis tests are carried out. Any hypothesis test distinguishes between two hypotheses. In general they are called NULL-hypothesis H_0 and alternate hypothesis H_1. In HEP usually there are two kinds of hypothesis tests of interest. The first case distinguishes between the SM expectation as NULL-hypothesis and the SM plus a general non-SM signal as the alternative hypothesis. The second case distinguishes between the SM expectation as NULL-hypothesis and the SM plus a specific, highly predictive signal model as the alternative hypothesis. Which of the hypothesis is assigned to be the NULL-hypothesis and which the alternative is not important as there is no qualitatively difference between them from a statistical point of view.
In HEP a variety of test statistics have been used. In the LEP Higgs searches, e.g., a likelihood ratio $-2ln\frac{L(s+b)}{L(b)}$ was used. The test statistic used in this search is based on a Profile Log Likelihood Ratio (PLLR) and is discussed in Sec. 6.9.5. Hypothesis tests are carried out to test the compatibility of the data with the estimated background as well as to exclude data signal models based on the CLs [126] prescription which is described in Sec. 6.9.5.3.

6.9.2 The likelihood function

In the following R is a representative for any counting region in this analysis and thus R ∈ (SR, CR1a, CR1b, CR2, CR3, CR4, VR1b, VR1c, VR2, VR5) and i a representative for any background process involved, that is those defined in the previous sections Z+jets (Z), multi-jets (QCD), W+jets(W), $t\bar{t}$ (T) and Diboson (D) so that $i \in (Z, QCD, W, T, D)$.

The likelihood function differs slightly for the different modes. In the discovery and exclusion mode the likelihood function for each of the channels A–E loose to tight is the product of Poisson distributions, one for the signal region P_{SR} and one for each of the control regions constraining the Z+jets (CR1a/b), multi-jets (CR2), W+jets (CR3) and $t\bar{t}$ (CR4) processes, labelled P_{CRX}, with $X \in (1a, 1b, 2, 3, 4)$ and of the PDFs modelling the systematic uncertainties C_{Syst}.

$$L(\boldsymbol{n}|\boldsymbol{\mu}, \boldsymbol{s}, N, \boldsymbol{\theta}) \quad = \quad P_{\text{SR}} \times P_{\text{CR1a}} \times P_{\text{CR1b}} \times P_{\text{CR2}} \times P_{\text{CR3}} \times P_{\text{CR4}} \times C_{\text{Syst}} \tag{6.7}$$

with

- $\boldsymbol{n}$ being the set of measurements. In particular $\boldsymbol{n} = (n_{SR}, n_{CR1a}, n_{CR1b}, n_{CR2}, n_{CR3}, n_{CR4})$
- $\boldsymbol{\mu}$ denoting the *process* strength vector containing all free parameters of the likelihood model associated directly with a process that is allowed to be scaled. In particular $\boldsymbol{\mu} = (\mu, \mu_Z, \mu_{QCD}, \mu_W, \mu_T)$ with μ being the non-SM signal strength(the index S for signal is being omitted to be in agreement with statistics conventions, that is $\mu = \mu_S$). μ_i with $i \in (Z, QCD, W, T)$ is the strength associated to the background process i. Elements of $\boldsymbol{\mu}$ are free parameters in the model. A free parameter is technically realized assuming a uniform distribution with no restriction on the domain (or such that the parameter never hits the domain bounds). The initial strength for each background process is 1.
- $\boldsymbol{s}$ being the vector of estimated non-SM signal events from MC in all regions R. In particular $\boldsymbol{s} = (s, s_{CR1a}, s_{CR1b}, s_{CR2}, s_{CR3}, s_{CR4})$ with s being the estimated amount of signal in the SR ($s = s_{SR}$) and s_R being the estimated amount of non-SM signal events in region R.
- N being the matrix of initially estimated background events per process i and per region R. That is the entries of N are $N_{i,R}$. $N_{i,R}$ are calculated either via MC normalized to the integrated luminosity for W+jets, $t\bar{t}$ and Diboson in all regions and Z+jets in CR1b or with data driven methods for multi-jets in all regions and Z+jets in CR1a and SR as described in previous chapters.
- $\boldsymbol{\theta}$ is the set of nuisance parameters that is used to parametrise systematic uncertainties.

Any P_R depends on

$$P_R \quad = \quad P(n_R|\lambda_R(\boldsymbol{\mu}, s_R, \boldsymbol{N}_i^R, \boldsymbol{\theta})) \tag{6.8}$$

with n_R the observed event in region R and λ_R the Poisson mean. Furthermore λ_R depends on s_R the amount of non-SM signal in region R and $\boldsymbol{N}_i^R$ the elements of $N_{i,R}$ corresponding to region R and follows the formula:

$$\lambda_R(\boldsymbol{\mu}, \boldsymbol{N}_i^R, \boldsymbol{\theta}) \quad = \quad \mu \cdot s_R \cdot U_{s,R}(\boldsymbol{\theta}) + \sum_i \mu_i \cdot N_i^R \cdot U_{i,R}(\boldsymbol{\theta}) + N_D^R \cdot U_{D,R}(\boldsymbol{\theta}) \tag{6.9}$$

Where as $U_{i,R}(\boldsymbol{\theta})$ is a function that parameterizes the systematic uncertainties on the N_i^R with $i \in (Z, QCD, W, T)$. The Diboson process is not normalized via a CR and thus is not associated with a scalable strength parameter and appears as a seperate term $N_D^R \cdot U_{D,R}(\boldsymbol{\theta}$.
Systematic uncertainties are included by constructing $U_{i,R}(\boldsymbol{\theta})$ and the corresponding probability density function $C_{Syst}(\boldsymbol{\theta})$. A general approach is described in Ref. [127]. Depending on the choice of the functional form of $C_{Syst}(\boldsymbol{\theta})$ the $U_{i,R}(\boldsymbol{\theta})$ are modelled. The standard choice for $C_{Syst}(\boldsymbol{\theta})$ is a normal distribution for each θ, thus $U_{i,R}(\boldsymbol{\theta})$ can be modelled as in the following

$$U_{i,R}(\boldsymbol{\theta}) = \left(1 \; + \; \sum_k \; \Delta_k^{i,R} \; \times \theta_k\right). \tag{6.10}$$

where $\Delta_k^{i,R}$ is the initially estimated relative impact of nuisance parameter θ_k on N_i^R. θ_k underlies a normal distribution $G_{Syst}(\theta_k) = C_{Syst}(\theta_k)$, its nominal value is 0 and is varied so that a value of ± 1 in θ_k corresponds an effective shift of $\pm\Delta_k^{i,R} \times N_i^R$ on N_i^R.

This procedure ensures a coherent treatment of correlated uncertainties. As an example serves the luminosity uncertainty θ_{lumi} being initially estimated to be $\Delta_{lumi}^{i,SR} = \Delta_{lumi}^{i,CR} = 2.7\%$ on an initial estimate from MC for process i normalized to integrated luminosity in a control region N_i^{CR} and the signal region N_i^{SR}.The underlying distribution is $G_{lumi}(\theta_{lumi})$. Thus the terms $N_i^{CR} \times (1 + \Delta_{lumi}^{i,CR} \times \theta_k)$ and $N_i^{SR} \times (1 + \Delta_{lumi}^{i,SR} \times \theta_k)$ do enter the likelihood via P_{SR} and P_{CR} and are *simultaneously* varied as in both terms θ_k occurs.

The proper inclusion of uncertainties arising from using and combining several finite MC samples is described in Ref. [128]. The treatment suggests to include for each MC sample a seperate term in the likelihood function. However this leads to a large number of free paramters. To avoid this another approach is implemented in the HistFactory packagage. In each bin l with contributions from limited MC sample sizes a nuisance paramters γ_l. The nuisance parameter γ_l is constructed so that it reflects the mean uncertainty from limited MC sample size over all samples affected in bin l. Including γ_l in the likelihood is done via expanding $U_{i,R}(\boldsymbol{\theta})$ to:

$$U_{i,R}(\boldsymbol{\theta}) = \left(1 \; + \; \sum_k \; \Delta_k^{i,R} \; \times \theta_k\right) \times \gamma_l \, . \tag{6.11}$$

The pdf $C_{Syst}(\gamma_l)$ describes the behaviour of the γ_l and is described by a Poission distribution $Poiss(\gamma_l\tau)$ with mean $\gamma_l\tau$. γ_l is set to 1 and τ reflects the affected number of expected events in bin l. The full C_{Syst} function is then given by the product of all pdf terms describing the nuisance paramters θ_k associated to systematic uncertainties $C_{Syst}(\theta_k)$ and all pdf terms describing the nuisance paramters γ_l describing limited MC sample size uncertainties $C_{Syst}(\gamma_l)$.

$$C_{Syst} = \prod_k C_{Syst}(\theta_k) \prod_l C_{Syst}(\gamma_l) \tag{6.12}$$

The vector $\boldsymbol{\theta}$ includes both θ_k and γ_l.

The TFs mentioned before in the text are used intrinsically in the likelihood. The CRs and the SR are coupled via the process strength vector $\boldsymbol{\mu}$. The same μ_i corresponding to a background process i is present in the λ parameter of the SR and the CRs. The μ_i are fixed by the measurements n_{CRX} in the CR. The amount of process i in SR $b_{i,SR}$ and a CR $b_{i,CR}$ is given by

$$b_i^{SR} = \mu_i \times N_i^{SR} \times U_{i,SR}(\boldsymbol{\theta}) \tag{6.13}$$

$$b_i^{CR} = \mu_i \times N_i^{CR} \times U_{i,CR}(\boldsymbol{\theta}) \tag{6.14}$$

$$\tag{6.15}$$

The TFs and their uncertainties U are defined to be

$$TF_{i,CR\to SR} = \frac{N_i^{SR}}{N_i^{CR}} \tag{6.16}$$

$$U_{i,CR\to SR} = \frac{U_{i,SR}(\boldsymbol{\theta})}{U_{i,CR}(\boldsymbol{\theta})} = \left(1 + \sum_k \Delta_k^{i,CR\to SR} \times \theta_k\right). \tag{6.17}$$

$U_{i,SR\to CR}$ being the effective uncertainty function and $\Delta_k^{i,CR\to SR}$ the relative uncertainty on $TF_{i,SR\to CR}$. In the example above with having the luminosity uncertainty as nuisance parameter θ_{lumi} present of the same magnitude, that is 2.7% on the N_i^{CR} and N_i^{SR} the uncertainty $\Delta_{lumi}^{i,CR\to SR}$ reduces to 0 as it cancels exactly out in the ratio $U_{i,SR\to CR}$. Any systematic uncertainty present in SR and CR is heavily reduced using this setup, that is estimating the components of SM background in SR relative to CRs.
In the background mode the likelihood reduces to

$$L(\boldsymbol{n}|\boldsymbol{\mu}, \boldsymbol{s}, N, \boldsymbol{\theta}) = P_{\text{CR1a}} \times P_{\text{CR1b}} \times P_{\text{CR2}} \times P_{\text{CR3}} \times P_{\text{CR4}} \times C_{\text{Syst}}\,. \tag{6.18}$$

so the SR is not present in the function.
In the extended background mode, that is the inclusion of i validation regions VR to the simultaneous normalization the likelihood is expanded to have the form:

$$L(\boldsymbol{n}|\boldsymbol{\mu}, \boldsymbol{s}, N, \boldsymbol{\theta}) = P_{\text{CR1a}} \times P_{\text{CR1b}} \times P_{\text{CR2}} \times P_{\text{CR3}} \times P_{\text{CR4}} \times \prod_{i\in\text{VR}} P_{\text{VR,i}} \times C_{\text{Syst}}\,. \tag{6.19}$$

6.9.3 Fit setups

6.9.3.1 Background fit

In the 'Background fit' mode the likelihood is minimized excluding the SR and VRs and excluding the non-SM signal strength μ. An example of this minimization of the fit to data in the background mode in the search channel SRC medium is visualized in Fig. 6.13. The minimization is performed with Minuit [129]. The likelihood is fitted only to the data in the CRs. The amount of events in the VRs and SR is extrapolated via the nominal TF. The fitted process strengths $\boldsymbol{\mu}$ and nuisance parameters θ_k are listed in Tab. 6.20. Listed are all floating parameters. The background fit is not heavily constrained albeit there are 5 measurements and 4 processes and thus 4 free parameters associated to processes. The only process which is constrained is the Z+jets process in CR1a and CR1b. However the sample size in CR1b is too low to have a significant impact. Thus the Z+jets process is mainly constrained by CR1a, this persists in all channels. The fit has even more Degrees Of Freedom (DOF) than the 4 from $\boldsymbol{\mu}$, that is those of the nuisance parameters $\boldsymbol{\theta}$. $\boldsymbol{\mu}$ are free parameters with an underlying uniform pdf, whereas the $\boldsymbol{\theta}$ are modelled as described in Sec. 6.9.2 and are already constrained before the fit by their analytical implementation C_{Syst}. Therefore the DOF of the nuisance parameters are usually not equally footed to those from $\boldsymbol{\mu}$.
The values and uncertainties of the fitted nuisance parameters are not far away from their initial guesses. The nuisance parameters which are implemented as described in Eq. 6.10 start the fit at the nominal value of 0. The fit result corresponds to the most probable set of nuisance parameters given the data and the

Var. Name	Fitted Val. ± Parabolic Unc.(MINOS)
μ_T	0.89 ± 0.34
μ_W	0.54 ± 0.23
μ_Z	0.97 ± 0.14
μ_{QCD}	0.94 ± 1.2
ℓ eff.	-0.03 ± 0.99
ℓ resoln.	0.01 ± 0.94
ℓ scale.	-0.00 ± 0.95
Generic Diboson	-0.03 ± 0.99
JER	0.00 ± 1
JES	-0.01 ± 0.29
Lumi	-0.00 ± 0.99
MET CellOut cluster	-0.00 ± 0.62
MET CellOut pileup	-0.00 ± 0.98
PDF	0.05 ± 0.99
Pileup	0.00 ± 1.1
QCD smear.	0.00 ± 1
Top theory	-0.06 ± 0.97
Trigger	0.00 ± 0.99
W+jets theory	0.00 ± 0.43
b-tag/veto eff.	0.03 ± 0.99
CR1b MC stat.	0.9 ± 0.2
CR2 MC stat.	1 ± 0.2
CR3 MC stat.	1 ± 0.04
CR4 MC stat.	1 ± 0.06

Table 6.20: Fitted values in the Background Fit mode in SRC medium. Listed are the background process strengths parameters in the upper box with a starting value of 1 and the nuisance parameters in the lower box with starting value of 0.

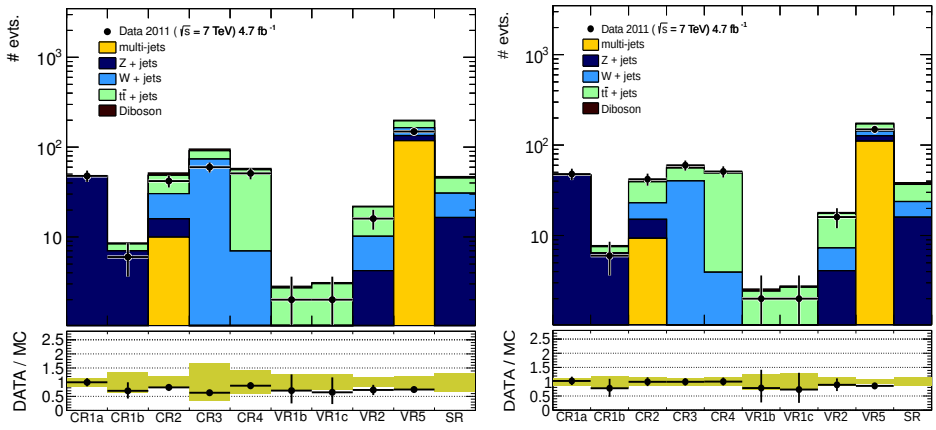

(a) (b)

Figure 6.13: *'Background Fit'* mode: The values of estimated events ***b*** before and after the fit are opposed to the data, the data in the SR is not shown. The likelihood is fitted only to the CRs. The number of events in the VRs and the SR are extrapolated via TFs.

configuration of the fit. The uncertainties are expressed in symmetric 68% C.L. intervals and are given by Minuit. A nuisance parameter which fitted value is not far away from 0 is close to its initial guess. An uncertainty close to its starting value of 1 tells us that the nuisance parameter is not constrained by the fit and thus acts as a free parameter (modulo its analytical implementation in C_{Syst}). A nuisance parameter having a larger uncertainty than one after the fit is a indication of a bad fit. A nuisance parameter having a smaller uncertainty than one means that some information of the likelihood is used to reduce the error on this parameter. This can be caused by auxiliary measurements or by correlation effects. Consider the case of a nuisance parameter being correlated among counting regions and fluctuations are present in these regions. The data is fluctuating above or below the expectation and thus it can happen that the nuisance parameter takes a most probable value different from 0. This means that the minimization tries to explain the difference between data and expectation with the uncertainty associated to this nuisance parameter. Furthermore it can happen that the uncertainty on the nuisance parameter is reduced compared to its initial guess.

It can be observed that the ALPGEN estimates in the extreme phase-space regions with large $E_{\text{T}}^{\text{miss}}$ and m_{eff} are harder than what was observed in data in the CRs. This is especially true for W+jets and Z+jets, but also for $t\bar{t}$ +jets generated with ALPGEN and persists through all channels.

6.9.3.2 Extended background fit

In the 'Extended Background Fit' mode the fit is more constrained by including more measurements in the VRs but keeping the same amount of DOFs, that is the $\boldsymbol{\mu}$ and $\boldsymbol{\theta}$. This is illustrated in Fig. 6.14 and the fitted parameters of the likelihood are listed in Tab. 6.21. The information from the data in the VRs reduces the uncertainty of the processes which are dominant in the VRs. In this example the multi-jets background and the top background via VR2 and VR5. VR1b and VR1c have not enough statistical power.

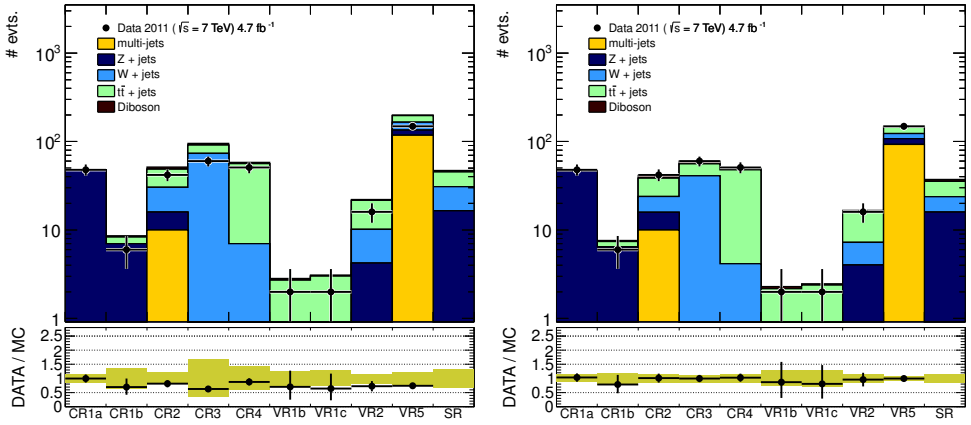

(a) (b)

Figure 6.14: *'Extended Background Fit'* mode: The values of estimated events $\boldsymbol{b}$ before and after the fit are opposed to the data, the data in the SR is not shown. The likelihood is fitted only to the CRs and VRs. The number of events in the SR is extrapolated via TFs.

6.9.3.3 Discovery fit

In the 'Discovery Fit' mode only CRs and the SR are included in the minimization. It is depicted in Fig. 6.16 and the fitted parameters of the likelihood are listed in Tab. 6.22. The generic non-SM process μ is included in the SR to consume any deviation of the estimated background events from the data in the SR. It ensures that the data in the SR does not constrain background processes. In general the 'Background Fit' and the 'Discovery Fit' should deliver similar results for the background strengths $\boldsymbol{\mu}$ and θ_k. The correlation matrix for selected floating paramters is shown in Fig. 6.15. The nuisance parameters associated to the theoretical uncertainty on the W+jets and $t\bar{t}$ +jets processes show a positive correlation to the corresponding process strenghts.

6.9.3.4 Exclusion fit

In the 'Exclusion Fit' mode only CRs and the SR is included in the minimization. It is depicted in

Var. Name	Fitted Val. ± Parabolic Unc.(MINOS)
μ_T	0.8 ± 0.28
μ_W	0.55 ± 0.24
μ_Z	0.97 ± 0.14
μ_{QCD}	0.99 ± 1.2
ℓ eff.	-0.02 ± 0.99
ℓ resoln.	0.01 ± 0.85
ℓ scale.	0.01 ± 0.9
Generic Diboson	-0.01 ± 1
JER	0.00 ± 1.1
JES	-0.03 ± 0.93
Lumi	-0.00 ± 1
MET CellOut cluster	-0.03 ± 0.83
MET CellOut pileup	0.00 ± 0.98
PDF	0.20 ± 0.9
Pileup	-0.05 ± 0.99
QCD smear.	-0.10 ± 1
Top theory	-0.30 ± 0.9
Trigger	0.01 ± 0.99
W+jets theory	0.00 ± 0.42
b-tag/veto eff.	0.10 ± 1
CR1b MC stat.	0.9 ± 0.2
CR2 MC stat.	1 ± 0.2
CR3 MC stat.	1 ± 0.04
CR4 MC stat.	1 ± 0.06
VR1b MC stat.	1 ± 0.2
VR1c MC stat.	1 ± 0.2
VR2 MC stat.	1 ± 0.08
VR5 MC stat.	0.9 ± 0.5

Table 6.21: Fitted values in the Extended Background Fit mode in SRC medium. Listed are the background process strengths parameters in the upper box with a starting value of 1 and the nuisance parameters in the lower box with starting value of 0.

Var. Name	Fitted Val. ± Parabolic Unc.(MINOS)
μ	-3.1 ± 8.7
μ_T	0.94 ± 0.45
μ_W	0.57 ± 0.46
μ_Z	0.97 ± 0.14
μ_{QCD}	0.94 ± 1.3
acc. Z+jets/γ	0.00 ± 0.99
ℓ eff.	-0.03 ± 0.99
ℓ resoln.	0.00 ± 0.94
ℓ scale.	0.00 ± 0.96
Generic Diboson	-0.03 ± 0.99
JER	-0.00 ± 1
JES	-0.20 ± 1
Lumi	-0.00 ± 0.99
MET CellOut cluster	-0.00 ± 0.65
MET CellOut pileup	-0.00 ± 0.98
PDF	0.05 ± 0.99
Pileup	-0.00 ± 1
QCD smear.	0.00 ± 1
Top theory	-0.07 ± 0.98
Trigger	0.00 ± 0.99
W+jets theory	0.01 ± 1
b-tag/veto eff.	0.03 ± 0.99
CR1b MC stat.	0.9 ± 0.2
CR2 MC stat.	1 ± 0.2
CR3 MC stat.	1 ± 0.04
CR4 MC stat.	1 ± 0.06
SR MC stat.	1 ± 0.07

Table 6.22: Fitted values in the Discovery Fit mode in SRC medium. Listed are the background process strengths parameters and the generic non-SM signal strength in the upper box with a starting value of 1 and the nuisance parameters in the lower box with starting value of 0.

Var. Name	Fitted Val. ± Parabolic Unc.(MINOS)
μ	1 ± 0
μ_T	0.99 ± 0.59
μ_W	0.52 ± 0.53
μ_Z	0.93 ± 0.13
μ_{QCD}	0.63 ± 1.6
acc. Z+jets/γ	-0.70 ± 0.9
ℓ eff.	-0.00 ± 0.99
ℓ resoln.	0.01 ± 0.82
ℓ scale.	0.02 ± 0.9
Generic Diboson	-0.09 ± 0.96
JER	0.10 ± 1
JES	-0.00 ± 0.25
Lumi	-0.07 ± 0.99
MET CellOut cluster	0.00 ± 0.41
MET CellOut pileup	-0.01 ± 1.3
PDF	0.09 ± 0.99
Pileup	0.01 ± 0.55
QCD smear.	-0.00 ± 0.91
Top theory	0.30 ± 1.1
Trigger	0.02 ± 0.99
W+jets theory	-0.02 ± 1
b-tag/veto eff.	0.01 ± 0.83
CR1b MC stat.	0.9 ± 0.2
CR2 MC stat.	1 ± 0.2
CR3 MC stat.	1 ± 0.04
CR4 MC stat.	1 ± 0.06
SR MC stat.	0.98 ± 0.05

Table 6.23: Fitted values in the Exclusion Fit mode in SRC medium. The signal corresponds to $m(\tilde{\chi}^0)$ = 0 TeV, $m(\tilde{q})$ = 2.0 TeV and $m(\tilde{g})$ = 1.0 TeV and the signal strength is set to 1. Listed are the background process strengths parameters in the upper box with a starting value of 1 and the nuisance parameters in the lower box with starting value of 0.

Fig. 6.23 and the fitted parameters of the likelihood are listed in Tab. 6.23. A signal model is included in the SR and where appropriate in the CR as well as all experimental uncertainties on the signal expectation.

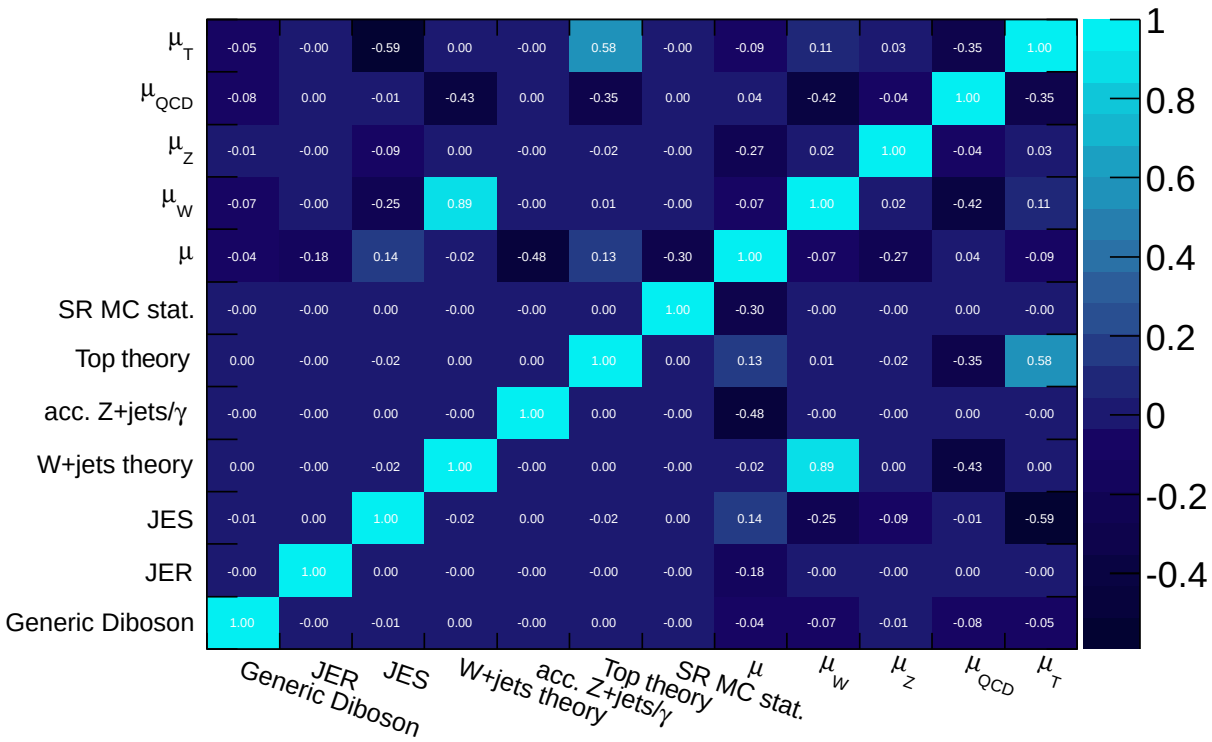

Figure 6.15: Correlation matrix of selected floating parameters in the discovery fit mode in SRC medium.

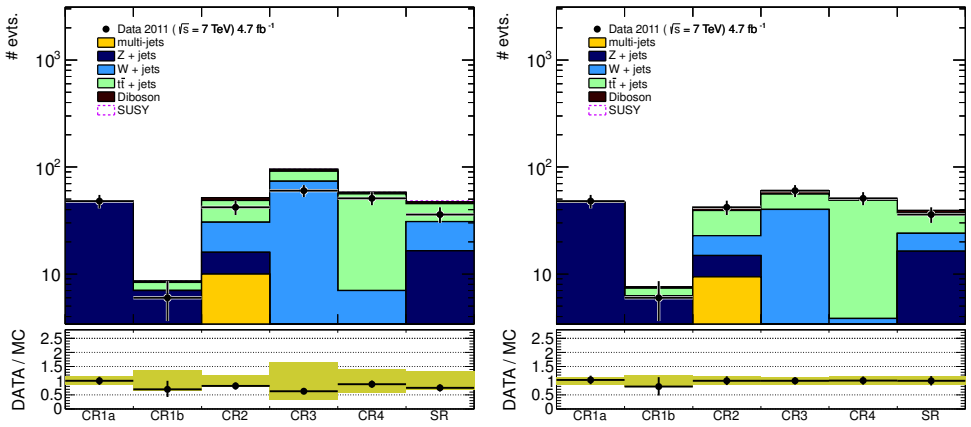

(a) (b)

Figure 6.16: *'Discovery Fit'* mode: The values of estimated events ***b*** before and after the fit are opposed to the data. The likelihood is fitted to the CRs and SR. The generic non-SM signal strenght is let free in the fit and absorbes any difference between data and estimated background in the SR.

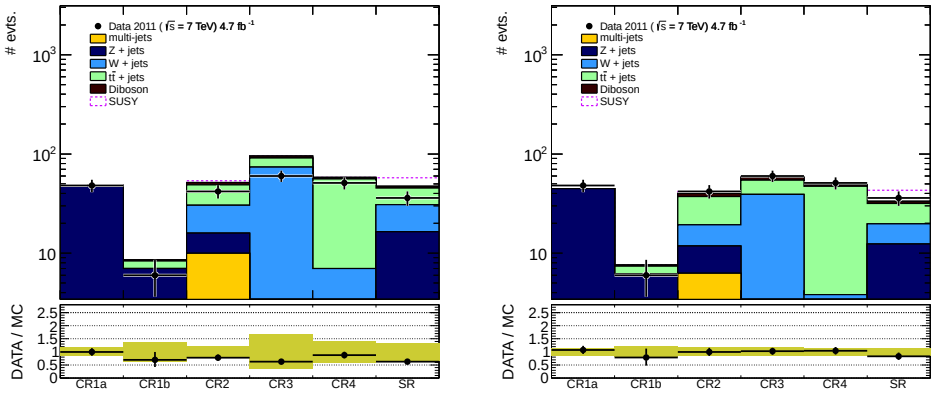

(a) (b)

Figure 6.17: *'Exclusion Fit'* mode: The values of estimated events ***b*** before and after the fit are opposed to the data. The likelihood is fitted to the CRs and SR. The signal 'SUSY' corresponds to $m(\tilde{\chi}^0) = 0\,\text{TeV}$, $m(\tilde{q}) = 2.0\,\text{TeV}$ and $m(\tilde{g}) = 1.0\,\text{TeV}$ and the signal strenght is set to 1.

6.9.4 Unconditional sampling

A well defined likelihood serves as a basis for the interpretation of the observed data. Sampling from this likelihood allows to test the behavior of the counting model in terms of rates and correlation coefficients. There are two basic kinds of samples that can be generated from the likelihood, the unconditional and the conditional dataset. The conditional dataset is derived by simply drawing i toy data events $\boldsymbol{n}_{i,gen}$ from the existing constraints on all parameters. Artificially generated data is labelled with the suffix "gen". The values from which the dataset is drawn are exactly those fed to the likelihood, e.g. the amount of W+jets in CR3 estimated via MC normalized to luminosity $\mu_W N_{W,CR3}$ with $\mu_W = 1$.
The unconditional dataset is derived by finding the most probable values of the parameters that are free in likelihood given the data $\boldsymbol{n}$, e.g. $\mu_W N_{W,CR3}$ with μ_W taking the most probable value given the data. These are usually labelled with a hat, that is $\hat{\mu}$, $\hat{\boldsymbol{\mu}}_{\boldsymbol{b}}$ and $\hat{\boldsymbol{\theta}}$. This is achieved by maximizing the likelihood. The most probable values are used as starting value to create the toy dataset containing i toy data events $\boldsymbol{n}_{i,gen}$ generated from the likelihood function. The investigation of the toy dataset gives information on how well the likelihood and the fit setup behaves given the data. The likelihood is maximized in each of the $\boldsymbol{n}_{i,gen}$. Of special interest are datasets with fixed values of the parameter of interest μ, that is $\mu = 0$ or $\mu = 1$. The maximized values in these cases are usually labelled with a double hat, that is $\hat{\hat{\boldsymbol{\mu}}}_b$ and $\hat{\hat{\boldsymbol{\theta}}}$, respectively. The starting values of the generation is found by maximizing the likelihood for a fixed value of the parameter of interest $\mu \in 0, 1$. Despite the fact that we usually say that we randomize the nuisance parameters, but indeed, they are always either fixed (in context of generating the (pseudo) observables), or fitted in the profile likelihood.
An example is given in Fig. 6.18, two sets of $\boldsymbol{n}_{i,gen}$ are generated in the exclusion fit mode of SRC medium, one assuming $\mu = 0$ and one assuming $\mu = 1$. The maximized signal strength $\hat{\mu}$ is plotted in Fig. 6.18(a) and the maximized background strengths $\hat{\mu}_W$ in Fig. 6.18(b) and $\hat{\mu}_T$ in Fig. 6.18(c). The distribution of the maximized nuisance parameter associated with the jet energy resolution $\hat{\theta}_{JER}$ is plotted in Fig. 6.18(d). The datasets reflects the fact that it turned out that the ALPGEN estimates in the extreme phase-space regions with large $E_{\mathrm{T}}^{\mathrm{miss}}$and m_{eff} are harder than that was observed in data in the CRs. The minimization does automatically take care of this in fitting the corresponding process strength μ_X to match the data. Therefore the maxima of the distributions of $\hat{\mu}_T$ and $\hat{\mu}_W$ are below 1. $\hat{\theta}_{JER}$ is distributed uniformly around 0 with a width of 1, as the underlying distribution of θ_{JER} is uniform. If the uncertainty would have been constrained by some parts of the likelihood, e.g. a shift of the mean or a reduced uncertainty it would be visible in this distribution. The absolute impact of the jet energy resolution uncertainty is implemented via the $\Delta_{JER}^{i,R}$ in Eq. 6.10.

In Fig. 6.19 the distributions of the maximized background process strength vector $\hat{\mu}_{QCD}$ in Fig. 6.19(a) are plotted. μ_{QCD} is defined to be positive. The parameter μ_{QCD} hits its lower bound which reflects the fact the the control region to normalize the multi-jets background CR2 is not very pure and thus sensitive to fluctuations of processes contaminating CR2. This does propagate to the evaluation of the covariance quality flag derived by Minuit, which ranges discretely from zero to three. Three is the best flag value indicating a properly calculated covariance matrix. Flag values of "1" or "2" indicate problems with the covariance quality matrix usually realted to the positive definiteness of the matrix. Generated events labelled with a flag of "0" indicate a not converged fit and are therefore discarded. However care must

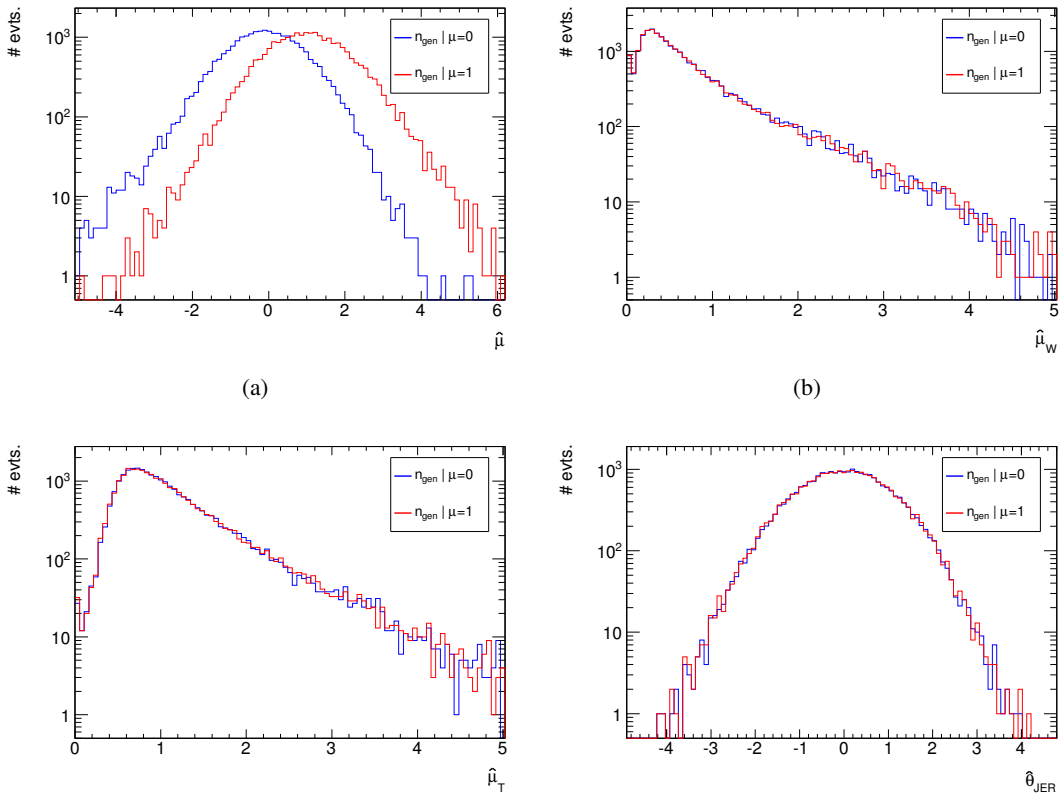

Figure 6.18: Distributions of parameters of the unconditional dataset of the exclusion fit mode in the search channel SRC medium for $\mu = 0$ and $\mu = 1$. The maximized signal strength $\hat{\mu}$ and the maximized background strengths $\hat{\mu}_W$ and $\hat{\mu}_T$ are plotted in 6.18(a), 6.18(b) and 6.18(c). $\hat{\theta}_{JER}$ is plotted in Fig. 6.18(d).

be taken in discarding generated events as this introduces a bias. The logarithm of the likelihood at the minimum is shown in Fig. 6.19(b).

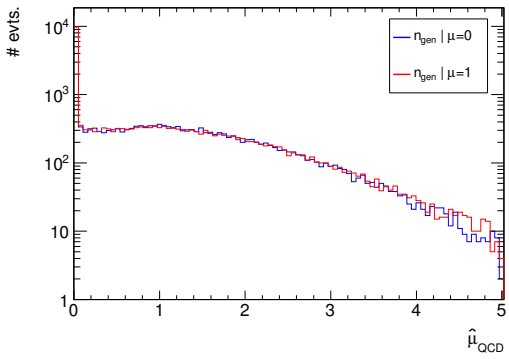

(a)

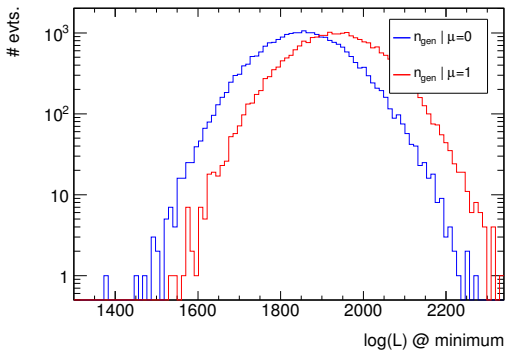

(b)

Figure 6.19: Distributions of parameters of the unconditional dataset of the exclusion fit mode in the search channel SRC medium for $\mu = 0$ and $\mu = 1$. The maximized background strength $\hat{\mu}_{QCD}$ is plotted in 6.19(a). The logarithm of the likelihood at the minimum is shown in Fig. 6.19(b).

6.9.5 The test statistic: Profile Log Likelihood Ratio (PLLR)

The parameter of interest is the non-SM signal strength μ, that is the first component of the process strength vector $\boldsymbol{\mu}$. In the following we distinguish between the non-SM signal strength μ and the vector of process strengths associated to background processes $\boldsymbol{\mu_b}$, that is $\boldsymbol{\mu} = (\mu, \boldsymbol{\mu_b})$. All other floating parameters than μ are nuisance parameters, that is their behavior and their maximized value are not of interest. However we distinguish between the process strength parameters of the background processes μ_i and the parameters θ_k that parametrise systematic uncertainties and monitor their behavior in the different fits. The maximized valued of the background processes μ_i do have a physics meaning, that is they tell us by how much the initial prediction is adjusted by the data in the CRs.
The test statistic is based on a profile log likelihood ratio $\Lambda(\boldsymbol{n}|\boldsymbol{\mu};\boldsymbol{\Theta})$ [130].

$$\Lambda(\mu) = -ln\frac{L(\boldsymbol{n}|\mu;\hat{\hat{\boldsymbol{\mu}}}_{\boldsymbol{b}};\hat{\hat{\boldsymbol{\Theta}}})}{L(\boldsymbol{n}|\hat{\mu};\hat{\boldsymbol{\mu}}_{\boldsymbol{b}};\hat{\boldsymbol{\Theta}})} \tag{6.20}$$

$\hat{\mu}$,$\hat{\boldsymbol{\mu}}_{\boldsymbol{b}}$,$\hat{\boldsymbol{\Theta}}$ maximize the likelihood function and $\hat{\hat{\boldsymbol{\mu}}}_{\boldsymbol{b}}$ and $\hat{\hat{\boldsymbol{\Theta}}}$ maximize the likelihood function for a given μ.
It has been shown in Ref. [130] that the the frequency distribution of $\Lambda(\mu)$ $f(\Lambda(\mu))$ approximates a χ^2-distribution in the large sample limit. Hypothesis testing in terms of a χ^2-distribution is well known. Expensive numeric simulation can be circumvented if the conditions of the approximation are fulfilled. In Fig. 6.20 an example of the distribution $f(\Lambda(\mu))$ is overlaid with a χ^2-distribution. The example corresponds to the search channel SRC medium in the exclusion mode. $f(\Lambda(\mu))$ was obtained by generating a toy dataset at the 68% C.L. upper limit on μ, that is $\mu = 1.6$ in this specific case.

6.9.5.1 Is the background estimate compatible with the data?

To test if the data is compatible with the background estimation the test statistic $q(0)$ is introduced:

$$q(0) = \begin{cases} -ln\frac{L(\boldsymbol{n}|0;\hat{\hat{\boldsymbol{\mu}}}_{\boldsymbol{b}};\hat{\hat{\boldsymbol{\Theta}}})}{L(\boldsymbol{n}|\hat{\mu};\hat{\mu}_b;\hat{\boldsymbol{\Theta}})} & \hat{\mu} \geq 0 \\ 0 & \hat{\mu} < 0 \end{cases} \tag{6.21}$$

An example of the distribution $f(q(\mu)|\mu = 0)$ is plotted in Fig. 6.21. The conditional dataset of the $\mu = 0$ hypothesis was generated as described in Sec. 6.9.4 and q(0) was calculated for each of the generated toy events. The conditional dataset is derived maximizing the likelihood with $\mu = 0$ and find the most probable values for μ_b and Θ that is $\hat{\hat{\boldsymbol{\mu}}}_{\boldsymbol{b}}$ and $\hat{\hat{\boldsymbol{\Theta}}}$, respectively. The maximized values are used as starting value to create toy datasets generated from the likelihood function. $q(0)^{obs}$ is the observed test statistic value. $q(0)$ is defined to be 0 if the observed amount of data is not as large as the estimated background, so that $\hat{\mu}$ is smaller than 0. A large observed value of $q(0)$ would indicate an incompatibility of the data and the background. In this specific example the observed value of $q(0)^{obs}$ is in the bulk of the generated toy dataset at ~ 0. This means that there is either good agreement of the data and the estimated background

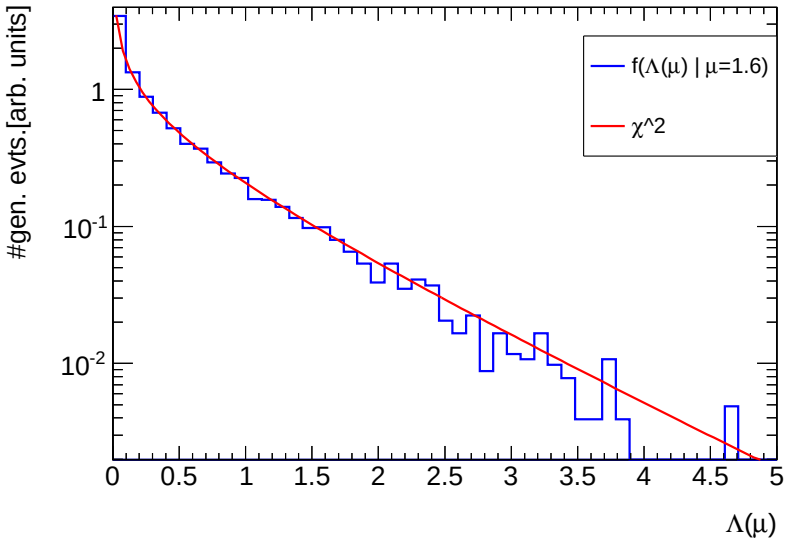

Figure 6.20: Distribution of $\Lambda(\mu)|\mu = 1.6$ opposed to a χ^2 distribution with one degree of freedom.

or the observed data is even less than the estimated background. In the definition of the test statistic $q(0)$ these two cases are not distinguished as we are only interested in positive signal event counts.
The quantification of the compatibility of the data and the background estimate is given by the p-value p_0, which is defined to be:

$$p_0 = \int_{q(0)^{obs}}^{\infty} f(q(\mu)|\mu = 0)dq(0) \tag{6.22}$$

$f(q(\mu)|\mu = 0)$ is normalized to unity. p_0 reflects how probable it is that the observed data is compatible with the $\mu = 0$ hypothesis given that $\mu = 0$ is true. A small p_0 indicates a disagreement between the data and the background estimate. Any p-value p can be stated in units of standard deviations of a Gaussian

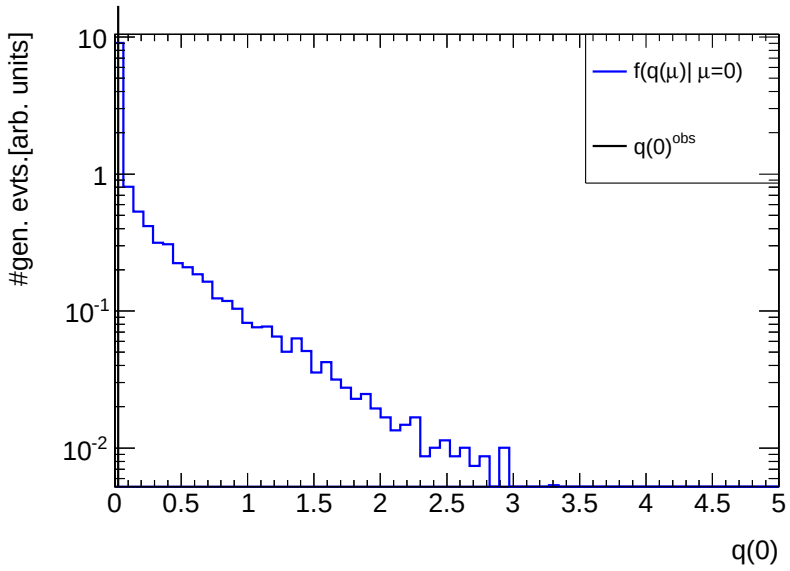

Figure 6.21: Distribution of the test statistic distribution $q(0)$ of the conditional dataset $f(q(\mu)|\mu = 0)$ in SRC medium.

distribution, which is commonly called significance Z by the error function $erf = \frac{2}{\sqrt{\pi}} \int_0^x e^{-t^2} dt$.

$$Z = erf^{-1}(1 - 2p) \cdot \sqrt{2}$$

When the p_0-value of a measurement falls below a threshold value p_{thres} or equivalently Z higher above a threshold Z_{thres}, one concludes that the data is not described by the background only hypothesis and therefore this hypothesis can be rejected. The "5σ" standard, which corresponds to a Z of 5 and a p-value of $2.9 \cdot 10^{-7}$, is widely used in the HEP community [131].

6.9.5.2 Is a specific supersymmetric model compatible with the data?

When testing the compatibility of a specific supersymmetric signal and the data a different test statistic $\tilde{q}(\mu)$ is defined. $\tilde{q}(\mu)$ is defined as in Ref. [130] and distinguishes between three cases of $\hat{\mu}$:

$$\tilde{q}(\mu) = \begin{cases} -ln\frac{L(\boldsymbol{n}|\mu;\hat{\hat{\boldsymbol{\mu}}}_b;\hat{\hat{\boldsymbol{\Theta}}})}{L(\boldsymbol{n}|0;\hat{\mu}_b;\hat{\boldsymbol{\Theta}})} & \hat{\mu} < 0 \\ -ln\frac{L(\boldsymbol{n}|\mu;\hat{\hat{\boldsymbol{\mu}}}_b;\hat{\hat{\boldsymbol{\Theta}}})}{L(\boldsymbol{n}|\hat{\mu};\hat{\boldsymbol{\mu}}_b;\hat{\boldsymbol{\Theta}})} & 0 \leq \hat{\mu} \leq \mu \\ 0 & \hat{\mu} > \mu \end{cases} \tag{6.23}$$

If $\hat{\mu} > \mu$ the observed amount of data is larger than the background plus the signal estimate. If $0 \leq \hat{\mu} \leq \mu$ the observed amount of data is smaller than the background plus signal estimate but larger than the background only estimate. When $\hat{\mu} < 0$ the amount of data is even smaller than the background only estimate. An example of the distributions $f(\tilde{q}(\mu))$ is plotted in Fig. 6.22. The conditional datasets are obtained by maximizing the likelihood with $\mu = 0$ to obtain the dataset corresponding to the distribution $f(\tilde{q}(\mu)|\mu = 0)$ and with $\mu = 1$ to obtain the data set corresponding to $f(\tilde{q}(\mu)|\mu = 1)$, respectively.

The following quantities are of interest

- $\tilde{q}(\mu)^{obs}$ is the observed test statistic value.
- The p-value p_0^* is calculated as

$$p_0^* = \int_{\tilde{q}(\mu)^{obs}}^{\infty} f(\tilde{q}(\mu)|\mu = 0) d\tilde{q}(\mu) \tag{6.24}$$

  thus it reflects how probable it is that the observed data is consistent with the $\mu = 0$ hypothesis given that $\mu = 0$ is true. Note that p_0^* is different from p_0 as they were derived from different test statistics.

- The p-value p_1 is calculated as follows:

$$p_1 = \int_{\tilde{q}(\mu)^{obs}}^{\infty} f(\tilde{q}(\mu)|\mu = 1) d\tilde{q}(\mu) \tag{6.25}$$

  thus it reflects how probable it is that the observed data is consistent with the $\mu = 1$ hypothesis given that $\mu = 1$ is true.

In addition, by convention, the following two quantities are defined:

- $CL_b = 1 - p_0^*$
- $CL_{s+b} = p_1$

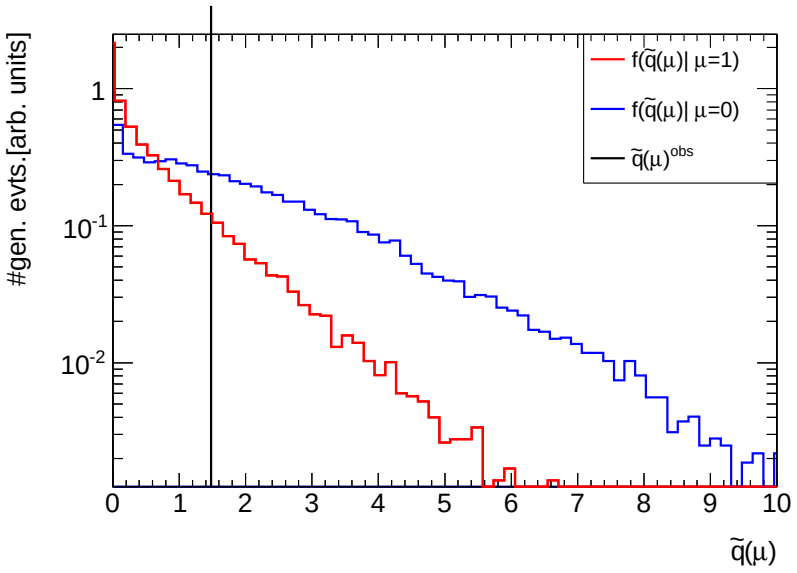

Figure 6.22: Distribution of the test statistic distribution $f(\tilde{q}(\mu))$ for $\mu = 0$ and $\mu = 1$ in SRC medium in the exclusion fit setup.

6.9.5.3 Is a model compatible with the data given the consistency of the background and the data?

In Ref. [126] an automated interpretation of hypothesis tests obtained by any test statistic T in case of limit setting was introduced, called "CL_s". In case of a large downward fluctuation of the observed data with respect to the estimated background the excluded parameter space on the non-SM signal is larger than the expected one. This is by principle no problem from the statistics point of view, but a (stronger) exclusion based on a statistical fluctuation does not seem to reflect the true value of the expected exclusion. The worst case scenario would be a signal hypothesis that is rejected due to a downward fluctuation of the data with respect to the background estimate in case there is no sensitivity to this signal hypothesis. Related to this issue is the possibility of having overestimated the background expectation, in this case it seems that the observed data is fluctuating downward, where it is not. To weaken or decrease the severity of these two points the CL_s interpretation was introduced which simply combines the information on the parameter of interest the signal strength with the largeness of the upward or downward fluctuation of data versus the expected amount of background events. The CL_s value is defined as

$$CL_s = \frac{CL_{s+b}}{CL_b} \tag{6.26}$$

In a strict statistical sense it translates any exclusion at a given confidence level (C.L.) on $T(\mu)$ into an exclusion at a confidence level on $T(\mu)$ 'weighted' by the confidence level on $T(0)$, thus one could call it a quality level on $T(\mu)$. The CL_s method is therefore an interpretation of the confidence level obtained on the signal strength. However in statistics conventions and in the following we keep the term confidence level on μ for simplicity albeit it means the quality level on μ stated above. The two points listed above giving rise to the introduction of the CL_s method are still present but much weakened, as they are suppressed by the CL_b value in Eq. 6.26.
When the CL_s-value of a measurement falls below a threshold value $CL_{s,thres}$ the signal hypothesis is rejected. In HEP physics this threshold is usually set to 0.05 or equivalently a Z_{thres} of 1.64.

The proper derivation of the CLs values in the unconditional regime is derived with the help of the approximation of CLs. The distribution of the expected approximated CLs-values is plotted in Fig. 6.23 and provides information on the expected sensitivity of the experiment and the uncertainty on this sensitivity is given by an uncertainty band corresponding to ± 1 "σ". This band is evaluated calculating the quantiles of the expected approximated CLs-value distribution. The probabilities to which the ± 1 σ quantiles belong are defined to be read of the cumulative distribution function of the normal (Gaussian) distribution (lower tail) at a value of ± 1. The median sensitivity is given at a CLs-value of 0.5 and the ± 1 σ values at 0.16 and 0.84, respectively.

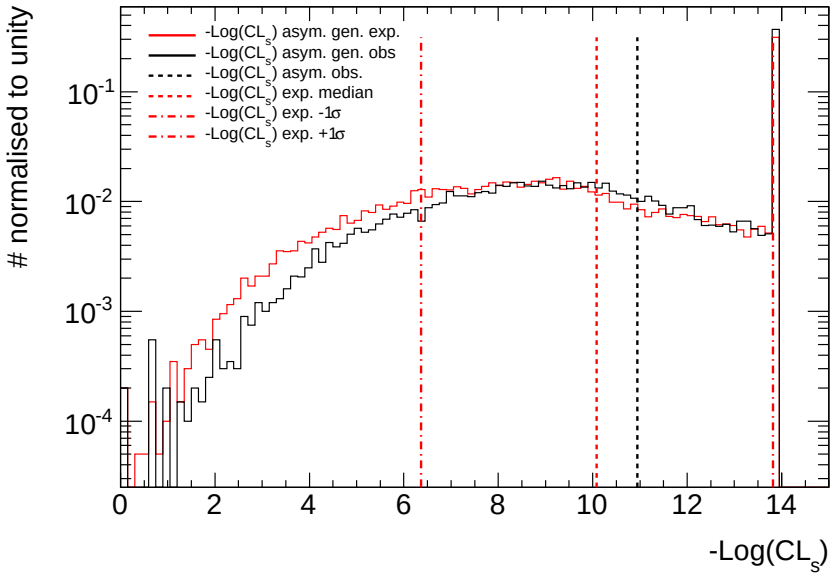

Figure 6.23: Distribution of approximate expected and observed CLs values in the unconditional ensemble. The cut-off at high sensitivity is due to numerical limitations.

6.10 Results

The estimated amount of background per channel is listed in Tab. 6.24 and opposed to the observed data. The statistical methods and tools described in the previous section are used to interpret the observed data. These numbers are obtained with the discovery fit setup, described in the previous section. The systematic and statistical uncertainties are factorized out. The background components are opposed to the estimation via MC normalized to luminosity. The non-SM signal strength is included in the fit to the data and after the fit it is removed (set to 0). The agreement or disagreement between the estimated background and the data is expressed in a p_0 value. As the SRs where the hypothesis test are carried out are not fully orthogonal only local p-values can be calculated. *No* disagreement between estimated background and data was observed. The largest deviation corresponding to a local p_0 of 0.016 occurred in SRC tight. This corresponds to a 2.1 sigma deviation in terms of Gaussian significance. In Fig. 6.24 the m_{eff} distributions of data are opposed to the background estimation from MC normalized to luminosity. In SRC a small turn on in the data can be seen at a m_{eff} value of $\sim 1.8\,\text{TeV}$. However the strength of the upward fluctuation is too small to indicate a disagreement between data and the estimated background.

The upper limit on Non-SM events is given as well in Tab. 6.24. These numbers are obtained in the exclusion mode, but with a generic non-SM signal, no uncertainties specific to the signal and no signal contamination in CRs. The non-SM signal is scanned from strength 0 up to the value where the CLs value falls below 0.05. The limit on the non-SM signal corresponds to a limit on the fiducial cross section, which is obtained simply by dividing the limit on the non-SM signal by the total integrated luminosity. This fiducial cross section can be compared to any non-SM signal, however the acceptance times efficiency of the non-SM signal has to be taken into account.

Process	Signal Region					
	SRC loose	SRE loose	SRA medium	SRAp medium	SRC medium	SRE medium
$t\bar{t}$+ Single Top	74 ± 12(sys) ± 7($stat$) (75)	73 ± 23(sys) ± 9.1($stat$) (68)	6.8 ± 4.4(sys) ± 1.8($stat$) (5.3)	11 ± 3.3(sys) ± 1.9($stat$) (10)	13 ± 4.3(sys) ± 2.2($stat$) (11)	19 ± 4.2(sys) ± 3.9($stat$) (15)
Z/γ+jets	71 ± 19(sys) ± 4.6($stat$) (78)	21 ± 6.3(sys) ± 2.4($stat$) (17)	32 ± 8.6(sys) ± 3.1($stat$) (44)	66 ± 17(sys) ± 4.6($stat$) (88)	16 ± 4.6(sys) ± 2.3($stat$) (20)	8.4 ± 2.7(sys) ± 1.7($stat$) (5.6)
W+jets	61 ± 9.9(sys) ± 5.9($stat$) (61)	23 ± 11(sys) ± 6.2($stat$) (23)	19 ± 3.6(sys) ± 2.9($stat$) (21)	25 ± 4.1(sys) ± 2.6($stat$) (30)	7.7 ± 2.5(sys) ± 1.7($stat$) (11)	6.2 ± 1.6(sys) ± 2.1($stat$) (4.7)
QCD jets	0.92 ± 1.1(sys) ± 0.18($stat$) (0.84)	8.4 ± 7.2(sys) ± 0.94($stat$) (25)	0.14 ± 0.2(sys) ± 0.15($stat$) (0.16)	0 ± 0.057(sys) ± 0.094($stat$) (0.52)	0.03 ± 0.04(sys) ± 0.021($stat$) (0.03)	1.4 ± 1.1(sys) ± 0.38($stat$) (2.7)
Di-Bosons	8 ± 4 (7.9)	4 ± 2 (4.2)	7 ± 4 (7.5)	14 ± 7 (16)	1.7 ± 0.9 (1.7)	3 ± 1 (2.7)
Total	214 ± 22.1(sys) ± 8.42($stat$)	129 ± 30.2(sys) ± 8.3($stat$)	65.4 ± 10.9(sys) ± 4.13($stat$)	116 ± 18.8(sys) ± 5.2($stat$)	39.3 ± 6.76(sys) ± 3.08($stat$)	37.8 ± 5.4(sys) ± 3.74($stat$)
Data	210	148	59	85	36	25
local p0 (Gaus. σ)	0.56(-0.15)	0.21(0.81)	0.66(-0.4)	0.9(-1.3)	0.61(-0.27)	0.87(-1.1)
UL on N_{BSM}	51(55^{42}_{76})	77(67^{49}_{91})	24(28^{20}_{39})	28(42^{31}_{58})	17(19^{14}_{26})	11(16^{12}_{23})
UL on CS /(fb)	11($12^{8.8}_{16}$)	16(14^{10}_{19})	5.1($5.9^{4.3}_{8.3}$)	6($8.9^{6.6}_{12}$)	3.6($4^{2.9}_{5.6}$)	2.2($3.4^{2.5}_{4.8}$)

Process	Signal Region				
	SRA tight	SRB tight	SRC tight	SRD tight	SRE tight
$t\bar{t}$+ Single Top	0.17 ± 0.21(sys) ± 0.059($stat$) (0.12)	0.25 ± 0.24(sys) ± 0.097($stat$) (0.2)	2 ± 1.4(sys) ± 0.59($stat$) (1.2)	2.4 ± 1.6(sys) ± 0.7($stat$) (1.4)	4.2 ± 4.5(sys) ± 1.3($stat$) (3)
Z/γ+jets	3.3 ± 1(sys) ± 1.1($stat$) (4)	2 ± 0.74(sys) ± 0.84($stat$) (2.1)	2 ± 0.67(sys) ± 0.68($stat$) (5.6)	0.93 ± 0.34(sys) ± 0.44($stat$) (3.4)	3.4 ± 1.2(sys) ± 1($stat$) (2.3)
W+jets	2.2 ± 0.67(sys) ± 0.72($stat$) (1.9)	0.98 ± 0.46(sys) ± 0.37($stat$) (0.84)	1.5 ± 1.1(sys) ± 0.71($stat$) (2.7)	2.4 ± 0.95(sys) ± 1($stat$) (2.5)	2.8 ± 1.6(sys) ± 0.97($stat$) (1.5)
QCD jets	0 ± 0.014(sys) ± 0.0084($stat$) (0.0095)	0 ± 0.06(sys) ± 0.032($stat$) (0.021)	0 ± 0.021(sys) ± 0.015($stat$) (0.005)	0 ± 0.22(sys) ± 0.18($stat$) (0.093)	0.46 ± 0.37(sys) ± 0.23($stat$) (0.85)
Di-Bosons	1.8 ± 0.9 (2)	1.8 ± 0.9 (1.9)	0.5 ± 0.3 (0.51)	2 ± 1 (2.2)	3 ± 1 (2.5)
Total	7.38 ± 1.86(sys) ± 1.26($stat$)	5 ± 1.67(sys) ± 0.906($stat$)	5.98 ± 2.02(sys) ± 0.978($stat$)	7.82 ± 2.42(sys) ± 0.969($stat$)	13.3 ± 6.26(sys) ± 1.59($stat$)
Data	1	1	14	9	13
local p0 (Gaus. σ)	0.98(-2.1)	0.96(-1.7)	0.016(2.1)	0.29(0.55)	0.45(0.14)
UL on N_{BSM}	3.1($6.4^{4.5}_{9.4}$)	3($5.6^{3.9}_{8.3}$)	16($9.5^{6.9}_{14}$)	9.6($8.5^{6.1}_{12}$)	12($12^{8.4}_{17}$)
UL on CS /(fb)	0.66($1.4^{0.96}_{2}$)	0.64($1.2^{0.83}_{1.8}$)	3.4($2^{1.5}_{2.9}$)	2($1.8^{1.3}_{2.6}$)	2.5($2.5^{1.8}_{3.5}$)

Table 6.24: Fitted background components in each SR, compared with observation. The estimated background values are quoted in the order *expectation ± systematic uncertainty ± statistical uncertainty (pre-fit prediction)*. For the total background estimates, the two quoted uncertainties are, respectively, systematic and statistical. The values in parentheses correspond to the MC estimate normalised to cross section times luminosity without any further scaling. For W+jets, Z+jets and $t\bar{t}$+jets,these predictions are scaled using results from the dedicated fits described in Section efsubsec:evselresul. Observed limits on the model independent cross section at 95% C.L. based on CLs, no signal uncertainties are taken into account. The observed cross section and the expected ones given a $\pm 1\sigma$ deviation in the background are given in brackets.

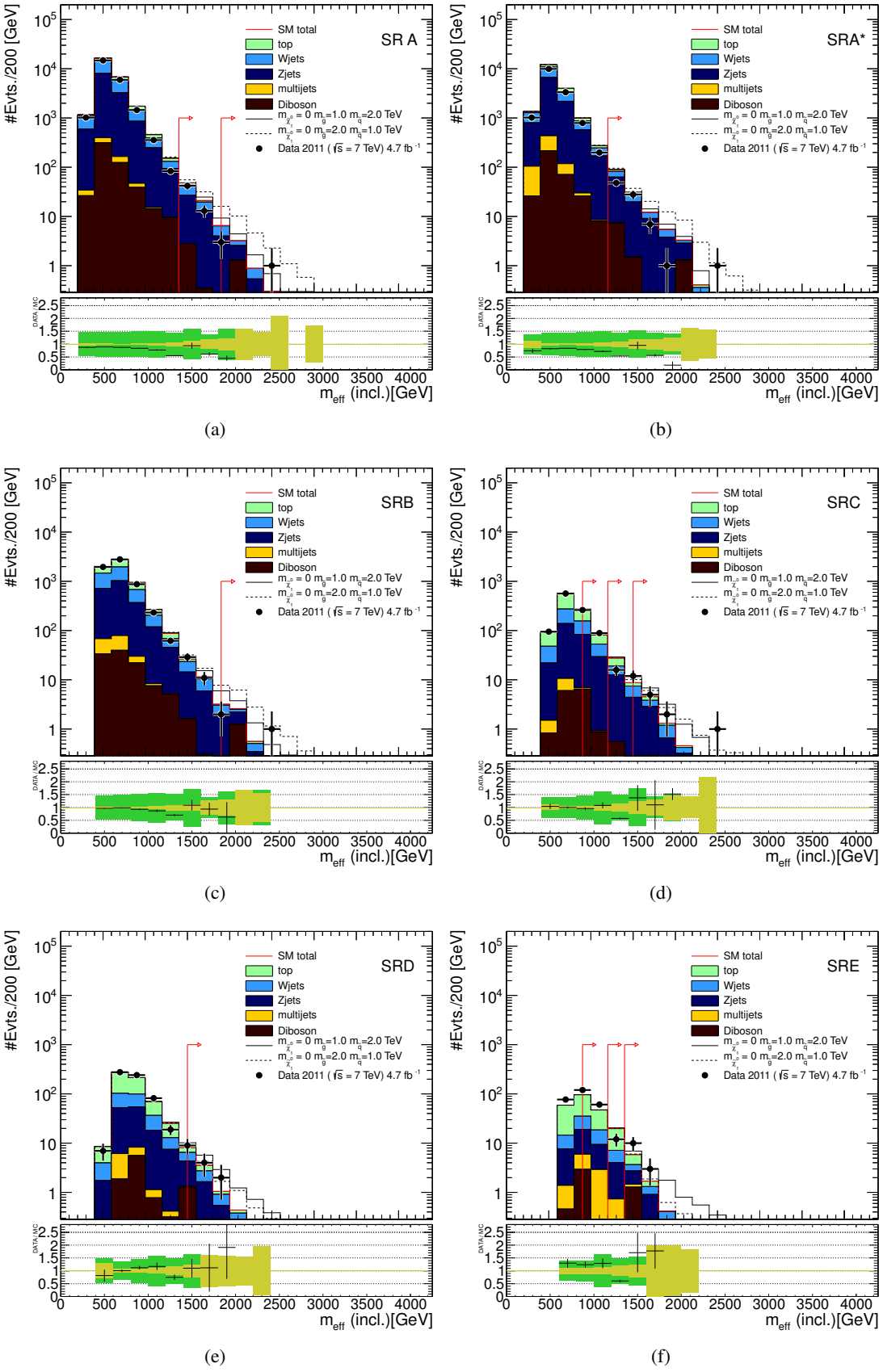

Figure 6.24: $meff$ (incl.) distributions of all search channels A-E. Each top panel shows the SM background expectations. MC simulation expectations are normalized to luminosity. The multi-jet background is estimated using the jet smearing method described in the text. Two benchmark model points with m($\tilde{\chi}^0$) =0 TeV, m($\tilde{q}$)=1.0 TeV, m($\tilde{g}$)=2.0 TeV and m($\tilde{\chi}^0$) =0 TeV, m($\tilde{q}$)=2.0 TeV, m($\tilde{g}$)=1.0 TeV, respectively. The arrows indicate the locations of the lower edges of the signal regions. The bottom panel shows the fractional deviation of the data from the total unscaled background estimate. The light (yellow) band shows the combined experimental uncertainties on the unscaled background estimates from jet energy scale, jet energy resolution, the effect of pile-up, the treatment of energy outside of reconstructed jets and MC simulation sample size. The medium (green) band includes also the total theoretical uncertainties.

Uncertainty	Relative to total(aver.)/%
MCSR	44
acc. Z+jets/γ	39
CR stats.	39
Top theory	34
JES	18
Generic Diboson	17
W+jets theory	15
CR3 MC stat.	12
CR2 MC stat.	9.6
PDF	9.4
b-tag/veto eff.	8.1
CR4 MC stat.	6
CR1b MC stat.	5.4
JER	5.4
QCD smear.	5.1
lepton resoln.	4.8
Pileup	3.2
MET CellOut cluster	3.1
Lumi	2.9
lepton scale.	2.7
leptoneff.	2.2
Trigger	1.6
MET CellOut pileup	1.4

Table 6.25: Averaged uncertainties over all 11 signal regions, the numbers shown correspond to the relative amount per component in percent to the total uncertainty .

6.11 Discussion of uncertainties

To digest the impact of uncertainties the averaged uncertainties relative to the total are listed in percent in Tab. 6.25. However this quantity can only give a very rough estimation of the impact of the various sources of uncertainties on the analyses as the relative contribution to the total uncertainty does vary over a broad range as can be seen in Tab. 6.27 where the uncertainties per channel are listed. The most important uncertainties are:

- 'MCSR' corresponds to a term including all statistical uncertainties from limited MC sample sizes in the SR.
- 'acc. Z+jets/γ' is the uncertainty associated to the interpolation from the photon CR to the SR to estimate Z+jets.
- 'CRstat' is the term including all statistical uncertainties associated to the observed data in the CRs.

Uncertainty	Relative to total/%
JES	77
CR stat.	43
CR stat.	24
PDF	23
MCSR	19
Diboson	19
acc. Z+jets/γ	14

Table 6.26: Relative amount per component in percent to the total uncertainty in channel SR E tight, shown are only contributions with > 10%.

- 'Top theory' and 'W+jets theory' is the uncertainty associated to $t\bar{t}$ and W+jets MC modelling, that is renormalisaion and factorization scale variations and a term corresponding to extra parton radiation.
- 'JES' corresponds to the uncertainty of the jet energy scale calibration.
- 'Generic Diboson' corresponds to the uncertainty in the MC modelling of the Diboson processes.
- 'CRX MC stat.' are the statistical uncertainties from limited MC sample size in CRX.
- 'JER' is the uncertainty of jet energy resolution.
- 'PDF' is the uncertainty associated to PDF choices.

Typical examples are SRC loose/medium/tight, here the relative 'MCSR' uncertainty takes the values (36/45/51) % and the 'CR stats.' (38/42/43) %. The 'acc. Z+jets/γ' is (76/55/22)%, thus dominates in the loose region and decreases in importance to the total uncertainty. Opposed to this the relative importance of the 'top theory' and 'W+jets theory' uncertainty increases from loose to tight with (27/49/56) % and (16/23/37)%. The 'JES' uncertainty is sub-dominant (<10/15/<10)% as well as 'CR3 MC stat' with (<10/<10/13) %. All other uncertainties contribute with a relative uncertainty of <10 %.
The largest deviation from the average values show SRE loose and SRE tight. In the approach of measuring the contributions of processes as well as their uncertainties relative to CRs a likelihood contour with several local minima can occur. Then the finding of the global minimum of the likelihood could not 100% ensured. Therefore the JES uncertainty is not taken relative to the CR, but rather applied independently in the SR and CR. This approach is conservative in respect to discovery and limit setting and pushed the 'JES' to be the dominant uncertainty. The relative importance in % to the total uncertainty in SRE tight is shown in Tab. 6.26. For completeness the breakdown of all factorized uncertainties is listed in Tab. 6.27 as well as their relative impact in Tab. 6.28

Uncertainty	Signal Region										
	SRA medium	SRA tight	SRAp medium	SRB tight	SRC loose	SRC medium	SRC tight	SRD tight	SRE loose	SRE medium	SRE tight
Total	11	2.2	19	2	22	7.3	2.2	2.6	31	7.2	6.4
CR stat.	4.1	1.1	5	0.97	8.3	3	0.98	0.98	8.3	3.7	1.6
CR2 MC stat.	0.48	0.52	0	0.35	0	0.1	0	0.29	0	3.1	0.22
CR4 MC stat.	0.78	0	0	0	0	0.86	0.1	0.048	0	1.9	0.88
CR3 MC stat.	1.3	0.19	2	0.085	0	0.66	0.29	0.33	0.94	3.1	0.68
CR1b MC stat.	1.1	0	4.5	0	0	0.77	0.16	0.21	0	0	0
MCSR	4.3	1.5	7.1	1.4	6.4	3	1.1	1.6	1.1	4.3	1.2
b-tag/veto eff.	1.2	0.046	4.3	0.032	0	0	0	0.19	0	3.1	0
MET CellOut cluster	0.14	0.061	0	0.051	0	0.27	0.047	0.076	3.6	0.17	0.29
Generic Diboson	2.5	0.52	6.1	0.55	0	0.69	0	0.97	1.4	0.85	1.2
JER	0	0.16	1.4	0	0	0.68	0.17	0	4.6	0.85	0
JES	0	0.074	3.4	0.055	0	1.1	0	0	24	0	4.9
ℓ eff.	0.24	0.032	0	0.032	0.77	0.19	0.032	0.032	0	0.14	0.57
ℓ resoln.	0.27	0.032	4.3	0.032	0.6	0.23	0	0.2	2.4	0.19	0
ℓ scale.	0.35	0.032	1.4	0.032	0.8	0.23	0	0	0	0.19	0.37
Trigger	0.13	0.032	0.44	0.032	0.67	0.13	0.032	0.032	0	0.26	0
PDF	0	0	4.2	0.098	1.6	0	0	0.18	0	2.8	1.5
MET CellOut pileup	0.27	0	0	0.05	0.32	0.23	0	0.032	0.86	0.12	0
Pileup	0.55	0.032	0.69	0.045	0.59	0.72	0.09	0.15	0	0	0
QCD smear.	0.11	0.032	1.4	0.032	0	0.21	0	0.032	6	1	0.41
W+jets theory	1.5	0.16	1.6	0.27	3.6	1.7	0.83	0.31	4.4	0.76	0.25
acc. Z+jets/γ	7.6	0.63	16	0.55	17	4	0.5	0	6.8	2.3	0.91
Lumi	0	0.043	0.35	0.033	0	0.55	0.032	0	2.3	0.2	0.46
Top theory	4	0.13	2.4	0.18	6	3.6	1.3	1.4	11	3.1	2.7

Table 6.27: Breakdown of influence of systematic uncertainties in the signal regions. Total is the full uncertainty; CR stat. is the uncertainty with all uncertainties apart from the statistical uncertainty in the CRs switched off; MC stat. is the uncertainty coming from limited MC sample sizes. All other entries show the influence of the corresponding systematic uncertainty which was obtained switching of only the particular uncertainty and quadratically subtract the result from the total. MC stat. uncertainties are modelled with a Poisson pdf shape, CR stat. uncertainties using Poisson pdf distributions. All other uncertainties are modelled via a piece-wise interpolation taking into account asymmetric variation in the input distributions. Note: the influence of MC stat. and all systematic uncertainties was obtained using quadratic subtraction, which assumes a Gaussian shape for all underlying probability density functions, this is not fully correct, but give a good estimate on which are the dominant uncertainties.

Uncertainty	Signal Region										
	SRA medium	SRA tight	SRAp medium	SRB tight	SRC loose	SRC medium	SRC tight	SRD tight	SRE loose	SRE medium	SRE tight
Total	1e+02	1e+02	1e+02	1e+02	1e+02	1e+02	1e+02	1e+02	1e+02	1e+02	1e+02
CR stat. /%	37	52	27	48	38	42	43	37	27	52	24
CR2 MC stat. /%	0.1	3	0	1.6	0	0.01	0	0.6	0	10	0.06
CR4 MC stat. /%	0.25	0	0	0	0	0.71	0.1	0.02	0	3.7	0.94
CR3 MC stat. /%	0.73	0.39	0.59	0.09	0	0.41	0.85	0.78	0.05	9.7	0.56
CR1b MC stat. /%	0.52	0	3	0	0	0.57	0.24	0.31	0	0	0
MCSR /%	7.9	28	7.5	31	4.4	9	13	21	0.06	20	1.9
b-tag/veto eff. /%	0.6	0.02	2.7	0	0	0	0	0.26	0	10	0
MET CellOut cluster /%	0.01	0.04	0	0.03	0	0.07	0.02	0.04	0.69	0.03	0.1
Generic Diboson /%	2.6	2.9	5.5	3.8	0	0.46	0	7.2	0.1	0.71	1.8
JER /%	0	0.29	0.28	0	0	0.45	0.3	0	1.1	0.71	0
JES /%	0	0.06	1.7	0.04	0	1.1	0	0	36	0	36
ℓ eff. /%	0.02	0	0	0	0.06	0.03	0.01	0	0	0.02	0.39
ℓ resoln. /%	0.03	0	2.6	0	0.04	0.05	0	0.31	0.31	0.04	0
ℓ scale. /%	0.05	0	0.3	0	0.07	0.05	0	0	0	0.04	0.17
Trigger /%	0.01	0	0.03	0	0.05	0.02	0	0	0	0.06	0
PDF /%	0	0	2.6	0.12	0.26	0	0	0.24	0	8	2.6
MET CellOut pileup /%	0.03	0	0	0.03	0.01	0.05	0	0.01	0.04	0.01	0
Pileup /%	0.13	0	0.07	0.03	0.04	0.49	0.08	0.17	0	0	0
QCD smear. /%	0.01	0	0.3	0	0	0.04	0	0	1.9	0.98	0.21
W+jets theory /%	0.98	0.29	0.36	0.91	1.3	2.7	7.1	0.71	1	0.57	0.08
acc. Z+jets/γ /%	28	4.4	46	3.8	35	16	2.5	0	2.5	5.2	1
Lumi /%	0	0.02	0.02	0.01	0	0.29	0	0	0.28	0.04	0.26
Top theory /%	6.8	0.17	0.84	0.39	3.8	13	17	15	6.8	9.7	9.5

Table 6.28: Breakdown of influence of systematic uncertainties in the signal regions. Quoted are the relative uncertainties. The entries are the same as in Tab. 6.27.

6.12 Impact on supersymmetric models

As there was no disagreement between data and the estimated background in the signal regions found, the impact on SUSY model parameters has been investigated. This analysis is dedicated to the strong production modes $\tilde{q}\tilde{q}$, $\tilde{q}\tilde{q}*$, $\tilde{q}\tilde{g}$ and $\tilde{g}\tilde{g}$. Only the first two generation of squarks ($\tilde{q} \in \tilde{u}, \tilde{d}, \tilde{c}, \tilde{s}$) are considered if not stated otherwise. The interpretation is split into several models. The single production modes and possible decay scenarios including one more intermediate particle are interpreted in Sec. 6.12.2 and Sec. 6.12.3. All production modes are considered in a simplified scenario in Sec. 6.12.1 where only the direct decay to the neutralino ($\tilde{\chi}^0$) is allowed. A model considering a proper supersymmetry breaking mechanism with assumptions on the supersymmetry breaking parameters is the CMSSM which is interpreted in Sec. 6.12.4. A CMSSM-based compressed scenario with all particles of the MSSM involved as potential intermediate particles is discussed in Sec. 6.12.5.

For a given model point the amount of signal expected in the SRs and CRs can be calculated from MC normalized to luminosity. This information is fed to the exclusion fit setup. A CLs value is calculated for each model point as described in Sec. 6.9.5.3. As there are 11 SRs which different sensitivity per model point, the region with the best *expected* sensitivity per model point is chosen. That is the SR with the lowest expected CLs value. Theoretical uncertainties on the signal are taken into account in calculating the $\pm 1\sigma$ observed CLs values, giving the $\pm 1\sigma$ fluctuation from the uncertainty on the cross section calculations. Limits on model parameters or masses are given at the level of $+1\sigma$ of the theoretical uncertainty on the signal.

The spectra of SUSY signal samples are generated with Herwig++ [87,88] or with MadGraph/PYTHIA6 [89, 90]. The SUSY signal cross section and their uncertainty are calculated following as close as possible the PDF4LHC [81] recommendations as described in Ref. [82], i.e. the mean of the envelope from several PDF sets as nominal signal cross section and the uncertainty form the global envelope. In these calculations two pdf sets were used, CTEQ6L1 and MRST2007LO*. The cross sections are calculated up to next-to-leading order in α_S, including the re-summation of soft gluon emission at next-to-leading-logarithmic accuracy (NLO+NLL) [75–79]. The nominal cross-section is defined as:

$$\sigma_{\text{nominal}} = 0.5 \times \left[\max(\sigma^{+}_{\text{CTEQ}}, \sigma^{+}_{\text{MSTW}}) + \min(\sigma^{-}_{\text{CTEQ}}, \sigma^{-}_{\text{MSTW}})\right], \tag{6.27}$$

$\sigma^{\pm}_{\text{CTEQ/MSTW}}$ is the uncertainty on the cross-section. The uncertainty envelope for the MSTW PDFs is obtained by varying the PDFs and the renormalisaion and factorization scale with the central value obtained by the MSTW PDF set. The same is done for the CTEQ pdf, but in addition the strong coupling constant α_S is varied. The signal expectation at $\pm 1\sigma$ are fed to the likelihood and the same hypothesis test procedure is carried out as for the nominal cross section.

6.12.1 Simplified Models I

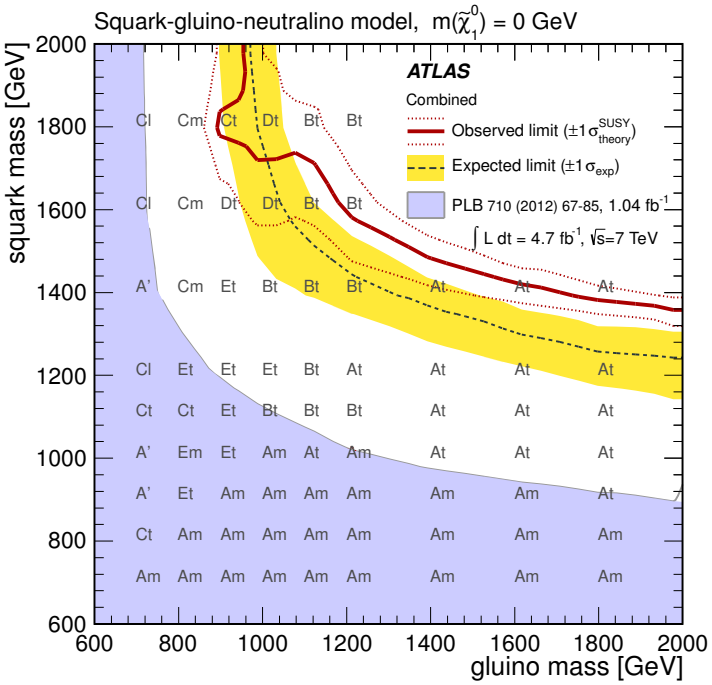

Figure 6.25: $\tilde{q}\tilde{q}$, $\tilde{q}\tilde{q}*$, $\tilde{q}\tilde{g}$ and $\tilde{g}\tilde{g}$ decaying directly to a massless LSP.

In Fig. 6.25 the interpretation in a model where the strongly produced particles via $\tilde{q}\tilde{q}$, $\tilde{q}\tilde{q}*$, $\tilde{q}\tilde{g}$ and $\tilde{g}\tilde{g}$ decay directly to a massless LSP. This is enforced by setting all other super-particles masses to very high values, so that they are kinematically not accessible. The limits are expressed in terms of the gluino mass $m_{\tilde{g}}$ and the squark masses of the first two generations $m_{\tilde{q}}$. For each model point the exclusion sensitivity is calculated and the best expected SR is chosen per model point. The best expected model point corresponds to the one with the lowest expected $CL_{s,exp}$ value. The label on the plots ranging from A-E and the suffixes 'l','m' and 't' stand for loose, medium and tight. In region where squark-squark production is dominant regions with low jet multiplicities are most sensitive, whereas in region where gluino-gluino production is dominant higher jet multiplicity channels take over. The red solid line corresponds to the combined observed limit based on the formalism explained in Sec. 6.9.5. the dotted lines are obtained by scaling the cross-section up/down by the theoretical uncertainty. The black dashed line shows the expected limit at 95% C.L., with the yellow band indicating the 1σ experimental uncertainties. In addition the analysis corresponding to ~ 1 fb^{-1} at 7 TeV is shown in shaded gray. Note that e.g. in SR A tight a fluctuation of the data below the estimated background was observed, thus the observed limit is better than the expected one, even outside the yellow band. In this scenario the limit on the gluino mass is approximately 860 GeV, and that on the squark mass is 1320 GeV. Squarks and gluinos with equal masses below 1410 GeV are excluded.

The same model but with a massive LSP is interpreted in Fig. 6.26. The LSP masses are set to 195 GeV and 395 GeV, respectively. These exclusion limits do degrade with increasing LSP mass, but not too much, as can be seen as well in Fig 6.27, where the exclusion curves for LSP masses for 0,195 and

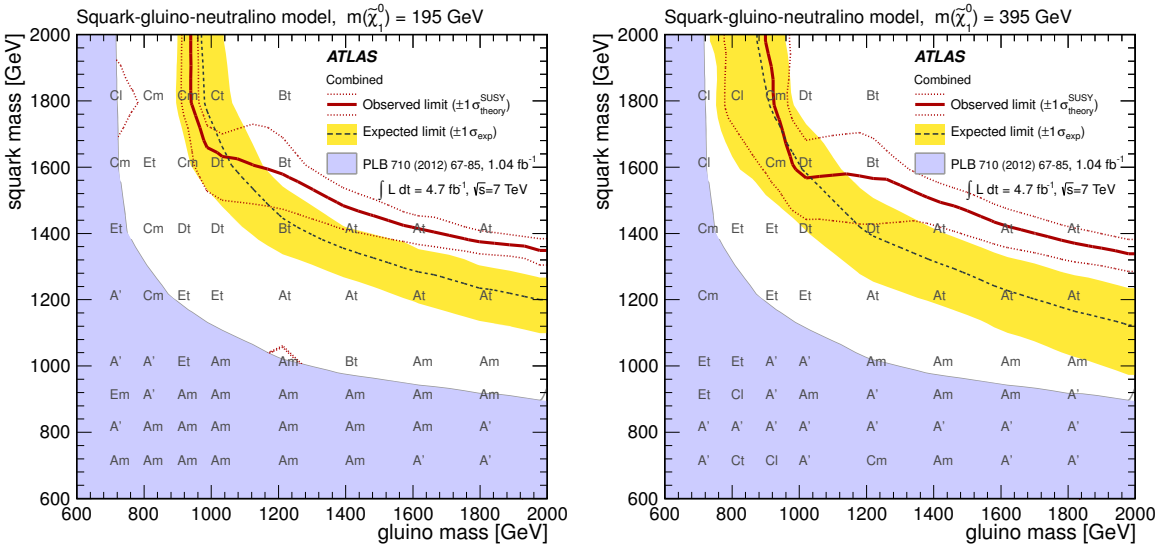

Figure 6.26: $\tilde{q}\tilde{q}$, $\tilde{q}\tilde{q}*$, $\tilde{q}\tilde{g}$ and $\tilde{g}\tilde{g}$ decaying directly to a massive LSP with 195 GeV and 395 GeV, respectively.

395 GeV are overlaid. When the LSP mass is 395 GeV the squark and gluino limit degrade up to a difference of ~ 200 GeV compared to the massless case.

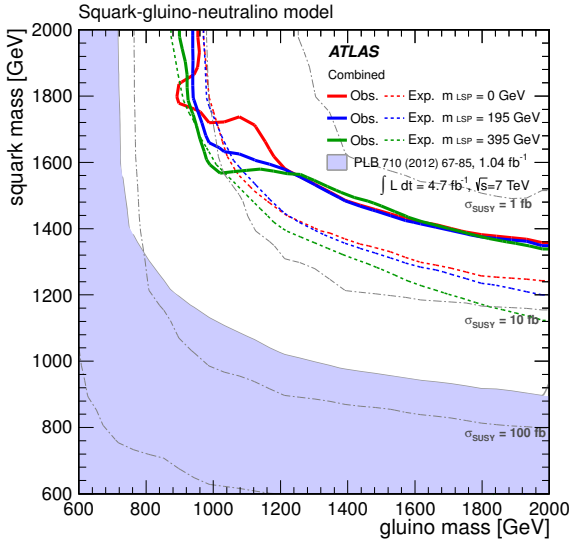

Figure 6.27: $\tilde{q}\tilde{q}$, $\tilde{q}\tilde{q}*$, $\tilde{q}\tilde{g}$ and $\tilde{g}\tilde{g}$ decaying directly to a massive LSP with 0,195 and 395 GeV respectively, overlaid.

6.12.2 Simplified Models II

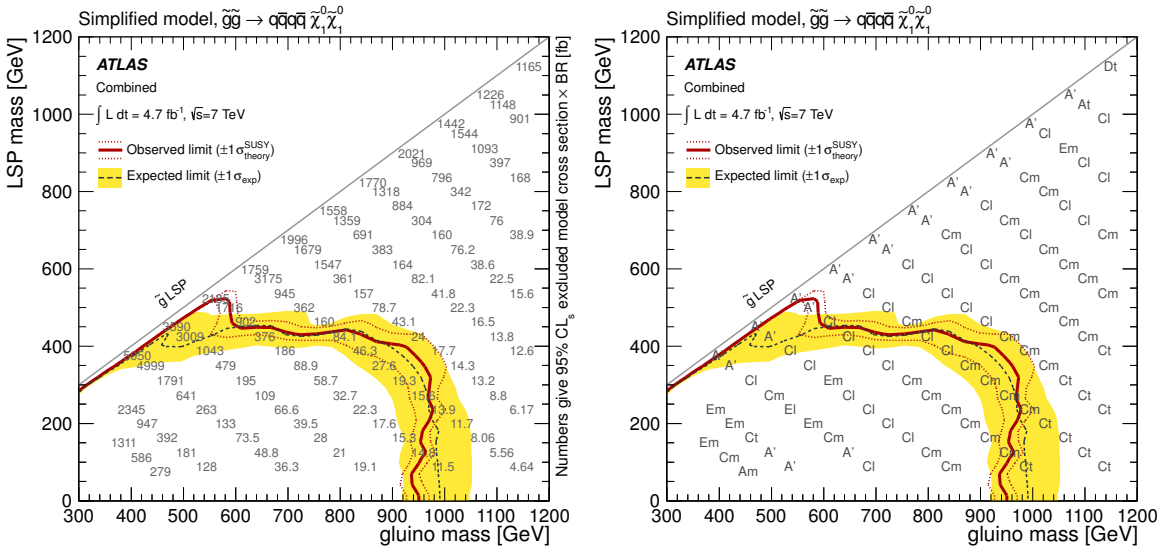

Figure 6.28: Direct production of gluino-gluino pairs each decaying to two jets and a neutralino LSP.

The model in Fig. 6.28 assumes only pair production of gluinos. As before the gluinos are forced to decay directly to the LSP and two jets. Gluino masses of $\sim 920\,\text{GeV}$ are excluded up to LSP masses of $\sim 400\,\text{GeV}$. The most sensitive region is SR C containing four and more jets. In the left plot the upper limit on the cross section times acceptance times efficiency UL_σ is plotted for each model point. It is calculated as follows:

$$UL_\sigma = \frac{UL_N}{acc. \times eff. \times L_{int}} \tag{6.28}$$

UL_N is the upper limit on the non-SM events calculated in the exclusion fit setup. $acc. \times eff.$ is the relative amount of signal passing all selection cuts to the SR and L_{int} is the total integrated luminosity. The model in Fig. 6.29 assumes only pair production of squarks and anti-squarks of the first two generations ($\tilde{u}, \tilde{d}, \tilde{c}, \tilde{s}$ and $\tilde{u}*, \tilde{d}*, \tilde{c}*, \tilde{s}*$). Squark masses of $\sim 700\,\text{GeV}$ are excluded up to LSP masses of $\sim 250\,\text{GeV}$.

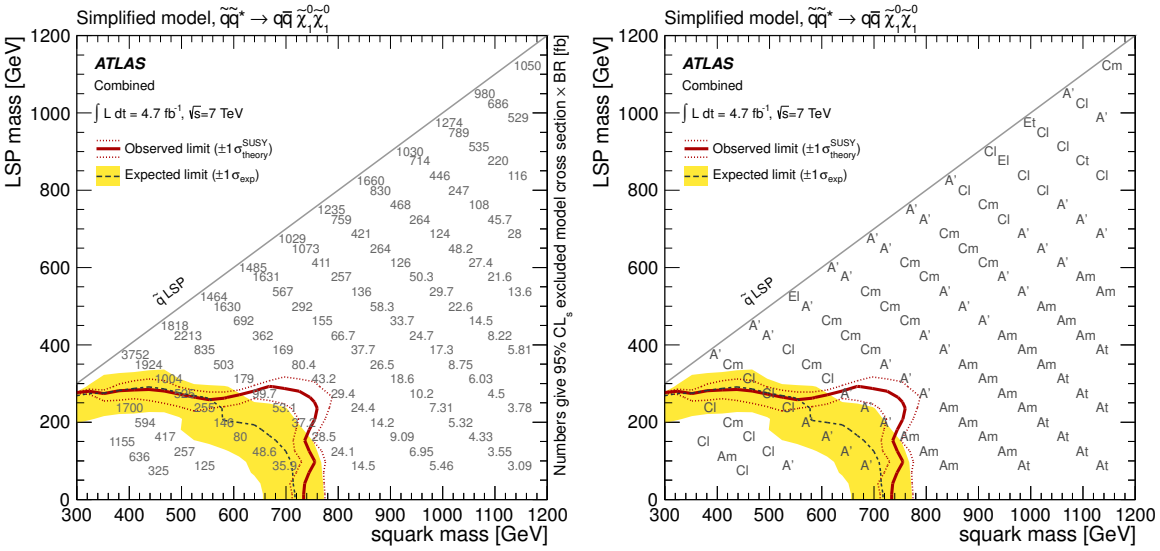

Figure 6.29: Direct production of squark-anti-squark pairs decaying to one jet, resp., and a neutralino LSP.

6.12.3 Simplified Models III

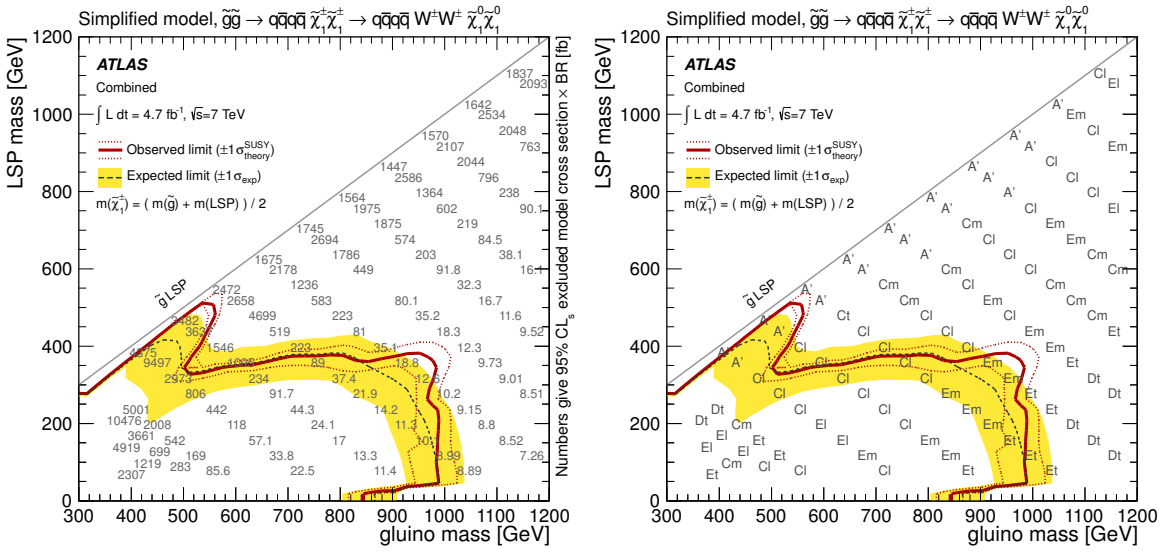

Figure 6.30: Combined exclusion limits for direct production of gluino pairs, each decaying via an intermediate chargino to two jets, a W boson and a neutralino LSP. The chargino mass is fixed halfway in between the gluino and LSP masses.

The model interpreted in Fig. 6.30 assumes only pair production of gluinos. But in contrast to the models described above an intermediate particle is kinematically accessible, the chargino. The mass of the chargino is set to be exactly in the middle of the gluino mass and the LSP mass. The gluinos decay via an intermediate chargino to two jets, a W boson and a neutralino LSP. Thus the phenomenology is in that way different that more jets are produced with a softer spectrum. In addition leptons can be produced. The most sensitive region is SR E containing 6 and more jets, compared to the direct decay modes where a region with four and more jets is most sensitive.
In Fig. 6.31 the chargino mass is fixed to 60 GeV. The y-axis is defined as the ratio of the mass difference of the chargino and the LSP to the mass difference of the chargino to the gluino.

The model interpreted in Fig. 6.32 assumes again only pair production of squarks and anti-squarks. The chargino is kinematically accessible, too. The mass of the chargino is set to be exactly in the middle of the squark mass and the LSP mass. In this scenario only left-handed squarks are considered in order to enhance the branching ratios of decay chains incorporating an intermediate chargino. The cross sections have been reduced by 50 % to take this situation properly into account. The squarks decay via an intermediate chargino to two jets, a W boson and a neutralino LSP. Thus the phenomenology is in that way different that more jets are produced with a softer spectrum. In addition leptons can be produced.
In Fig. 6.33 the chargino mass is fixed to 60 GeV. The y-axis is defined as the ratio of the mass difference of the chargino and the LSP to the mass difference of the chargino to the squarks.

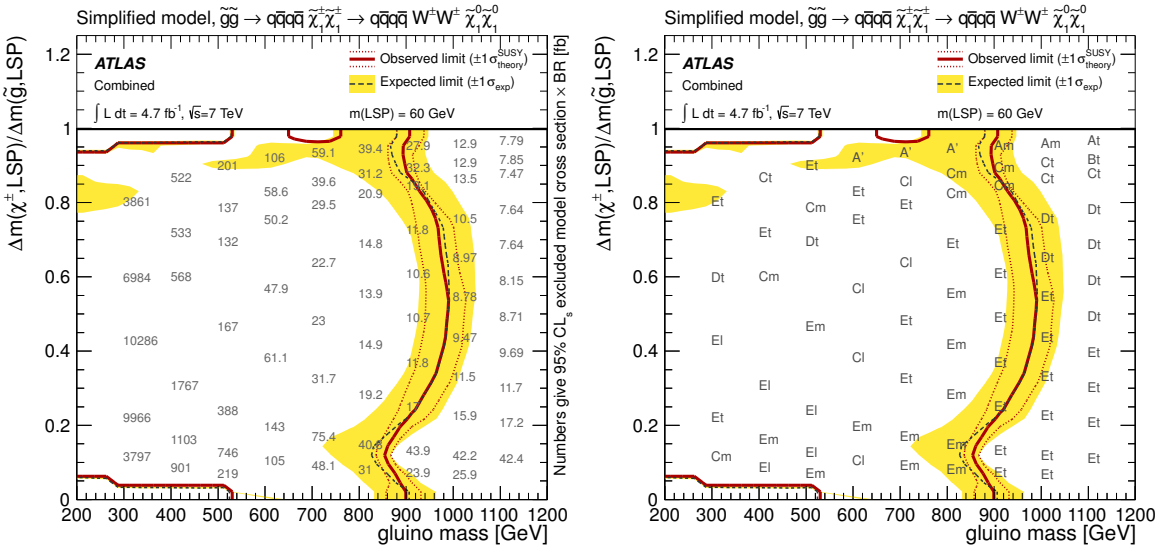

Figure 6.31: Combined exclusion limits for direct production of gluino pairs, each decaying via an intermediate chargino to two jets, a W boson and a neutralino LSP. The chargino mass is fixed to 60 GeV.

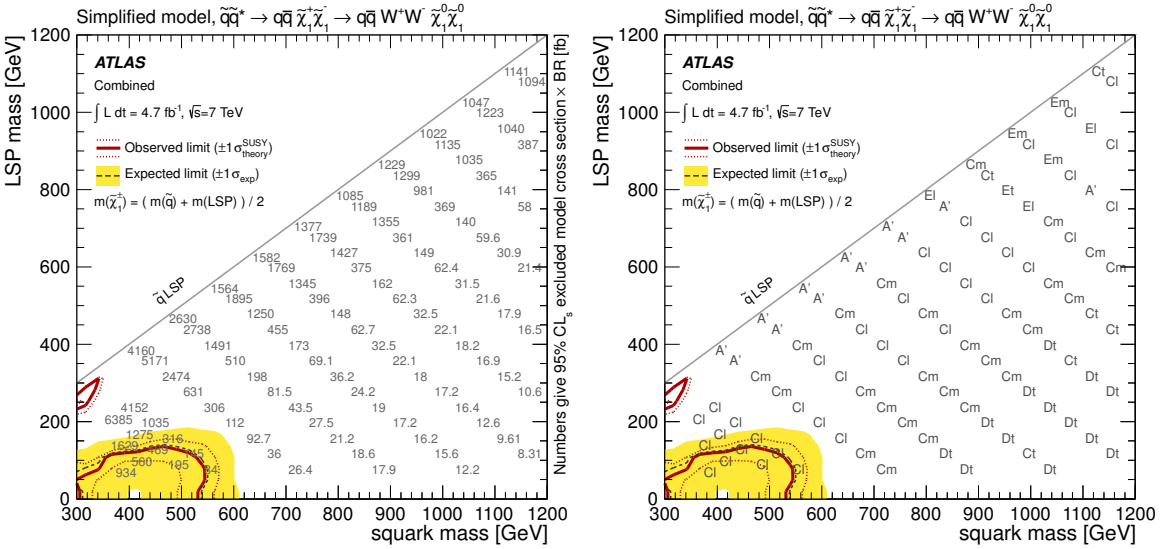

Figure 6.32: Combined exclusion limits for direct production of squark pairs, each decaying via an intermediate chargino to two jets, a W boson and a neutralino LSP. The chargino mass is fixed halfway in between the gluino and LSP masses.

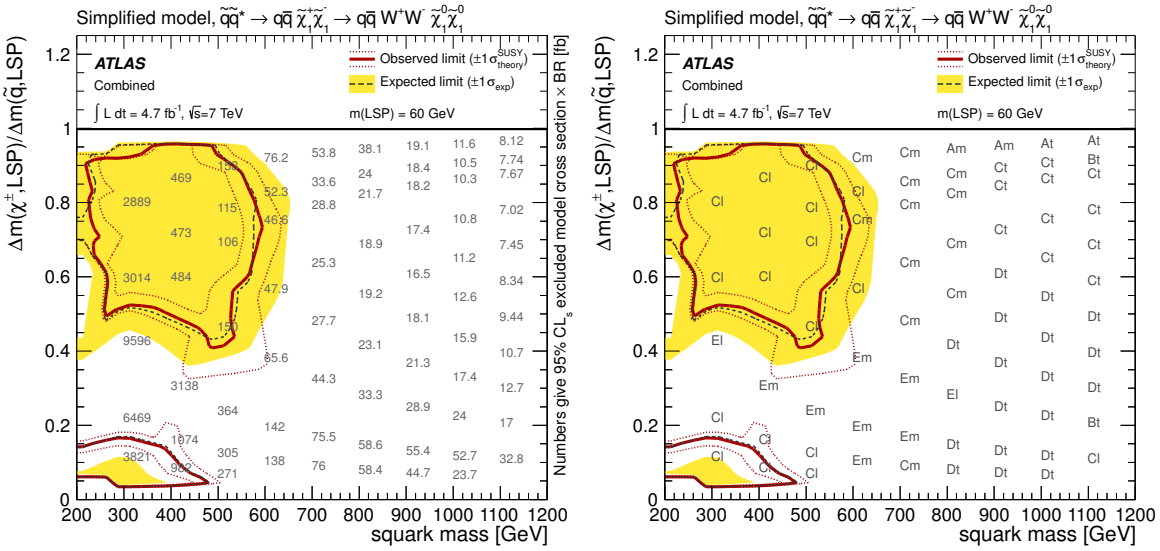

Figure 6.33: Combined exclusion limits for direct production of squark pairs, each decaying via an intermediate chargino to two jets, a W boson and a neutralino LSP. The chargino mass is fixed to 60 GeV.

6.12.4 CMSSM

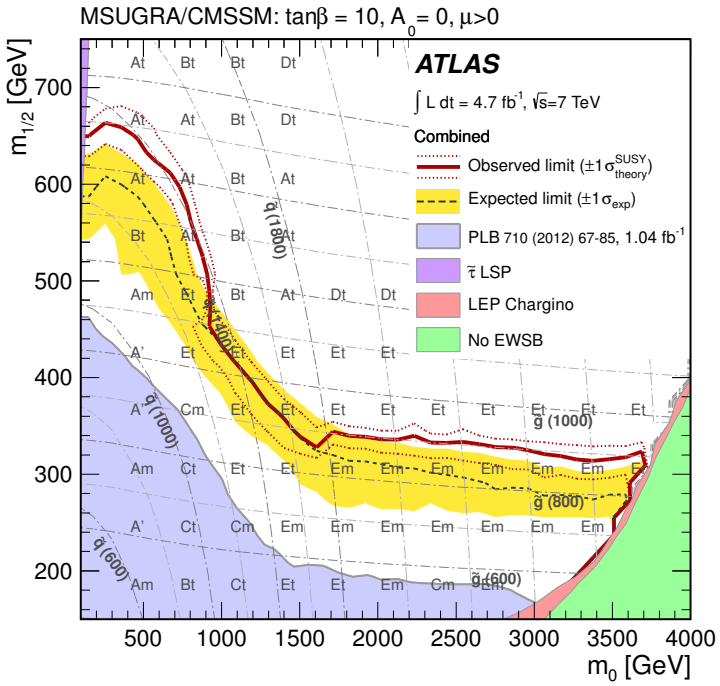

Figure 6.34: CMSSM model with $tan(\beta) = 10$, $A_0 = 0$, $\mu > 0$.

In Fig. 6.34 the interpretation in the CMSSM is shown for a specific model parameters set of $tan(\beta) = 10$, $A_0 = 0$, $\mu > 0$ in the m_0-$m_{1/2}$ plane. In the CMSSM a relation on the minimal squark mass $m_{\tilde{q}}$ relative to the gluino mass $m_{\tilde{g}}$ exists. In Ref. [132] it is shown that the the ratio $m_{\tilde{q}}/m_{\tilde{g}}$ barely exceeds 0.9 with $m_{\tilde{q}}$ being the average of the first two generations. The limit on $m_{1/2}$ reaches 300 GeV at high m_0 and 640 GeV for low values of m_0 . At equal masses squarks and gluinos with masses below 1360 GeV are excluded.

6.12.5 Compressed Models

A CMSSM-like model with increased compression was proposed in Ref. [91, 92] and is interpreted in Fig. 6.35. All supersymmetric particles are involved in the phenomenology, but their distance in mass to each other is controlled by a compression factor c. The squark mass is set to 96% of the gluino mass. Three types of models with different assumption on the kinematically accessible particles are shown. In the top left plot all squarks, electroweak gauginos and the gluino are kinematically accessible. In the top right the neutralinos and charginos are not accessible and in the bottom plot the squarks are not accessible.

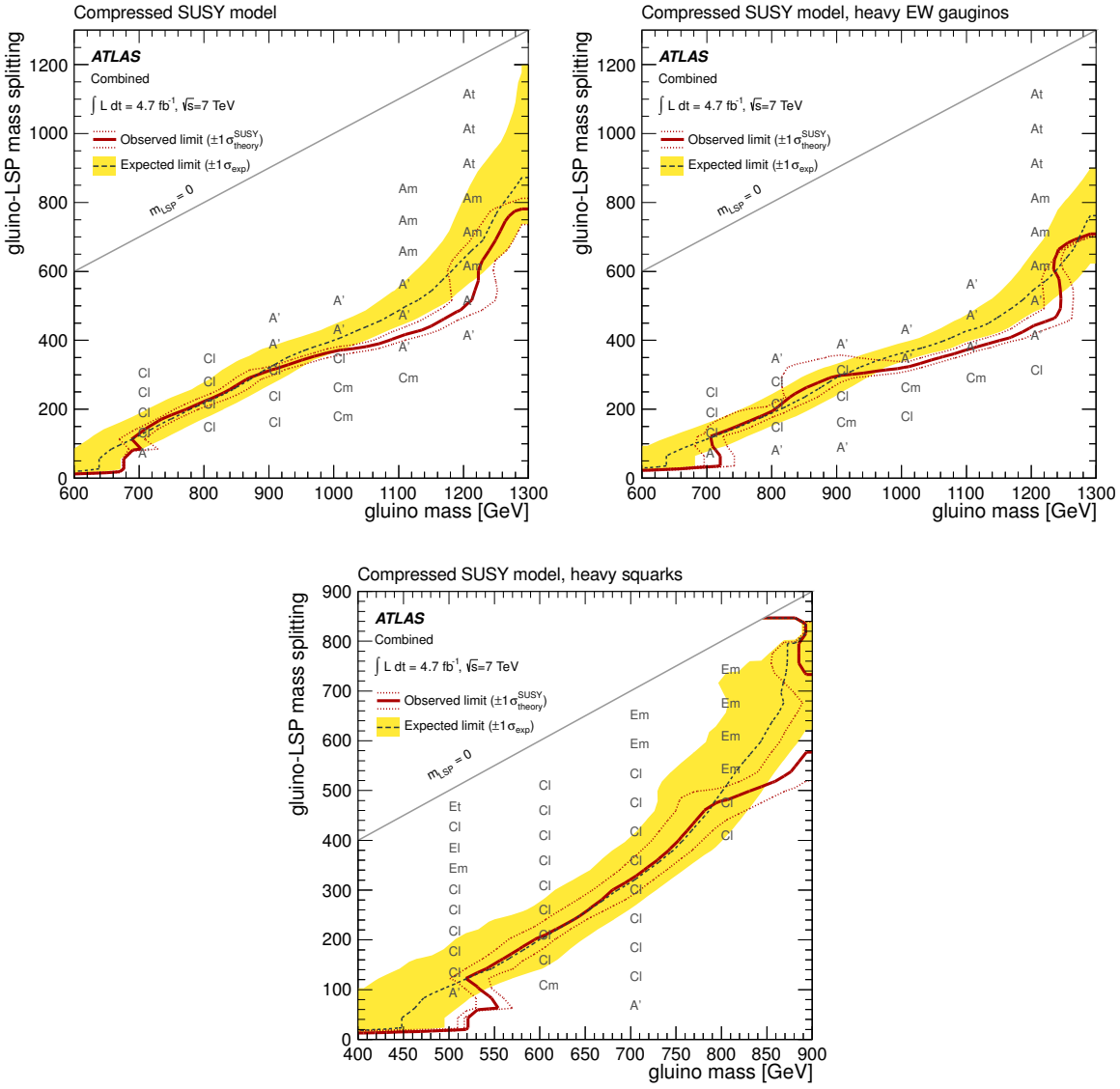

Figure 6.35: Compressed CMSSM like model. Top left: All squarks, electroweak gauginos and the gluino are kinematically accessible. Top right: neutralinos and charginos are not accessible. Bottom: Squarks are not accessible.

6.13 Status of searches for supersymmetric particles

So far all searches for supersymmetric particles were negative. No superpartner to a SM particle was observed. The most stringent limits on masses of squarks and gluinos before the LHC started where set by the Tevatron, see Refs. [133–135].

Besides the analysis of the full 7 TeV dataset a subset of the 8 TeV data set taken with ATLAS was

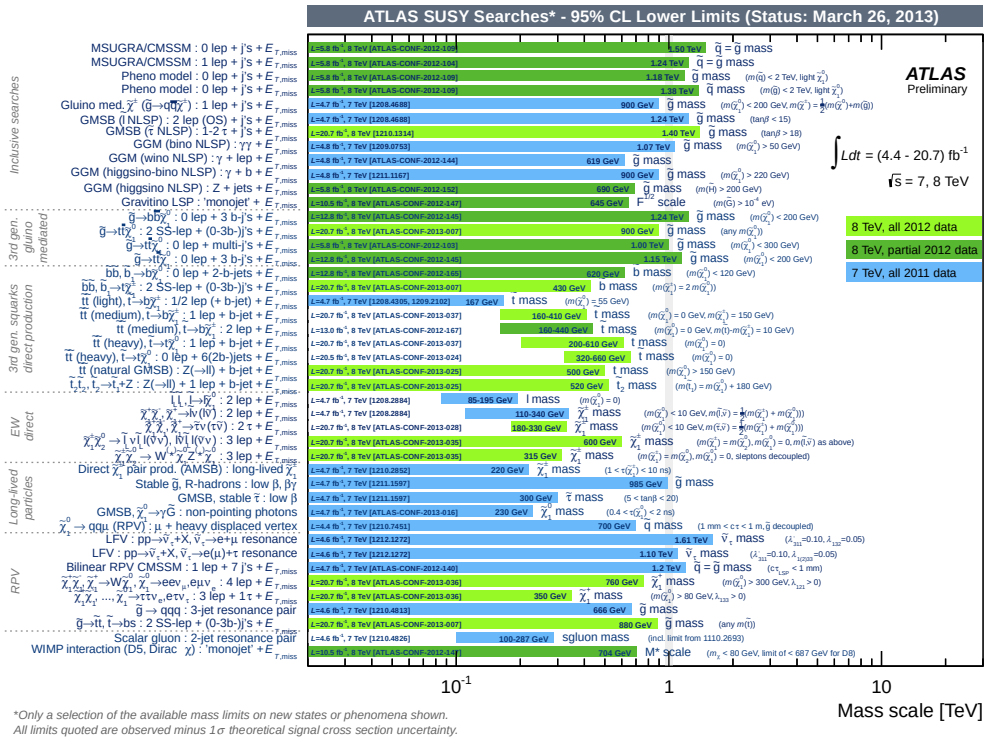

Figure 6.36: Overview on the mass reach of searches for supersymmetric particles with the ATLAS detector.

preliminary analyzed in final states with jets and $E_{\mathrm{T}}^{\mathrm{miss}}$ in Ref. [6] corresponding to 5.8 fb^{-1} of integrated luminosity. No deviation of the data from the background expectation was found either. The CMS experiment carried out similar searches to those carried out by ATLAS in final states with jets and missing transverse momentum, summarized in Ref. [136]. No significant deviation from the SM expectation was observed as well and similar limits on particle masses are set.

Depending on the primary produced particles, mass spectra and decay chains SUSY could manifest in a variety of signatures. Therefore a large amount of event topologies are investigated at the LHC. In Fig. 6.36 an overview of the searches carried out by ATLAS to date is shown[1]. Among others there are searches dedicated explicitly to third generation squarks which are favored to be light by natural SUSY. The impact of the measurement described in this thesis at an earlier stage corresponding to 1.04 fb^{-1} at 7 TeV center of mass energy [4] on the phenomenological MSSM (pMSSM) [85] was tested in Ref. [11].

[1] from https://twiki.cern.ch/twiki/bin/view/AtlasPublic/CombinedSummaryPlots#SusySummary, March 2013)

In the pMSSM the 105 parameters of the MSSM reduce to 19 which are considered the most important ones for phenomenology. Sampling from these parameters allows to investigate a very general view on the MSSM. It turns out that the searches in final states with jets and missing transverse momentum are excluding a large proportion > 95% of the sampled parameter space. MSSM signatures that may have eluded this searches include either low cross-sections or large decay chains. In case of the large decay chains, the jet spectra get very soft and fall below the p_{T} threshold of the searches.
In Ref. [137] the authors show that the pMSSM phase space with realistic conditions for light squarks of all three generations, light gluinos and low fine tuning is not excluded, yet. The indications of the SM Higgs mass being at ∼125 GeV is opposed to fine tuning in the pMSSM in Ref. [138]. The authors assume a SM Higgs particle identified at this mass and showed that within the pMSSM parameter space low fine tuned models still exist. However if fine tuning is taken as an exclusion criteria, a large phase of the pMSSM can be abandoned. Spots in the squark pair production based on the MSSM particle spectrum that are still allowed are discussed in Ref. [139]. Dedicated searches to the third generation of squarks improve the sensitivity to these decay modes, e.g. in Refs. [140, 141].
The search described in this thesis sets as well limits on the dark matter candidate of the MSSM, the neutralino. However, these limits only hold if the LSP occurs in a cascade decay of strongly produced particles and thus are model dependent. In Ref. [142] a review on dark matter searches is given. The sensitivity of direct LHC searches based on strong production of supersymmetric particles is opposed to constraints from experiments with a fixed target scattering experiments consisting of heavy nuclei targeted at the sky. The authors find that in the energy range of the dark mater candidate of $\sim 100-500$ GeV and at low nuclei-dark matter scattering cross sections the direct searches at the LHC are excluding a phase space on which the heavy nuclei experiments are not sensitive, yet. However these constraints are only valid for the assumption of the dark matter candidate to appear in cascades from strongly produced particles in the CMSSM.
Constrained supersymmetric models as the CMSSM are under heavy attack by the negative LHC searches for supersymmetric particles, by the potential SM Higgs candidate at ∼125 GeV, by constraints on rare decays of $B_s \to \mu\mu$ and direct dark matter searches with scattering experiments [143]. The authors show a degradation of the compatibility of the CMSSM with currently available observations.

Chapter 7

Summary

The start of the LHC in 2010 marks a new era in high energy particle physics. Protons are collided at unprecedented center-of-mass energies. The energy range under investigation at the LHC, reaching up to 14 TeV, has never been explored in a laboratory under such well controlled conditions as it is possible with a particle accelerator experiment.

The Standard Model of particle physics (SM) is very successful in describing elementary particles and their interactions. The recent discovery of a new boson at the LHC continues this successful story as it yields characteristics compatible with the last undiscovered particle in the SM, the Higgs boson. However, the SM has limitations such as the hierarchy problem or the missing dark matter candidate.

One of the extensions to the SM includes a new space-time symmetry, called Supersymmetry (SUSY), resulting in a symmetry between fermions and bosons. The hierarchy problem is heavily reduced if there are supersymmetric particles at the TeV scale. In minimal realizations of theories including such a symmetry, e.g. the Minimal Supersymmetric Standard Model (MSSM), a copy of each particle of the SM exists. If these new particles have masses of $\mathcal{O}(100)$ GeV up to several TeV they may be accessible with the LHC. Under the assumption of an additional $\mathbb{Z}_2$ symmetry, called R-Parity, the new particles are produced in pairs and the lightest supersymmetric particle (LSP) serves as a dark matter candidate.

In most phenomenological SUSY models the production of supersymmetric particles at the LHC is dominated by squark-squark, squark-anti-squark, squark-gluino and gluino-gluino pair production. Squarks are the super-partners to quarks and gluinos the super-partners to the gluons. These particles decay subsequently into the lightest supersymmetric particle which does not interact with detector material. Thus the striking signature for such a pair production of supersymmetric particles in proton-proton collisions are multiple jets in combination with missing transverse energy.

The ATLAS experiment surrounds an interaction point at the LHC and records the signatures of the particle collisions. This thesis contains a search for supersymmetric particles in final states with jets and

missing transverse momentum on data collected by the ATLAS experiment. The analysis corresponding to an integrated luminosity of $4.7\,\mathrm{fb}^{-1}$ of 7 TeV center of mass energy proton-proton collisions is discussed in detail. The search is carried out in dedicated signal regions defined in inclusive jet multiplicities from two to six jets and a large missing transverse momentum component.

The dominant sources of SM processes leading to similar signatures are as follows. The W + jets background is composed of events with a W decaying to a tau and a neutrino ($W \rightarrow \tau\nu$) or a W decaying into an electron or muon ($W \rightarrow l\nu$) in which no electron or muon candidate is reconstructed. The irreducible background Z + jets is dominated by events with a Z decaying to neutrinos ($Z \rightarrow \nu\nu$) and thus with large missing transverse energy. Hadronic τ decays in $t\bar{t}$-quark events which decay semi-leptonically ($t\bar{t} \rightarrow bb\tau\nu qq$) and single top events can generate large missing transverse momentum and pass the jet and lepton requirements. The multi-jet background is caused by rare instances of poor reconstruction of jet energies in calorimeters leading to fake missing transverse momentum and by neutrinos in the semi-leptonic decay of heavy quarks. For each of the main background components a control region is defined which requirements are as close as possible to the signal region selection, thus minimizing systematic uncertainties arising from extrapolation from control regions to the signal regions. For each selection a simultaneous normalization of the backgrounds is performed, taking into account correlations in the systematic uncertainties and signal contamination in the control regions.

The main results presented in this thesis are as follows. No deviation from the SM expectation has been found in the data. Stringent limits on the masses of the first two generations of squarks are presented. Under the assumption that they decay directly to the LSP, masses below 860 GeV are excluded at 95% confidence level. Gluino masses below 1320 GeV are excluded, assuming specific simple decay modes. In this simplified picture quarks and gluinos with equal masses are excluded below 1410 GeV. In the constrained MSSM (CMSSM) with $tan(\beta) = 10$, $A_0 = 0$ and $\mu > 0$, the limit on the universal gaugino masses $m_{1/2}$ is extended to 300 GeV at high universal scalar masses m_0 and to 640 GeV at low m_0. In the CMSSM the bounds on squarks and gluinos with equal masses reach up to 1360 GeV. The dependency of these results on the LSP mass is quite low as long as the mass of the LSP is less than 400 GeV.

The limits on the masses of gluinos and squarks of the first two generations presented in this thesis exceed the limits set by previous experiments, such as the Tevatron [133–135], by far and are compatible to the limits found by the CMS collaboration [136]. The results of this search constrain the phase space of the parameters of the MSSM and thus provide important information to model building. In the phenomenological MSSM large parts of the phase space are excluded by the results presented in this thesis [11].

The shutdown of the LHC in 2013-15 will be used to further investigate the coverage of these searches in the MSSM phase space and beyond. The challenge will be to identify any admissible signatures of supersymmetric particles and search for them in an updated or in a new analysis at higher luminosity and higher center of mass energy. From 2015 on the LHC will run with a center of mass energy of up

to 14 TeV, and supersymmetric particles in a higher, yet unexplored, mass range will be kinematically accessible.

Appendix A

Exclusive event selection and shape analysis

A more rigorous approach to extract more information from the data is to use the shape information of distributions and combine information from several measurements. The shape information can be gathered using binned distributions. A proper combination of bins is possible if the bins are statistically independent. In this section an approach is studied to use the information on m_{eff} and the jet multiplicity in an exclusive manner. Opposed to the main part of the text jet selections are defined exclusively. In the example below a two dimensional plane is considered with one dimension being m_{eff} with four bins ranging from 800-2200+ GeV and the other dimension being the jet multiplicity with five bins ranging from 2-6+ jets. The + indicated that the last bin sums up all entries above the upper limit of the last bin. If we assume a binned distribution with n bins the likelihood expands to the form:

$$L(\boldsymbol{n}|\mu, \boldsymbol{\mu}_b, \boldsymbol{\theta}) \quad = \quad \prod_{j \in \text{n}} \; P_{\text{SR,j}} \; \times \; \prod_{CRX} P_{\text{CRX,j}} \; \times \; C_{\text{Syst}} \tag{A.1}$$

The pdf C_{Syst} can but does not have to depend on the binning depending on its implementation. The shape of the distribution is given by the values of N. The values of N are usually estimated via MC. If the shape of the distribution should keep exactly the shape from N, that is the initial estimate, only the absolute normalization of the distribution should be changed. This is done similar to the single bin setup via the vector $\boldsymbol{\mu} = (\mu, \boldsymbol{\mu}_b)$. For each process one degree of freedom exists and the likelihood reads:

$$L(\boldsymbol{n}|\mu, \boldsymbol{\mu}_b, N, \boldsymbol{\theta}) \quad = \quad \prod_{j \in \text{n}} \; P_{\text{SR,j}}(\boldsymbol{\mu}_b) \; \times \; \prod_{CRX} P_{\text{CRX,j}}(\boldsymbol{\mu}_b) \; \times \; C_{\text{Syst}} \tag{A.2}$$

However at this stage of the experiment or especially the status of the MC simulation with not fully understood discrepancies between MC simulation and data a data driven approach to the shape information is mandatory. This can be achieved by expanding the background strength vector $\boldsymbol{\mu}_b$ to a matrix containing the shape information per background process and per bin $\boldsymbol{\mu}_{b,j}$. This definition allows the background process strengths $\boldsymbol{\mu}_{b,j}$ to adapt to the shape of the data distributions in the CRs. The likelihood thus

expands to:

$$L(\boldsymbol{n}|\mu, \boldsymbol{\mu}_{b,j}, N, \boldsymbol{\theta}) \quad = \quad \prod_{j \in \mathrm{n}} \quad P_{\mathrm{SR,j}}(\boldsymbol{\mu}_{b,j}) \times \prod_{CRX} P_{\mathrm{CRX,j}}(\boldsymbol{\mu}_{b,j}) \times C_{\mathrm{Syst}} \tag{A.3}$$

A slice of this likelihood is depicted in Fig. A.1 where the projection on the part corresponding to events with exactly two jets, that is the first bin of the jet multiplicity distribution, is shown. The m_{eff} distribution in CR3 is shown before the minimization in the discovery mode in Fig. A.1(a) and after in Fig. A.1(b), in CR4 before in Fig. A.1(c) and after in Fig. A.1(d) and in the SR before in Fig. A.1(e) and after in Fig. A.1(f). Note that the assumptions in this model are simplified: No multi-jets contribution is considered and the number of uncertainties was reduced to reduce the number of free parameters in the model. Problems arising in this approach is the modelling of the nuisance parameters and constrains from data on the nuisance parameters. The increased number of data bins which are fitted against a model where the only correlated parameters among bins are nuisance parameters corresponding to systematic uncertainties tend to reduce the uncertainty of the parameters. The background strengths per bin are basically free and adapt to the data observed in the bin. To use this setup properly a very precise understanding of the uncertainties and their modelling must exist. Otherwise information form the data will falsely be used to reduce uncertainties on nuisance parameters where it is not appropriate. Another important issue is that if there are statistical fluctuations present these can have the same effect of falsely reducing uncertainties on nuisance parameters.

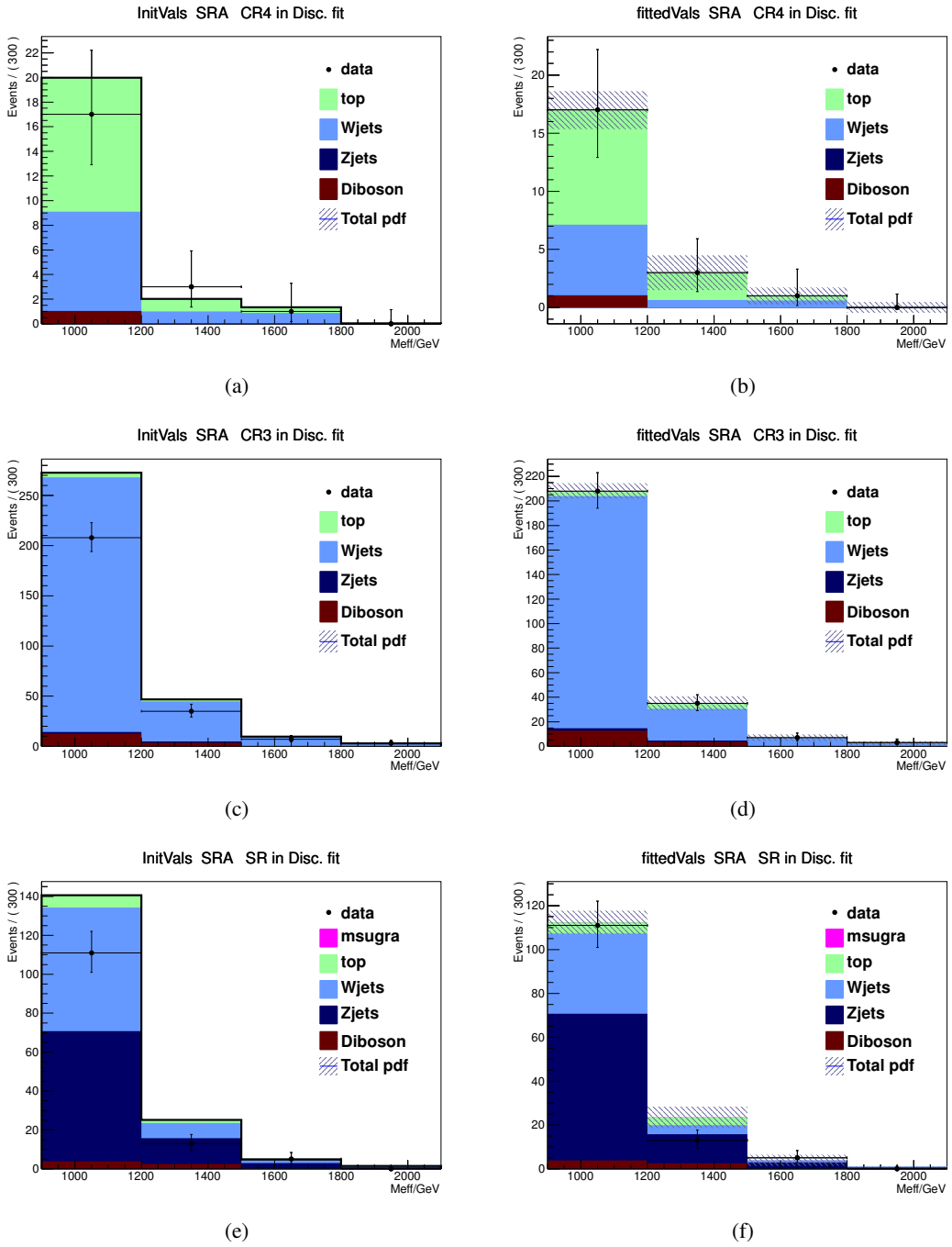

Figure A.1: Projection on a plane in jet multiplicity requiring exactly 2 jets. The m_{eff} distribution before and after the minimization in the Discovery mode are plotted.

Appendix B

Unified Extra Dimensions

An example of the sensitivity to other beyond SM scenarios is shown in Ref. [12] where an additional interpretation of the analysis in the context of a minimal universal extra dimensions model [65–67] is performed. The analysis used is described in Ref. [4] corresponds to 1.04 fb^{-1} of integrated luminosity and is the predecessor of the analysis described in the main text. In Fig. B.1 a interpretation with the MUED framework is presented in terms the compactification scale (R^{-1}) and the compression scale ($\Lambda \cdot R$) and the masses of the Kaluza-Klein gluon g_{KK} and the Kaluza-Klein photon γ_{KK}.

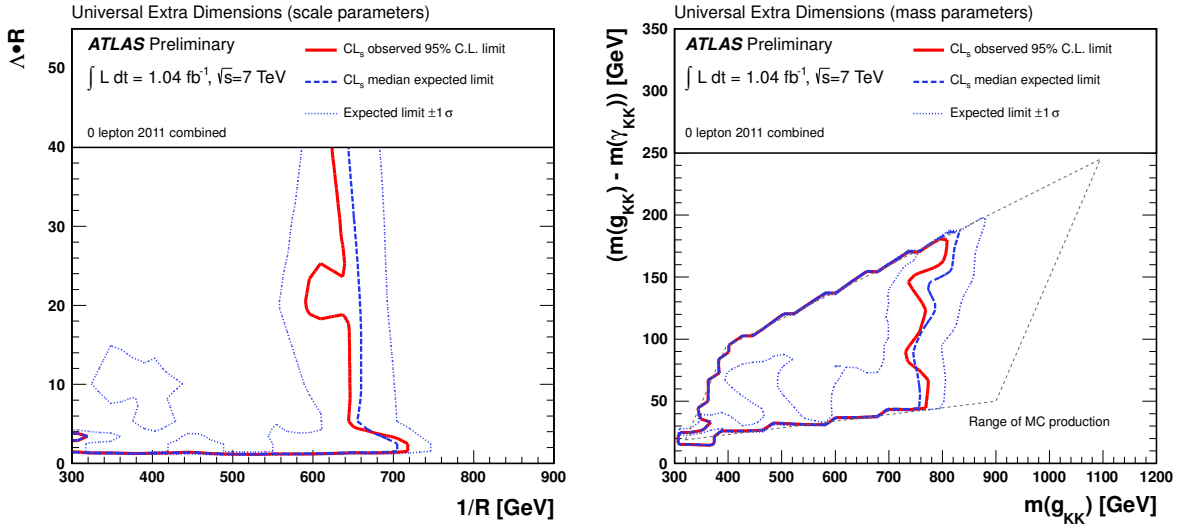

Figure B.1: Exclusion limits in the Universal Extra Dimensions model space, in terms of [left] the compactification scale (R^{-1}) and the compression scale ($\Lambda \cdot R$) and [right] the masses of the Kaluza-Klein gluon g_{KK} and the Kaluza-Klein photon γ_{KK} (LKP).

Appendix C

Combination of search channels

This section describes the combination of the searches for supersymmetry in the 0-lepton channel [1] and the 1-lepton channel [144] performed by ATLAS using the 2010 dataset corresponding to $35\,\mathrm{pb}^{-1}$ [13] of integrated luminosity. Both analyses require jets and $E_{\mathrm{T}}^{\mathrm{miss}}$, the 0-lepton channel vetoes electrons or muons whereas the 1-lepton search requires exactly one electron or muon. Thus the signal and control regions of each channel are statistically exclusive. Both analyses are counting experiments and showed no deviation from SM expectations. Let L_0 and L_1 be the likelihood containing the information on the measurement of the 0-lepton channel and 1-lepton channel, respectively.

$$L_0 = L(\boldsymbol{n}_0|\mu;\boldsymbol{\mu_b}_0;\boldsymbol{s}_0;N_0;\boldsymbol{\theta};\boldsymbol{\theta}_0) \tag{C.1}$$

$$L_1 = L(\boldsymbol{n}_1|\mu;\boldsymbol{\mu_b}_1;\boldsymbol{s}_1;N_1;\boldsymbol{\theta};\boldsymbol{\theta}_1) \tag{C.2}$$

Uncorrelated terms between L_0 and L_1 are

- $\boldsymbol{n}_0$ and $\boldsymbol{n}_1$ being the set of measurements in the 0-lepton channel and 1-lepton channel, respectively.
- $\boldsymbol{\mu_b}_0$ and $\boldsymbol{\mu_b}_1$ denoting the background process strength vector in the 0-lepton channel and 1-lepton channel, respectively.
- $\boldsymbol{s}_0$ and $\boldsymbol{s}_1$ being the vector of estimated non-SM signal events from MC in the 0-lepton channel and 1-lepton channel, respectively.
- N_0 and N_1 being the matrix of initially estimated background events in the 0-lepton channel and 1-lepton channel, respectively.
- $\boldsymbol{\theta}_0$ and $\boldsymbol{\theta}_1$ is the set of nuisance parameters that parametrise systematic uncertainties which are not correlated between the 0-lepton channel and 1-lepton channel.

Correlated terms between L_0 and L_1 are

- μ the signal strength.

- $\boldsymbol{\theta}$ the set of nuisance parameters that parametrise systematic uncertainties which are *correlated* between the 0-lepton channel and 1-lepton channel.

The total likelihood is the product of contributions from the 0-lepton and 1-lepton channels.

$$L_{tot} = L_0 \times L_1 \tag{C.3}$$

Systematic uncertainties in common between all channels are: the jet energy scale, signal cross section uncertainty, and the luminosity uncertainty. These uncertainties are treated as 100% correlated. The correlated systematic uncertainties are accounted for when building the combined likelihood through the use of common nuisance parameters $\boldsymbol{\theta}$, and a single common Gaussian constraint per nuisance parameter. All other uncertainties are taken as uncorrelated and modelled via $\boldsymbol{\theta}_0$ and $\boldsymbol{\theta}_1$.

The combined exclusion limits are obtained performing pseudo-experiments; they are derived at 95% confidence level (C.L.) using as test statistic a one-sided profile likelihood ratio as described in section 6.9.5. The combined exclusion contour is shown in Fig. C.1 and is done per grid point in the m_0, $m_{1/2}$ plane of the CMSSM framework. At each grid point, the 0-lepton channel the best expected exclusion sensitivity.

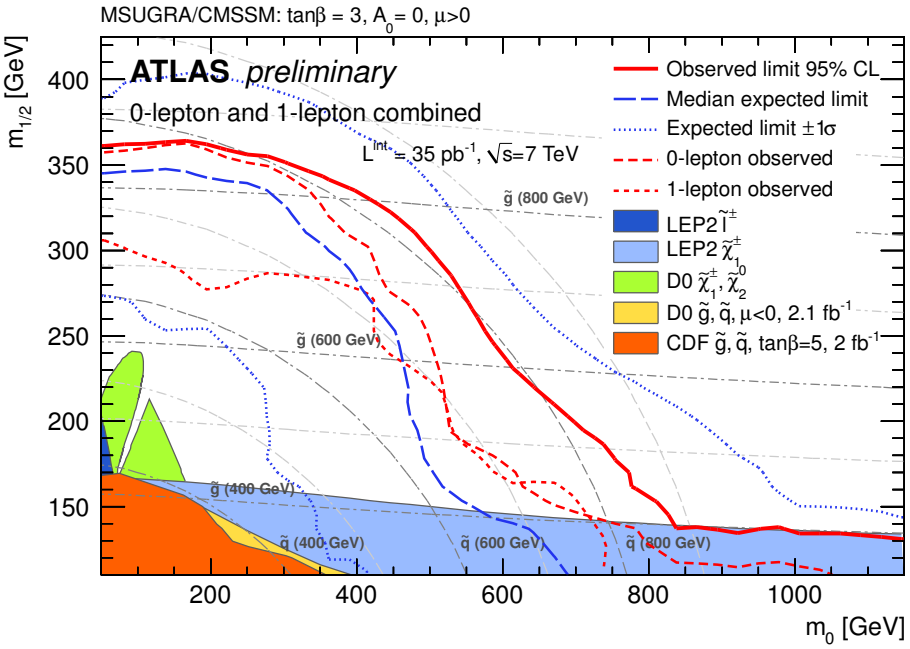

Figure C.1: Expected and observed limits for the combined 0- and 1-lepton channels. The blue dashed line corresponds to the expected median 95% C.L. exclusion limit, the dashed-solid blue lines to $\pm 1\sigma$ 95% C.L. (PCL) limits respectively. The red line represents the combined observed limit. The observed limits for the individual 0-lepton and 1-lepton channels are indicated with red dashed lines. Tevatron and LEP limits on $m_{\tilde{q}}$ and $m_{\tilde{g}}$ are marked for searches in the specific context of MSUGRA/CMSSM, with $\tan(\beta) = 3$, $A_0 = 0$ and $\mu > 0$, and are also shown for illustration.

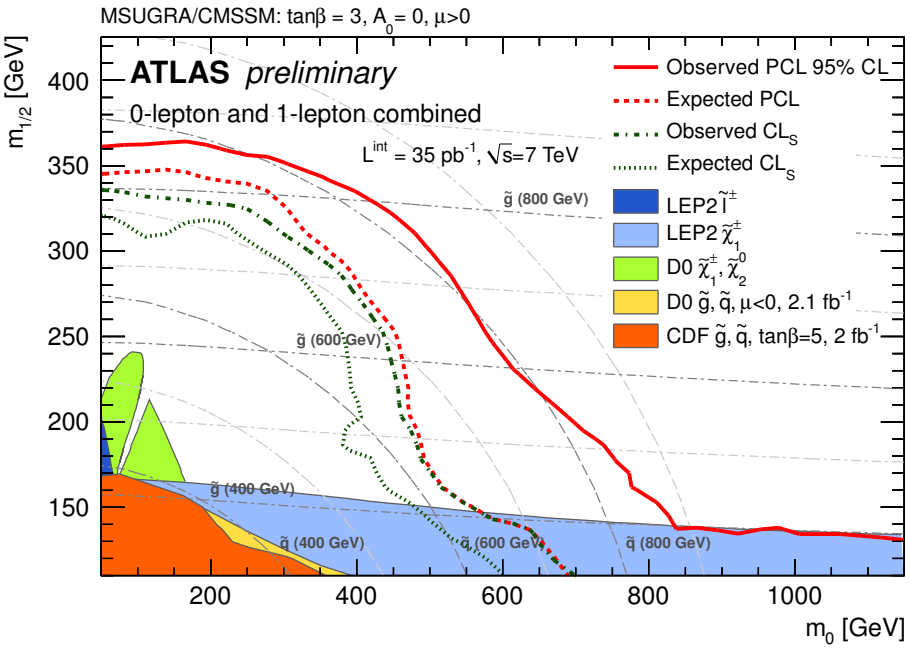

Figure C.2: Expected and observed limits of the combined 0-and 1-lepton channels derived with the power constrained limit (PCL) and the CL_s method. The red dashed line corresponds to the expected median PCL at 95% C.L., and the red solid line to the observed PCL at 95% C.L. The green dotted line corresponds to the expected median exclusion contour at 95% C.L. derived with the CL_s method, and the green dashed-dotted line corresponds to the observed exclusion contour at 95% C.L. derived with the CL_s method. Tevatron and LEP limits on $m_{\tilde{q}}$ and $m_{\tilde{g}}$ are marked for searches in the specific context of MSUGRA/CMSSM, with $\tan(\beta) = 3$, $A_0 = 0$ and $\mu < 0$, and are also shown for illustration.

Appendix D

Search in multi-leptonic final states and missing transverse energy

In Ref. [14, 15] final states with three or more isolated electrons or muons, jets and intermediate missing transverse energy are investigated. Electrons and muons in originate from the decay of charginos and neutralinos produced in cascade decays of primary produced colored sparticles. The selection ensures a well defined sample with low background.
The total number of SM background events expected in this search th in $34\,\mathrm{pb}^{-1}$ of data collected in 2010 is $0.109 \pm 0.023^{+0.036}_{0.025}$. No event was observed in data passing all selection criteria. Limits are calculated in the MSUGRA/CMSSM framework in the m_0, $m_{1/2}$ plane with $\tan(\beta) = 3$, $A_0 = 0$ and $\mu > 0$ and are shown in Fig. D.1.

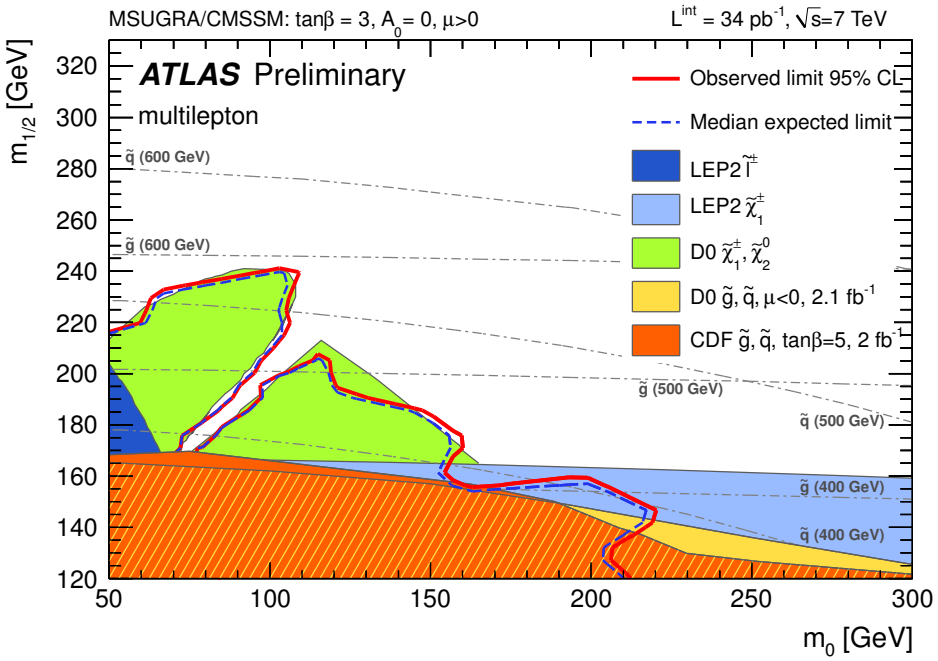

Figure D.1: Expected and observed limits. The blue dashed line corresponds to the expected median 95% C.L. exclusion limit, the dashed-solid blue lines to $\pm 1\sigma$ 95% C.L. (PCL) limits respectively. The red line represents the observed limit. Tevatron and LEP limits are also shown for illustration.

Appendix E

Transfer-function Summary

Region	Main CR/Process				
	CR1a / Z/γ+jets	CR2 / QCD jets	CR4 / $t\bar{t}$+ Single Top	CR3 / W+jets	CR1b / Z/γ+jets
CR1a	1	0	0	0	
CR2	0.075	1	0.38	0.21	0.79
CR4	0.00069	0	1	0.098	0.0073
CR3	0.0087	0	0.34	1	0.092
CR1b		0	0.018	0	1
SR	0.32	0.016	0.52	0.36	2.9

Table E.1: Initial cross Transfer Factors for SRC (loose).

Region	Main CR/Process				
	CR1a / Z/γ+jets	CR2 / QCD jets	CR4 / $t\bar{t}$+ Single Top	CR3 / W+jets	CR1b / Z/γ+jets
Central value	0.32	0.016	0.52	0.36	2.9
JER	0.002 0		0.016 0	0.0045 0	0.14 0
JES	0.0023 −0.0093		−0.002 −0.0034	0.0016 −0.025	0.63 −0.19
Pileup			0 −0.0011	0 −0.0083	
l resoln.			−0.0033 0.0031	−0.00084 0.00074	0 −0
Trigger			−0.0029 0.003	−0.002 0.002	−0.03 0.03
b-tag/veto eff.			−0.038 0.052	−0.0062 0.0064	
acc. Z+jets/ γ	0.084 −0.084				
l scale.			−0.0034 0.0037	−0.0023 0.003	0 −0.025
QCD smear.		0.012 −0.012			
MET CellOut cluster	0.00046 −0.0036		−0.0031 −0.0013	−0.0016 −0.00022	
Top Theory			0.052 −0.052		
l eff.			−0.0036 0.0037	−0.0024 0.0025	−0.035 0.035
MET CellOut pileup	0.00015 −0.0032		−0.0027 −0.0021	0.00017 −0.00028	
PDF			−0.0033 0.0045	−0.0062 −0.0017	
Z+jets Theory					0.017 −0.017
MC stat.			0.034 −0.034	0.022 −0.022	0.35 −0.35
W+jets Theory				0.029 −0.029	

Table E.2: Initial uncertainties of Transfer Factors to signal region for SRC (loose).

Region	Main CR/Process				
	CR1a / Z/γ+jets	CR2 / QCD jets	CR4 / $t\bar{t}$+ Single Top	CR3 / W+jets	CR1b / Z/γ+jets
CR1a	1	0	0	0	
CR2	0.11	1	0.8	0.57	0
CR4	0	0	1	0.14	0
CR3	0.014	0	0.3	1	0
CR1b		0	0	0	0
SR	0.27	0.048	0.92	0.74	6.5

Table E.3: Initial cross Transfer Factors for SRE (loose).

Region	Main CR/Process				
	CR1a / Z/γ+jets	CR2 / QCD jets	CR4 / $t\bar{t}$+ Single Top	CR3 / W+jets	CR1b / Z/γ+jets
Central value	0.27	0.048	0.92	0.74	6.5
JER	0.014 0		0.018 0	−0.012 0	3.7 0
JES	0.011 −0.003		−0.034 −0.0073	−0.035 −0.065	2.7 −1.6
Pileup			0 0.00094	0 0.016	
l resoln.			−0.0098 0.0078	−0.006 0.0038	0 −0
Trigger			−0.0054 0.0055	−0.0044 0.0044	−0.07 0.071
b-tag/veto eff.			−0.068 0.092	−0.014 0.015	
acc. Z+jets/ γ	0.08 −0.08				
l scale.			−0.012 0.0088	−0.0052 0.0046	0 −0
QCD smear.		0.04 −0.04			
MET CellOut cluster	0.00087 −0.0012		0.0053 −0.01	−0.0021 −0.0042	
Top Theory			0.14 −0.14		
l eff.			−0.0066 0.0067	−0.0052 0.0053	−0.086 0.087
MET CellOut pileup	0.00055 −0.0019		0.0032 −0.0064	−0.0013 −0.0034	
PDF			−0.024 0.034	−0.0075 0.00035	
Z+jets Theory					0.065 −0.065
MC stat.			0.072 −0.072	0.072 −0.072	2.5 −2.5
W+jets Theory				0.081 −0.081	

Table E.4: Initial uncertainties of Transfer Factors to signal region for SRE (loose).

Region	Main CR/Process				
	CR1a / Z/γ+jets	CR2 / QCD jets	CR4 / $t\bar{t}$+ Single Top	CR3 / W+jets	CR1b / Z/γ+jets
CR1a	1	0	0	0	
CR2	0.046	1	0.3	0.19	0.31
CR4	0	0	1	0.071	0
CR3	0.018	0	0.46	1	0.12
CR1b		0	0.039	0	1
SR	0.36	0.032	0.34	0.31	2.5

Table E.5: Initial cross Transfer Factors for SRA (medium).

Region	Main CR/Process				
	CR1a / Z/γ+jets	CR2 / QCD jets	CR4 / $t\bar{t}$+ Single Top	CR3 / W+jets	CR1b / Z/γ+jets
Central value	0.36	0.032	0.34	0.31	2.5
JER	0.01 0		0.022 0	−0.021 0	−0.14 0
JES	0.0011 −0.00014		0.049 0.0087	0.0069 0.017	−0.46 0.9
Pileup			0 0.034	0 −0.014	
l resoln.			−0.0041 0.0092	−0.0039 0.0027	0 −0
Trigger			−0.0018 0.0019	−0.0017 0.0017	−0.028 0.029
b-tag/veto eff.			−0.027 0.039	−0.0032 0.0033	
acc. Z+jets/ γ	0.096 −0.096				
l scale.			−0.0041 0.0055	−0.0052 0.00047	−0.05 −0.034
QCD smear.		0.019 −0.019			
MET CellOut cluster	0.0012 $-3.2e{-}05$		−0.00074 −0.0061	−0.00082 −0.0015	
Top Theory			0.2 −0.2		
l eff.			−0.0023 0.0024	−0.002 0.002	−0.032 0.032
MET CellOut pileup	0.00049 $-1.8e{-}05$		−0.00058 −0.0022	−0.00077 $9.4e{-}05$	
PDF			0.006 −0.0094	−0.0067 0.014	
Z+jets Theory					0.1 −0.1
MC stat.			0.078 −0.078	0.035 −0.035	0.46 −0.46
W+jets Theory				0.025 −0.025	

Table E.6: Initial uncertainties of Transfer Factors to signal region for SRA (medium).

Region	Main CR/Process				
	CR1a / Z/γ+jets	CR2 / QCD jets	CR4 / $t\bar{t}$+ Single Top	CR3 / W+jets	CR1b / Z/γ+jets
CR1a	1	0	0	0	
CR2	0.028	1	0.063	0.08	0.15
CR4	0.00091	0	1	0.067	0.0049
CR3	0.017	0	0.41	1	0.091
CR1b		0	0.036	0	1
SR	0.39	0.1	0.23	0.19	2.2

Table E.7: Initial cross Transfer Factors for SRAp (medium).

Region	Main CR/Process				
	CR1a / Z/γ+jets	CR2 / QCD jets	CR4 / $t\bar{t}$+ Single Top	CR3 / W+jets	CR1b / Z/γ+jets
Central value	0.39	0.1	0.23	0.19	2.2
JER	0.013 0		0.0018 0	−0.0066 0	0.41 0
JES	0.0021 −0.0022		−0.015 −0.038	0.0096 0.0005	−0.064 0.48
Pileup			0 0.00075	0 −0.0068	
l resoln.			−0.00086 0.0037	−0.0015 0.0023	0 −0
Trigger			−0.0013 0.0013	−0.001 0.001	−0.038 0.039
b-tag/veto eff.			−0.012 0.019	−0.0019 0.002	
acc. Z+jets/ γ	0.1 −0.1				
l scale.			−0.001 0.003	−0.0019 0.00074	−0.016 0.0057
QCD smear.		0.061 −0.061			
MET CellOut cluster	0.00072 −0.00049		0.00054 −0.0016	0.00033 −0.0028	
Top Theory			0.043 −0.043		
l eff.			−0.0016 0.0016	−0.0012 0.0012	−0.032 0.032
MET CellOut pileup	0.00051 −0.00016		−0.00031 0.00065	−0.00062 −0.00047	
PDF			0.0038 −0.0054	0.00099 0.0073	
Z+jets Theory					0.087 −0.087
MC stat.			0.039 −0.039	0.017 −0.017	0.26 −0.26
W+jets Theory				0.013 −0.013	

Table E.8: Initial uncertainties of Transfer Factors to signal region for SRAp (medium).

Region	Main CR/Process				
	CR1a / Z/γ+jets	CR2 / QCD jets	CR4 / $t\bar{t}$+ Single Top	CR3 / W+jets	CR1b / Z/γ+jets
CR1a	1	0	0	0	
CR2	0.11	1	0.74	0.51	0
CR4	0	0	1	0.15	0
CR3	0.01	0	0.28	1	0
CR1b		0	0	0	0
SR	0.32	0.038	0.62	0.39	5

Table E.9: Initial cross Transfer Factors for SRE (medium).

Region	Main CR/Process				
	CR1a / Z/γ+jets	CR2 / QCD jets	CR4 / $t\bar{t}$+ Single Top	CR3 / W+jets	CR1b / Z/γ+jets
Central value	0.32	0.038	0.62	0.39	5
JER	0.03 0		0.047 0	0.0051 0	7.9 0
JES	0.021 −0.0063		0.044 0.013	0.0046 −0.012	3.8 0.79
Pileup			0 0.074	0 0.015	
l resoln.			−0.0043 0.018	−0.0038 0.0036	0 −0
Trigger			−0.0037 0.0038	−0.0022 0.0023	−0.057 0.057
b-tag/veto eff.			−0.043 0.063	−0.008 0.0084	
acc. Z+jets/ γ	0.096 −0.096				
l scale.			−0.0052 0.014	−0.0027 0.00098	0 −0
QCD smear.		0.031 −0.031			
MET CellOut cluster	1.4e−05 −2.7e−05		0.0022 0.012	0.00037 −0.0042	
Top Theory			0.1 −0.1		
l eff.			−0.0047 0.0048	−0.0028 0.0028	−0.067 0.068
MET CellOut pileup	1.8e−05 −0.00055		−0.0043 0.00084	−0.0014 0.00033	
PDF			−0.032 0.046	0.0051 0.00084	
Z+jets Theory					0.05 −0.05
MC stat.			0.11 −0.11	0.081 −0.081	3.2 −3.2
W+jets Theory				0.046 −0.046	

Table E.10: Initial uncertainties of Transfer Factors to signal region for SRE (medium).

Region	Main CR/Process				
	CR1a / Z/γ+jets	CR2 / QCD jets	CR4 / $t\bar{t}$+ Single Top	CR3 / W+jets	CR1b / Z/γ+jets
CR1a	1	0	0	0	
CR2	0.032	1	0.05	0.32	0.49
CR4	0	0	1	0.43	0
CR3	0	0	0.053	1	0
CR1b		0	0.0039	0	1
SR	0.3	0.009	0.013	0.25	5.3

Table E.11: Initial cross Transfer Factors for SRA (tight).

Region	Main CR/Process				
	CR1a / Z/γ+jets	CR2 / QCD jets	CR4 / $t\bar{t}$+ Single Top	CR3 / W+jets	CR1b / Z/γ+jets
Central value	0.3	0.009	0.013	0.25	5.3
JER	0.011 0		−0.0013 0	−0.01 0	−1.4 0
JES	0.00085 −0.00028		0.0093 −0.012	−0.0049 −0.021	−2 1.7
Pileup			0 −0.0041	0 0.00072	
l resoln.			0 0	−0.0023 0.0023	0 −0
Trigger			$-6.7e{-}05$ $6.8e{-}05$	−0.0017 0.0017	−0.11 0.11
b-tag/veto eff.			−0.00088 0.0014	−0.0027 0.0028	
acc. Z+jets/ γ	0.08 −0.08				
l scale.			0 0	0 0.001	0 −0
QCD smear.		0.009 −0.0089			
MET CellOut cluster	0.0013 $-2.2e{-}09$		−0.00012 0.00022	−0.00045 −0.0091	
Top Theory			0.012 −0.012		
l eff.			$-9e{-}05$ $9.1e{-}05$	−0.002 0.002	−0.12 0.12
MET CellOut pileup	0.00054 $-1.7e{-}09$		−0.00013 0.00015	−0.00045 0.00079	
PDF			0.0023 −0.0036	−0.01 0.03	
Z+jets Theory					0.85 −0.85
MC stat.			0.0091 −0.0091	0.089 −0.089	3.2 −3.2
W+jets Theory				0.023 −0.023	

Table E.12: Initial uncertainties of Transfer Factors to signal region for SRA (tight).

Region	Main CR/Process				
	CR1a / Z/γ+jets	CR2 / QCD jets	CR4 / $t\bar{t}$+ Single Top	CR3 / W+jets	CR1b / Z/γ+jets
CR1a	1	0	0	0	
CR2	0.09	1	0.064	0.29	1.2
CR4	0	0	1	0.43	0
CR3	0	0	0.042	1	0
CR1b		0	0.0037	0	1
SR	0.38	0.011	0.022	0.14	4.2

Table E.13: Initial cross Transfer Factors for SRB (tight).

Region	Main CR/Process				
	CR1a / Z/γ+jets	CR2 / QCD jets	CR4 / $t\bar{t}$+ Single Top	CR3 / W+jets	CR1b / Z/γ+jets
Central value	0.38	0.011	0.022	0.14	4.2
JER	0.016 0		0.002 0	−0.0022 0	0 0
JES	0.016 −0.0081		0.0079 −0.0069	0.029 −0.019	1.8 −4.2
Pileup			0 −0.0061	0 −0.0064	
l resoln.			0 0	−0.0014 0.0014	0 −0
Trigger			−0.00011 0.00011	−0.00084 0.00085	−0.085 0.087
b-tag/veto eff.			−0.0015 0.0023	−0.0015 0.0015	
acc. Z+jets/ γ	0.1 −0.1				
l scale.			0 0	0 0.00062	0 −0
QCD smear.		0.0078 −0.0078			
MET CellOut cluster	0.0032 $-1.2e{-}09$		−0.00021 0.00038	−0.00031 −0.016	
Top Theory			0.017 −0.017		
l eff.			−0.00015 0.00015	−0.00098 0.001	−0.081 0.084
MET CellOut pileup	0.0032 $-1.4e{-}09$		−0.00022 0.00025	−0.00031 −0.016	
PDF			0.0035 −0.0056	−0.0022 0.015	
Z+jets Theory					0.92 −0.92
MC stat.			0.013 −0.013	0.053 −0.053	3.1 −3.1
W+jets Theory				0.044 −0.044	

Table E.14: Initial uncertainties of Transfer Factors to signal region for SRB (tight).

Region	Main CR/Process				
	CR1a / Z/γ+jets	CR2 / QCD jets	CR4 / $t\bar{t}$+ Single Top	CR3 / W+jets	CR1b / Z/γ+jets
CR1a	1	0	0	0	
CR2	0.18	1	0.37	0.16	0.44
CR4	0	0	1	0.095	0
CR3	0	0	0.36	1	0
CR1b		0	0.022	0	1
SR	0.32	0.0034	0.15	0.16	1.8

Table E.15: Initial cross Transfer Factors for SRC (tight).

Region	Main CR/Process				
	CR1a / Z/γ+jets	CR2 / QCD jets	CR4 / $t\bar{t}$+ Single Top	CR3 / W+jets	CR1b / Z/γ+jets
Central value	0.32	0.0034	0.15	0.16	1.8
JER	0.0071 0		0.00068 0	0.0089 0	0.79 0
JES	0.013 −0.04		0.0022 0.031	0.033 −0.03	1 0.63
Pileup			0 −0.0073	0 −0.0031	
l resoln.			−0.0036 0.00099	−0.0015 0.00073	0 −0
Trigger			−0.00078 0.00079	−0.00081 0.00082	−0.027 0.027
b-tag/veto eff.			−0.016 0.022	−0.0031 0.0033	
acc. Z+jets/ γ	0.085 −0.085				
l scale.			−0.0036 0.005	−0.00037 0.00037	0 −0.13
QCD smear.		0.0044 −0.0025			
MET CellOut cluster	0.0017 −0.00029		0.0026 0.0027	0.00031 0.0009	
Top Theory			0.098 −0.098		
l eff.			−0.001 0.001	−0.00098 0.00099	−0.027 0.027
MET CellOut pileup	$2.2e{-}09$ −0.0033		0.0026 0.002	0.0021 0.00079	
PDF			−0.0056 0.0096	−0.0049 0.0057	
Z+jets Theory					0.18 −0.18
MC stat.			0.074 −0.074	0.046 −0.046	0.63 −0.63
W+jets Theory				0.091 −0.091	

Table E.16: Initial uncertainties of Transfer Factors to signal region for SRC (tight).

Region	Main CR/Process				
	CR1a / Z/γ+jets	CR2 / QCD jets	CR4 / $t\bar{t}$+ Single Top	CR3 / W+jets	CR1b / Z/γ+jets
CR1a	1	0	0	0	
CR2	0.4	1	0.57	0.35	0.95
CR4	0	0	1	0.13	0
CR3	0	0	0.32	1	0
CR1b		0	0.014	0	1
SR	0.29	0.02	0.2	0.26	2.1

Table E.17: Initial cross Transfer Factors for SRD (tight).

Region	Main CR/Process				
	CR1a / Z/γ+jets	CR2 / QCD jets	CR4 / $t\bar{t}$+ Single Top	CR3 / W+jets	CR1b / Z/γ+jets
Central value	0.29	0.02	0.2	0.26	2.1
JER	0.053 0		0.023 0	0.046 0	4.1 0
JES	0.033 −0.0098		0.01 0.024	0.033 −0.039	2.2 2.5
Pileup			0 0.00063	0 0.0082	
l resoln.			−0.0056 0.0015	−0.0043 0.0021	0 −0
Trigger			−0.00094 0.00095	−0.0014 0.0014	−0.02 0.021
b-tag/veto eff.			−0.024 0.034	−0.0065 0.0069	
acc. Z+jets/ γ	0.076 −0.076				
l scale.			−0.0056 0.0078	−0.001 0.0011	0 −0.23
QCD smear.		0.012 −0.012			
MET CellOut cluster	2.2e−09 −5.6e−09		0.0023 0.0044	0.0047 0.0036	
Top Theory			0.12 −0.12		
l eff.			−0.0013 0.0013	−0.0017 0.0017	−0.022 0.022
MET CellOut pileup	9.8e−10 −5.6e−09		0.0022 0.0025	−0.0015 0.0043	
PDF			−0.0076 0.013	−0.0038 0.013	
Z+jets Theory					0.19 −0.19
MC stat.			0.088 −0.088	0.078 −0.078	1.1 −1.1
W+jets Theory				0.036 −0.036	

Table E.18: Initial uncertainties of Transfer Factors to signal region for SRD (tight).

Region	Main CR/Process				
	CR1a / Z/γ+jets	CR2 / QCD jets	CR4 / $t\bar{t}$+ Single Top	CR3 / W+jets	CR1b / Z/γ+jets
CR1a	1	0	0	0	
CR2	0.16	1	0.72	0.53	0
CR4	0	0	1	0.18	0
CR3	0	0	0.16	1	0
CR1b		0	0	0	0
SR	0.31	0.04	0.32	0.26	2.7

Table E.19: Initial cross Transfer Factors for SRE (tight).

Region	Main CR/Process				
	CR1a / Z/γ+jets	CR2 / QCD jets	CR4 / $t\bar{t}$+ Single Top	CR3 / W+jets	CR1b / Z/γ+jets
Central value	0.31	0.04	0.32	0.26	2.7
JER	0.045 0		0.055 0	0.042 0	1.8 0
JES	0.03 −0.0099		0.13 −0.03	0.037 −0.011	0.71 4
Pileup			0 0.078	0 −0.0097	
l resoln.			−0.0059 0.013	−0.004 0.0024	0 −0
Trigger			−0.0019 0.0019	−0.0014 0.0014	−0.037 0.037
b-tag/veto eff.			−0.037 0.054	−0.0066 0.0071	
acc. Z+jets/ γ	0.091 −0.091				
l scale.			−0.0059 0.008	−0.0026 0.0012	0 −0
QCD smear.		0.022 −0.022			
MET CellOut cluster	0.00019 −0.00012		−0.0043 0.0075	−0.0022 −0.0077	
Top Theory			0.2 −0.2		
l eff.			−0.0024 0.0025	−0.0018 0.0018	−0.041 0.042
MET CellOut pileup	2.7e−05 −0.0004		−0.0029 0.0038	−0.0015 0.0038	
PDF			−0.019 0.03	0.011 −0.0044	
Z+jets Theory					0.081 −0.081
MC stat.			0.092 −0.092	0.067 −0.067	2.1 −2.1
W+jets Theory				0.031 −0.031	

Table E.20: Initial uncertainties of Transfer Factors to signal region for SRE (tight).

Appendix F

Simultaneous Normalisation with low event counts

In the searches for SUSY the sensitivity to highest mass particles is bound to a good understanding of the high mass tail of kinematic observables. Any background to those searches is normalized by an additional measurement (control region) near to the kinematic selection chosen for discovery of new physics (signal region). As there are several backgrounds and thus several control regions a cross contamination of backgrounds processes in the control regions can occur. Therefore a **simultaneous** normalization is mandatory. The combination of the simultaneous fit and the push to high mass regions leads to the following question: Is the normalization and interpretation still valid if very low or even zero events are observed in control regions? To illustrate this a minimal complex toy example has been made. If we assume a problem with two background processes b_W and b_{tt}, and two normalization regions WR and TR, respectively. The amount of background in the signal region is estimated via a fixed transfer factor $c_{W\to SR}$ and $c_{tt\to SR}$. The amount of e.g. W in the signal region is then $W_{SR} = c_{W\to SR} \times b_W$ where b_W is already constrained by the measurement in the W control region. The likelihood $L(\boldsymbol{n}|\mu, \boldsymbol{b})$ for the counting model:

$$\begin{aligned} L(\boldsymbol{n}|\mu, \boldsymbol{b}) &= P_{\mathrm{SR}} \times P_{\mathrm{WR}} \times P_{\mathrm{TR}} && \text{(F.1)} \\ &= P(n_S|\lambda_S(\mu, \boldsymbol{b})) \times P(n_{WR}|\lambda_W(\boldsymbol{b}_W)) \times P(n_{TR}|\lambda_T(\boldsymbol{b}_T)) && \text{(F.2)} \end{aligned}$$

Each Poisson function $P_{i\mathrm{R}}$ uses as input the measured number of events in the region, n_i, and the expected number of events λ_i. The λ_i depend only on the b_i for which the corresponding control region was designed (ignoring cross contamination, signal contamination and additional nuisance parameters from systematic uncertainties) and the transfer factor. μ is the signal strength.

$$\begin{aligned} \lambda_{SR}(\mu, b_{WR}, b_{TR}) &= \mu \cdot s + C_{W\to\mathrm{SR}} \cdot b_W + C_{T\to\mathrm{SR}} \cdot b_T\ , && \text{(F.3)} \\ \lambda_{WR}(b_{WR}) &= b_{WR}, && \text{(F.4)} \\ \lambda_{TR}(b_{TR}) &= b_{TR}. && \text{(F.5)} \end{aligned}$$

Thus the expectations are defined by the following set of linear equations

$$\begin{pmatrix} 1 & C_{W\to \mathrm{SR}} & C_{T\to \mathrm{SR}} \\ 0 & 1 & 0 \\ 0 & 0 & 1 \end{pmatrix} \begin{bmatrix} s \\ b_W \\ b_T \end{bmatrix} = \begin{bmatrix} \lambda_{SR} \\ \lambda_{WR} \\ \lambda_{TR} \end{bmatrix}$$

The measurements in the control regions fix the expectations and thus the normalization of b_{WR} and b_{TR}. Given this setup there is only one unique solution to the problem and it has to be kept in mind that the measurement in the SR is not allowed to constrain b_{WR} and b_{TR} else the whole experiment is biased.
In the following a set of numbers are assumed corresponding to a low counting regime combined with changing the number of observed events in WR to 0, 2 or 4.

- Expected W events in SR : 2
- Expected W events in WR : 2
- Expected signal events in SR : 10
- Observed events in SR : 4
- Observed number in TR : 2
- Expected T events in TR : 2
- Expected T events in TR : 2
- $C_{W\to \mathrm{SR}}$: 1
- $C_{T\to \mathrm{SR}}$: 1

The system is solved numerically (this has to be done latest when including additional nuisance parameters) with the MIGRAD and MINOS implementation of Minuit. MIGRAD uses the HESSE formalism to calculate uncertainties. The results are presented in dependence of the measurement in WR in Fig. F.1. In all figures the dependency on the measurement in WR is shown.

In case of 0 measured events in WR b_W is fitted to 0 as expected, see Fig. F.1(a) and the MIGRAD minimization converges. However MIGRAD cannot calculate an uncertainty on b_W. In all cases where the observed events is non-zero the propagation of uncertainties works.
To generate the unconditional ensemble the most probable values of the nuisance parameters have to be calculated. This coincides with the simultaneous fit described before. In Fig. F.2 distributions of the conditional ensemble are shown. In Fig. F.2(a) the generated data in WR is shown and as the most probable value is 0 the generated data is as well 0. In Fig. F.2(b) the profile likelihood ratio is shown and shows discrete steps corresponding to the discrete outcomes of the Poisson pdf distributions.

In the following next to minimal example a cross contamination of $b_t t$ in WR is turned on. The matrix to solve then looks like:

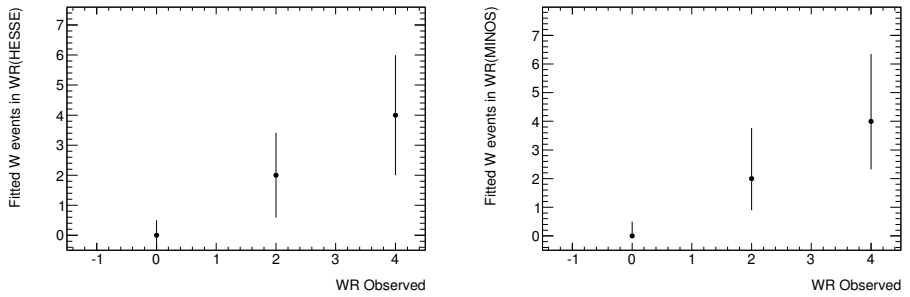

(a) Fitted Number of W events in WR/MIGRAD (b) Fitted Number of W events in WR/MINOS

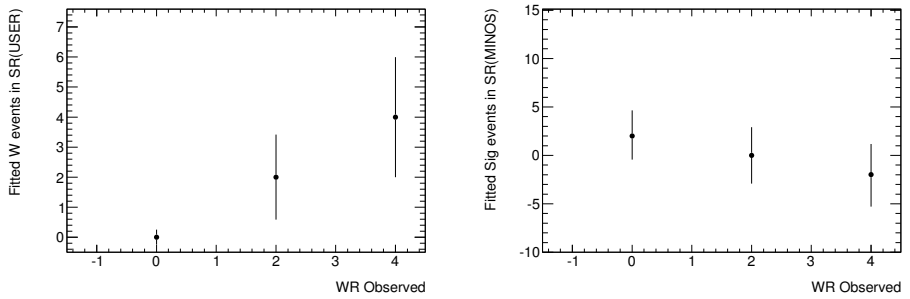

(c) Fitted Number of W events in SR (d) Fitted Number of SIG events in SR

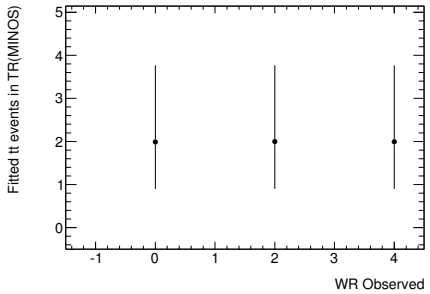

(e) Fitted Number of tt events in TR

Figure F.1: Fitted number of events in the toy example described in the text.

$$\begin{pmatrix} 1 & C_{W\to\mathrm{SR}} & C_{T\to\mathrm{SR}} \\ 0 & 1 & C_{T\to\mathrm{WR}} \\ 0 & 0 & 1 \end{pmatrix} \begin{bmatrix} s \\ b_W \\ b_T \end{bmatrix} = \begin{bmatrix} \lambda_{SR} \\ \lambda_{WR} \\ \lambda_{TR} \end{bmatrix}$$

and the numbers example expands to:

- Expected W events in SR : 2
- Expected W events in WR : 2
- Expected signal events in SR : 10
- Observed events in SR : 4
- Observed number in TR : 2

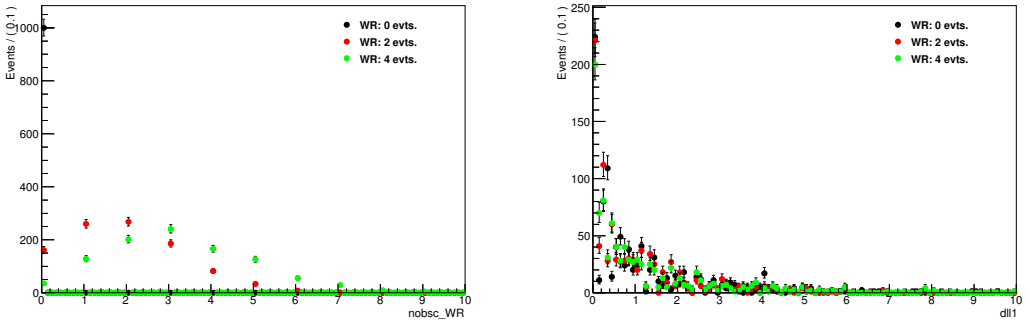

(a) Generated data in WR

(b) -2 log of Profile Likelihood ratio with mu=1

Figure F.2: Generated data in WR and profile likelihood ratio distribution of the unconditional ensemble of the toy example described in the text.

- Expected T events in TR : 2
- Expected T events in TR : 2
- $C_{W\to\mathrm{SR}}$: 1
- $C_{T\to\mathrm{SR}}$: 1
- $C_{T\to\mathrm{WR}}$: 0.5

The same effect as before is seen on b_W,see Fig. F.3, which is normalized to 0 with 0 measured in WR. The tt process however is as well constrained by this which can be seen in Fig. F.3(e). In case of 0 measured events in WR the fitted b_{tt} does take a value between 2 (measured in tt region) and 0. In any other case b_{tt} is solely constrained by TR. In Fig. F.4 the generated data in the WR and the TR is shown and the profile likelihood ratio distribution. The same conclusion as in the previous example holds. In case of 0 observed events in any control region the problem becomes ill defined.

To conclude: the profile likelihood construction does not work in case of 0 observed events in one of the control regions. Counting regions other than the SR with 0 events observed should be removed from the likelihood model. A possibility to gain more statistics in a control region is to relax some of the requirements. This has usually the pitfall that additional uncertainties from the interpolation due to different phase space requirements occur. Another option would be to translate the fact that 0 events were observed in the CR corresponding to process i into an upper limit of process i in the SR. this has the pitfall that the likelihood function has to be rewritten. This can be done, however in a highly automated setup this can get complicated. As the profile likelihood construction is at its edge in this situation the conditional ensemble might be more appropriate to consider. The minimization works from a technical point of view as long as at least one event is visible in the counting region.

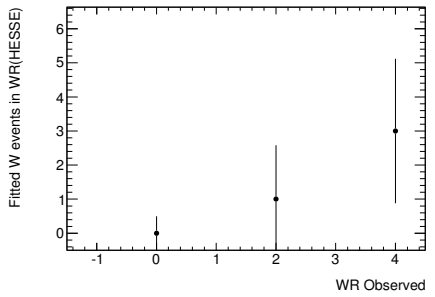

(a) Fitted Number of W events in WR/MIGRAD

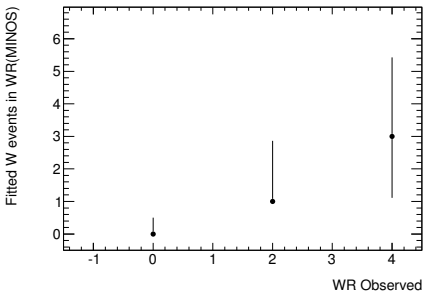

(b) Fitted Number of W events in WR/MINOS

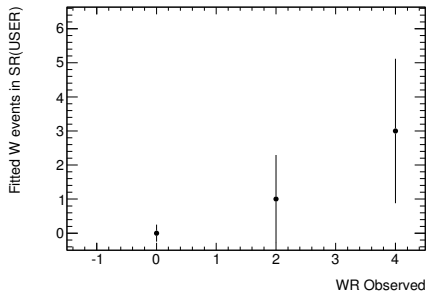

(c) Fitted Number of W events in SR

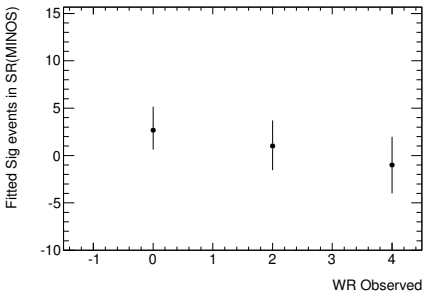

(d) Fitted Number of SIG events in SR

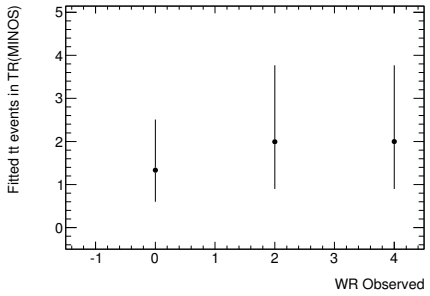

(e) Fitted Number of tt events in TR

Figure F.3: Fitted number of events in the next to minimal toy example described in the text.

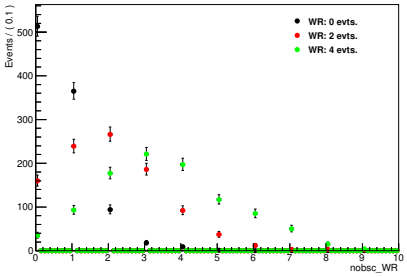

(a) Generated data in WR

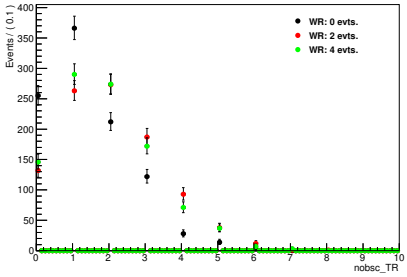

(b) Generated data in TR

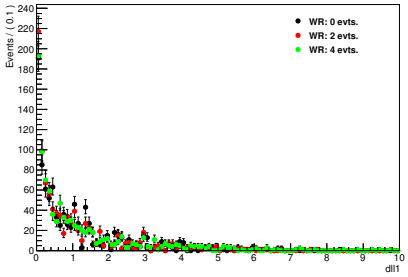

(c) -2 log of Profile Likelihood ratio with mu=1

Figure F.4: Generated data in WR and TR and profile likelihood ratio distribution of the unconditional ensemble of the next to minimal toy example described in the text.

Bibliography

[16] O. S. Brüning, P. Collier, P. Lebrun, S. Myers, R. Ostojic, J. Poole, and P. Proudlock, *LHC Design Report*, CERN, Geneva, 2004.

[17] ATLAS Collaboration, *The ATLAS Experiment at the CERN Large Hadron Collider*, JINST **3** (2008) S08003.

[18] ATLAS Collaboration, *Observation of a new particle in the search for the Standard Model Higgs boson with the ATLAS detector at the LHC*, Phys. Lett. **B716** (2012) 1–29, arXiv:1207.7214 [hep-ph].

[19] CMS Collaboration, *Observation of a new boson at a mass of 125 GeV with the CMS experiment at the LHC*, Phys. Lett. **B716** (2012) 30–61, arXiv:1207.7235 [hep-ph].

[20] J. Beringer et al., *Review of Particle Physics*, Phys. Rev. **D86** (2012) 010001.

[21] S. Weinberg, *The Quantum Theory of Fields (Volume 1)*, Cambridge University Press, June, 1995.

[22] T. Binoth, C. Buttar, P. Clark, and E. N. Glover, *Proceedings of 65th Scottish Universities Summer School in Physics: LHC Physics (SUSSP65)*, 2012.

[23] H. Flacher, M. Goebel, J. Haller, A. Hoecker, K. Monig, et al., *Revisiting the Global Electroweak Fit of the Standard Model and Beyond with Gfitter*, Eur.Phys.J. **C60** (2009) 543–583, arXiv:0811.0009 [hep-ph].

[24] M. Baak, M. Goebel, J. Haller, A. Hoecker, D. Ludwig, et al., *Updated Status of the Global Electroweak Fit and Constraints on New Physics*, Eur.Phys.J. **C72** (2012) 2003, arXiv:1107.0975 [hep-ph].

[25] M. Baak, M. Goebel, J. Haller, A. Hoecker, D. Kennedy, et al., *The Electroweak Fit of the Standard Model after the Discovery of a New Boson at the LHC*, Eur.Phys.J. **C72** (2012) 2205, arXiv:1209.2716 [hep-ph].

[26] M. Davier, A. Hoecker, B. Malaescu, and Z. Zhang, *Reevaluation of the Hadronic Contributions to the Muon g-2 and to alpha(MZ)*, Eur.Phys.J. **C71** (2011) 1515, arXiv:1010.4180 [hep-ph].

[27] H. Miyazawa, *Baryon Number Changing Currents*, Prog. Theor. Phys. **36 (6)** (1966) 1266–1276.

[28] Y. A. Gol'fand and E. P. Likhtman, *Extension of the Algebra of Poincare Group Generators and Violation of p Invariance*, JETP Lett. **13** (1971) 323–326.

[29] P. Ramond, *Dual Theory for Free Fermions*, Phys. Rev. **D3** (1971) 2415–2418.

[30] A. Neveu and J. H. Schwarz, *Factorizable dual model of pions*, Nucl. Phys. **B31** (1971) 86–112.

[31] A. Neveu and J. H. Schwarz, *Quark Model of Dual Pions*, Phys. Rev. **D4** (1971) 1109–1111.

[32] J. Gervais and B. Sakita, *Field theory interpretation of supergauges in dual models*, Nucl. Phys. **B34** (1971) 632–639.

[33] J. Wess and B. Zumino, *A Lagrangian Model Invariant Under Supergauge Transformations*, Phys. Lett. **B49** (1974) 52.

[34] J. Wess and B. Zumino, *Supergauge Transformations in Four-Dimensions*, Nucl. Phys. **B70** (1974) 39–50.

[35] S. Martin, *A Supersymmetry Primer*, `arXiv:hep-ph/9709356v6`.

[36] P. C. West, *Introduction to Supersymmetry and Supergravity*, World Scientific Pub Co Inc.

[37] S. Weinberg, *The quantum theory of fields. Vol. 3: Supersymmetry*, 2000.

[38] M. Peskin and D. Schroeder, *An introduction to quantum field theory*, Addison-Wesley Publishing Company, 1995.

[39] P. Fayet, *Supersymmetry and Weak, Electromagnetic and Strong Interactions*, Phys. Lett. **B64** (1976) 159.

[40] P. Fayet, *Spontaneously Broken Supersymmetric Theories of Weak, Electromagnetic and Strong Interactions*, Phys. Lett. **B69** (1977) 489.

[41] G. R. Farrar and P. Fayet, *Phenomenology of the Production, Decay, and Detection of New Hadronic States Associated with Supersymmetry*, Phys. Lett. **B76** (1978) 575–579.

[42] P. Fayet, *Relations Between the Masses of the Superpartners of Leptons and Quarks, the Goldstino Couplings and the Neutral Currents*, Phys. Lett. **B84** (1979) 416.

[43] S. Dimopoulos and H. Georgi, *Softly Broken Supersymmetry and SU(5)*, Nucl. Phys. **B193** (1981) 150.

[44] M. Asano, K. Rolbiecki, and K. Sakurai, *Can R-parity violation hide vanilla supersymmetry at the LHC?*, JHEP **1301** (2013) 128, `arXiv:1209.5778 [hep-ph]`.

[45] S. Weinberg, *Implications of Dynamical Symmetry Breaking*, Phys. Rev. **D13** (1976) 974–996.

[46] E. Gildener, *Gauge Symmetry Hierarchies*, Phys. Rev. **D14** (1976) 1667.

[47] S. Weinberg, *Implications of Dynamical Symmetry Breaking: An Addendum*, Phys. Rev. **D19** (1979) 1277–1280.

[48] L. Susskind, *Dynamics of Spontaneous Symmetry Breaking in the Weinberg- Salam Theory*, Phys. Rev. **D20** (1979) 2619–2625.

[49] E. Witten, *Dynamical Breaking of Supersymmetry*, Nucl. Phys. **B188** (1981) 513.

[50] M. Dine, W. Fischler, and M. Srednicki, *Supersymmetric Technicolor*, Nucl. Phys. **B189** (1981) 575–593.

[51] S. Dimopoulos and S. Raby, *Supercolor*, Nucl. Phys. **B192** (1981) 353.

[52] N. Sakai, *Naturalness in Supersymmetric Guts*, Zeit. Phys. **C11** (1981) 153.

[53] R. Kaul and P. Majumdar, *Cancellation of quadratically divergent mass corrections in globally supersymmetrc spontaneously broken gauge theories*, Nucl. Phys. **B199** (1982) 36.

[54] S. Dimopoulos, S. Raby, and F. Wilczek, *Supersymmetry and the Scale of Unification*, Phys. Rev. **D24** (1981) 1681–1683.

[55] L. E. Ibanez and G. G. Ross, *Low-Energy Predictions in Supersymmetric Grand Unified Theories*, Phys. Lett. **B105** (1981) 439.

[56] M. B. Einhorn and D. R. T. Jones, *The Weak Mixing Angle and Unification Mass in Supersymmetric SU(5)*, Nucl. Phys. **B196** (1982) 475.

[57] W. J. Marciano and G. Senjanovic, *Predictions of Supersymmetric Grand Unified Theories*, Phys. Rev. **D25** (1982) 3092.

[58] C. Giunti, C. W. Kim, and U. Lee, *Running coupling constants and grand unification models*, Mod. Phys. Lett. **A6** (1991) 1745–1755.

[59] J. Ellis, S. Kelley, and D. Nanopoulos, *Probing the desert using gauge coupling unification*, Phys. Lett. **B260** (1991) 131–137.

[60] U. Amaldi, W. de Boer, and H. Furstenau, *Comparison of grand unified theories with electroweak and strong coupling constants measured at LEP*, Phys. Lett. **B260** (1991) 447–455.

[61] P. Langacker and M.-X. Luo, *Implications of precision electroweak experiments for M(t), rho(0), sin**2-Theta(W) and grand unification*, Phys. Rev. **D44** (1991) 817–822.

[62] D. Larson, J. Dunkley, G. Hinshaw, E. Komatsu, M. Nolta, et al., *Seven-Year Wilkinson Microwave Anisotropy Probe (WMAP) Observations: Power Spectra and WMAP-Derived Parameters*, Astrophys.J.Suppl. **192** (2011) 16, arXiv:1001.4635 [astro-ph.CO].

[63] H. Goldberg, *Constraint on the photino mass from cosmology*, Phys. Rev. Lett. **50** (1983) 1419.

[64] J. Ellis, J. Hagelin, D. Nanopoulos, K. Olive, and M. Srednicki, *Supersymmetric relics from the big bang*, Nucl. Phys. **B238** (1984) 453–476.

[65] T. Appelquist, H.-C. Cheng, and B. A. Dobrescu, *Bounds on universal extra dimensions*, Phys. Rev. **D64** (2001) 035002.

[66] D. Hooper and S. Profumo, *Dark Matter and Collider Phenomenology of Universal Extra Dimensions*, Phys. Rept. **453** (2007) 29.

[67] H.-C. Cheng, K. T. Matchev and M. Schmaltz, *Bosonic Supersymmetry? Getting Fooled at the LHC*, Phys. Rev. D **66** (2002) 056006.

[68] ATLAS Collaboration, *Performance of the ATLAS Trigger System in 2010*, 2012. Eur.Phys.J. **C72** (2012) 1849, arXiv:1110.1530 [hep-ex].

[69] N. Metropolis and S. Ulam, *The Monte Carlo Method*, Journal of the American Statistical Association **44** (1949) 335.

[70] J. M. Campbell, J. Huston, and W. Stirling, *Hard Interactions of Quarks and Gluons: A Primer for LHC Physics*, Rept.Prog.Phys. **70** (2007) 89, arXiv:hep-ph/0611148 [hep-ph].

[71] V. Gribov and L. Lipatov, *Deep inelastic e p scattering in perturbation theory*, Sov.J.Nucl.Phys. **15** (1972) 438.

[72] G. Altarelli and G. Parisi, *Asymptotic Freedom in Parton Language*, Nucl.Phys. **B126** (1977) 298.

[73] Y. L. Dokshitzer, *Calculation of the Structure Functions for Deep Inelastic Scattering and e+ e- Annihilation by Perturbation Theory in Quantum Chromodynamics.*, Sov.Phys.JETP **46** (1977) 641–653.

[74] T. Sjostrand, S. Mrenna, and P. Z. Skands, *PYTHIA 6.4 Physics and Manual*, JHEP **0605** (2006) 026, arXiv:hep-ph/0603175.

[75] W. Beenakker, R. Hopker, M. Spira, and P. M. Zerwas, *Squark and gluino production at hadron colliders*, Nucl. Phys. **B492** (1997) 51–103, arXiv:hep-ph/9610490.

[76] W. Beenakker et al., *Soft-gluon resummation for squark and gluino hadroproduction*, JHEP **0912** (0912) 041, arXiv:0909.4418 [hep-ph].

[77] W. Beenakker, S. Brensing, M. Kramer, A. Kulesza, E. Laenen, et al., *Squark and gluino hadroproduction*, Int.J.Mod.Phys. **A26** (2011) 2637–2664, arXiv:1105.1110 [hep-ph].

[78] A. Kulesza and L. Motyka, *Threshold resummation for squark-antisquark and gluino-pair production at the LHC*, Phys.Rev.Lett. **102** (2009) 111802.

[79] A. Kulesza and L. Motyka, *Soft gluon resummation for the production of gluino-gluino and squark-antisquark pairs at the LHC*, Phys.Rev. **D80** (2009) 095004.

[80] P. Falgari, C. Schwinn, and C. Wever, *NLL soft and Coulomb resummation for squark and gluino production at the LHC*, JHEP **1206** (2012) 052, arXiv:1202.2260 [hep-ph].

[81] M. Botje et al., *The PDF4LHC Working Group Interim Recommendations*, arXiv:1101.0538 [hep-ph].

[82] Krämer, Kuleszal, van der Leeuw, Mangano, Padhi, Plehn, and Portell, *Supersymmetry production cross sections in pp collisions at* $\sqrt{s} = 7$ *TeV*, arXiv:1206.2892v1 [hep-ph].

[83] P. M. Nadolsky et al., *Implications of CTEQ global analysis for collider observables*, Phys. Rev. **D78** (2008) 013004.

[84] A. Sherstnev and R. S. Thorne, *Parton Distributions for LO Generators*, Eur. Phys. J. **C55** (2008) 553–575, arXiv:0711.2473 [hep-ph].

[85] J. A. Conley, J. S. Gainer, J. L. Hewett, M. P. Le, and T. G. Rizzo, *Supersymmetry Without Prejudice at the 7 TeV LHC*, Physical Review D (2011) , arXiv:1103.1697 [hep-ph].

[86] J. L. Feng, J.-F. Grivaz, and J. Nachtman, *Searches for Supersymmetry at High-Energy Colliders*, Rev.Mod.Phys. **82** (2010) 699–727, arXiv:0903.0046 [hep-ex].

[87] M. Bahr et al., *Herwig++ Physics and Manual*, Eur. Phys. J. **C58** (2008) 639–707, arXiv:0803.0883 [hep-ph].

[88] M. Bahr et al., *Herwig++ 2.3 release note*, arXiv:0812.0529 [hep-ph].

[89] F. Maltoni and T. Stelzer, *MadEvent: Automatic event generation with MadGraph*, JHEP **0302** (2003) 027, arXiv:hep-ph/0208156 [hep-ph].

[90] J. Alwall et al., *MadGraph/MadEvent v4: The New Web Generation*, JHEP **09** (2007) 028, arXiv:0706.2334 [hep-ph].

[91] T. J. LeCompte and M. S. P., *Large Hadron Collider reach for supersymmetric models with compressed mass spectra*, Phys. Rev. **D84** (2011) 015004, arXiv:1105.4304 [hep-ph].

[92] T. J. LeCompte and M. S. P., *Compressed supersymmetry after 1/fb at the Large Hadron Collider*, Phys. Rev. **D85** (2012) 035023, arXiv:1111.6897 [hep-ph].

[93] M. L. Mangano, M. Moretti, F. Piccinini, R. Pittau, and A. D. Polosa, *ALPGEN, a generator for hard multiparton processes in hadronic collisions*, JHEP **07** (2003) 001, arXiv:hep-ph/0206293.

[94] G. Corcella et al., *HERWIG 6.5: an event generator for Hadron Emission Reactions With Interfering Gluons (including supersymmetric processes)*, JHEP **01** (2001) 010, arXiv:hep-ph/0011363.

[95] G. Corcella et al., *HERWIG 6.5 release note*, 2002. arXiv:hep-ph/0210213.

[96] J. M. Butterworth, J. R. Forshaw, and M. H. Seymour, *Multiparton interactions in photoproduction at HERA*, Z. Phys. **C72** (1996) 637–646, arXiv:hep-ph/9601371.

[97] T. Gleisberg, S. Hoeche, F. Krauss, M. Schonherr, S. Schumann, et al., *Event generation with SHERPA 1.1*, JHEP **0902** (2009) 007, arXiv:0811.4622 [hep-ph].

[98] B. P. Kersevan and E. Richter-Was, *The Monte Carlo event generator AcerMC version 2.0 with interfaces to PYTHIA 6.2 and HERWIG 6.5*, arXiv:hep-ph/0405247 [hep-ph].

[99] ATLAS Collaboration, *First tuning of HERWIG/JIMMY to ATLAS data*, Tech. Rep. ATL-PHYS-PUB-2010-014, CERN, Geneva, 2010.

[100] ATLAS Collaboration, *ATLAS tunes of PYTHIA 6 and Pythia 8 for MC11*, Tech. Rep. ATL-PHYS-PUB-2011-009, CERN, Geneva, 2011.

[101] ATLAS Collaboration, *Further ATLAS tunes of PYTHIA6 and Pythia 8*, Tech. Rep. ATL-PHYS-PUB-2011-014, CERN, Geneva, 2011.

[102] ATLAS Collaboration, G. Aad et al., *The ATLAS Simulation Infrastructure*, Eur. Phys. J. **C70** (2010) 823–874, arXiv:1005.4568 [physics.ins-det].

[103] S. Agostinelli et al., *GEANT4: A simulation toolkit*, Nucl. Instrum. Meth. **A506** (2003) 250–303.

[104] ATLAS Collaboration, *Performance of the ATLAS transverse energy triggers with initial LHC runs at* $\sqrt{s} = 7$ *TeV*, Tech. Rep. ATLAS-CONF-2011-072, May, 2011.

[105] ATLAS Collaboration, *Jet Trigger Performance with 2011 Data*, Tech. Rep. ATL-COM-DAQ-2011-063, CERN, 2011.

[106] M. Cacciari, G. P. Salam, and G. Soyez, *The anti-k_t jet clustering algorithm*, JHEP **04** (2008) 063, arXiv:0802.1189 [hep-ph].

[107] W. Lampl et al., *Calorimeter Clustering Algorithms: Description and Performance*, Tech. Rep. ATL-LARG-PUB-2008-002, CERN, 2011 .

[108] ATLAS Collaboration, *Jet energy measurement with the ATLAS detector in proton-proton collisions at* $\sqrt{s} = 7$ *TeV*, arXiv:1112.6426 [hep-ex].

[109] ATLAS Collaboration, *Commissioning of the ATLAS high-performance b-tagging algorithms in the 7 TeV collision data*, Tech. Rep. ATLAS-CONF-2011-102. http://cdsweb.cern.ch/record/1369219.

[110] ATLAS Collaboration, *Measurement of the b-tag Effciency in a Sample of Jets Containing Muons with 5* fb^{-1} *of Data from the ATLAS Detector*, Tech. Rep. ATLAS-CONF-2012-043. http://cdsweb.cern.ch/record/1435197.

[111] ATLAS Collaboration, *Electron performance measurements with the ATLAS detector using the 2010 LHC proton-proton collision data*, Eur. Phys. J. **C72** (2012) 1909, arXiv:1110.3174 [hep-ex].

[112] ATLAS Collaboration, *Muon Momentum Resolution in First Pass Reconstruction of pp Collision Data Recorded by ATLAS in 2010*, Tech. Rep. ATLAS-CONF-2011-046. http://cdsweb.cern.ch/record/1338575.

[113] ATLAS Collaboration, *Muon reconstruction effciency in reprocessed 2010 LHC proton-proton collision data recorded with the ATLAS detector*, Tech. Rep. ATLAS-CONF-2011-063. http://cdsweb.cern.ch/record/1345743.

[114] ATLAS Collaboration, *Measurement of the inclusive isolated prompt photon cross-section in pp collisions at* $\sqrt{s} = 7$ *TeV using 35* pb^{-1} *of ATLAS data*, Physics Letters B **706 (2-3)** (2011) 150–167.

[115] ATLAS Collaboration, *Luminosity Determination in pp Collisions at* $\sqrt{s} = 7$ *TeV Using the ATLAS Detector at the LHC*, Eur.Phys.J **C71** (2011) 1630, arXiv:1101.2185 [hep-ex].

[116] ATLAS Collaboration, *Luminosity Determination in pp Collisions at* $\sqrt{s} = 7$ *TeV Using the ATLAS Detector in 2011*, ATLAS-CONF-2011-116 , http://cdsweb.cern.ch/record/1376384.

[117] T. Sjostrand, S. Mrenna, and P. Z. Skands, *A Brief Introduction to PYTHIA 8.1*, Comput. Phys. Commun. **178** (2008) 852–867, arXiv:0710.3820.

[118] S. Ask, M. Parker, T. Sandoval, M. Shea, and W. Stirling, *Using gamma+jets Production to Calibrate the Standard Model Z(nunu)+jets Background to New Physics Processes at the LHC*, JHEP **1110** (2011) 058, arXiv:1107.2803 [hep-ph].

[119] J. Butterworth, E. Dobson, U. Klein, B. Mellado Garcia, T. Nunnemann, J. Qian, D. Rebuzzi, and R. Tanaka, *Single Boson and Diboson Production Cross Sections in pp Collisions at sqrts=7 TeV*, Tech. Rep. ATL-COM-PHYS-2010-695, CERN, Geneva, Aug, 2010.

[120] K. Stoerig and G. Herten, *QCD background estimation for Supersymmetry searches with jets and missing transverse momentum with the ATLAS experiment at the Large Hadron Collider*, PhD thesis, Freiburg U., 2012.

[121] M. Aliev, H. Lacker, U. Langenfeld, S. Moch, P. Uwer, et al., *HATHOR: HAdronic Top and Heavy quarks crOss section calculatoR*, Comput.Phys.Commun. **182** (2011) 1034–1046, arXiv:1007.1327 [hep-ph].

[122] G. Cowan, *Statistical Data Analysis*, Clarendon Press, 1998.

[123] L. Moneta, K. Belasco, K.Cranmer, S. Kreiss, A. Lazzaro, D. Piparo, G. Schott, W. Verkerke, and M. Wolf, *The RooStats Project*, arXiv:1009.1003 [physics.data-an].

[124] W. Verkerke, *Statistical Software for the LHC*, proceedings of the PHYSTAT LHC Workshop, CERN (2007) 169.

[125] K. Cranmer, G. Lewis, L. Moneta, A. Shibata, and W. Verkerke, *HistFactory: A tool for creating statistical models for use with RooFit and RooStats*, Tech. Rep. CERN-OPEN-2012-016, Jan, 2012.

[126] A. Read, *Presentation of search results: the CLs technique*, Journal of Physics G: Nucl. Part. Phys. **28** (2002) 2693–2704.

[127] J. S. Conway, *Incorporating Nuisance Parameters in Likelihoods for Multisource Spectra*, arXiv:1103.0354 [hep-ph]. Presented at PHYSTAT 2011, CERN, Geneva, Switzerland, January 2011, to be published in a CERN Yellow Report.

[128] R. Barlow and C. Beeston, *Fitting using finite Monte Carlo samples*, Computer Physics Communications **77** (1993) no. 2, 219 – 228.

[129] F. James, *MINUIT Reference Manual*, CERN Program Library Writeup **D506** .

[130] G. Cowan, K. Cranmer, E. Gross, and O. Vitells, *Asymptotic formulae for likelihood-based tests of new physics*, Eur. Phys. J. **C71** (2011) 1554, arXiv:1007.1727 [physics.data-an].

[131] Sinervo, *Signal Significance in Particle Physics*, Proceedings of the conference: Advanced Statistical Techniques in Particle Physics, Durham (2002) .

[132] J. Jaeckel, V. V. Khoze, T. Plehn, and P. Richardson, *Travels on the squark-gluino mass plane*, PRD **85** (2012) 015015.

[133] CDF Collaboration, *Search for Gluinos and Scalar Quarks in $p\overline{p}$ Collisions at $\sqrt{s} = 1.8$ TeV Using the Missing Energy plus Multijets Signature*, Phys. Rev. Lett. **88** (2002) 041801.

[134] CDF Collaboration, *Inclusive Search for Squark and Gluino Production in $p\overline{p}$ Collisions at* $\sqrt{s} = 1.96$ TeV, Phys. Rev. Lett. **102** (2009) 121801.

[135] D0 Collaboration, *Search for squarks and gluinos in events with jets and missing transverse energy using 2.1 fb^{-1} of collision data at*, Physics Letters B **660** (2008) no. 5, 449 – 457.

[136] CMS Collaboration Collaboration, S. Chatrchyan et al., *Interpretation of searches for supersymmetry with simplified models*, arXiv:1301.2175 [hep-ex].

[137] M. W. Cahill-Rowley, J. L. Hewett, A. Ismail, and T. G. Rizzo, *More Energy, More Searches, but the pMSSM Lives On*, arXiv:1211.1981 [hep-ph].

[138] M. W. Cahill-Rowley, J. L. Hewett, A. Ismail, and T. G. Rizzo, *The Higgs Sector and Fine-Tuning in the pMSSM*, Phys.Rev. **D86** (2012) 075015, arXiv:1206.5800 [hep-ph].

[139] R. Mahbubani, M. Papucci, G. Perez, J. T. Ruderman, and A. Weiler, *Light non-degenerate squarks at the LHC*, arXiv:1212.3328 [hep-ph].

[140] ATLAS Collaboration, *Search for light top squark pair production in final states with leptons and b-jets with the ATLAS detector in* $\sqrt{s} = 7$ *TeV proton-proton collisions*, Tech. Rep. CERN-PH-EP-2012-207, 2012. arXiv:1209.2102 [hep-ex].

[141] ATLAS Collaboration, *Search for a heavy top-quark partner in final states with two leptons with the ATLAS detector at the LHC*, JHEP **1211** (2012) 094, arXiv:1209.4186 [hep-ex].

[142] M. Drees and G. Gerbier, *Mini-Review of Dark Matter: 2012*, arXiv:1204.2373 [hep-ph].

[143] O. Buchmueller, R. Cavanaugh, M. Citron, A. De Roeck, M. Dolan, et al., *The CMSSM and NUHM1 in Light of 7 TeV LHC,* B_s *to mu+mu- and XENON100 Data*, Eur.Phys.J. **C72** (2012) 2243, arXiv:1207.7315 [hep-ph].

[144] Atlas Collaboration, *Search for Supersymmetry Using Final States with One Lepton, Jets, and Missing Transverse Momentum with the ATLAS Detector in sqrt(7) TeV pp Collisions*, PRL **106** (2011) 131802, arXiv:1102.2357 [hep-ph].

List of Figures

List of Tables

Acknowledgements / Danksagung

Diese Arbeit wäre nicht möglich gewesen ohne die Unterstützung und Hilfe folgender Menschen, denen ich hiermit danke.

Prof. Gregor Herten, *Dr. Sascha Caron* für die Betreuung dieser Arbeit und wertvolle Kommentare und Diskussionen.

Dr. Janet Dietrich, Dr. Stephan Horner, Dr. Florian Ahles, Riccardo-Maria Bianchi, Dr. Jan Sundermann, Dr. Zuzana Rurikova, Dr. Kathrin Störig, Tobias Rave, Valerio Consorti, Simone Amoroso, Tomas Javurek, Martina Pagacova, Fabio Cardillo, Antonia Strübig für nützliche Diskussionen, Hilfe beim Programmieren und Unterstützung meiner Arbeit. Insbesondere möchte ich mich bei Dr. Max Baak, Dr. Renaud Bruneliere und Prof. Dan Tovey bedanken für ihre Geduld und Hilfe bei statistischen und anderen Fragestellungen und bei Teng Jian Khoo für zahlreiche Diskussionen und virtuelle Gesellschaft in durchgemachten Nächten vor Konferenzen.